

arXiv:2512.15096v1 [gr-qc] 17 Dec 2025

Cosmological Models with Symmetric Teleparallel Gravity and its Extension

THESIS

Submitted in fulfillment
of the requirements for the degree of
DOCTOR OF PHILOSOPHY

by

Shubham Atmaram Narawade
2021PHXF0039H

Under the Supervision of
Prof. BIVUDUTTA MISHRA



BITS Pilani
Pilani | Dubai | Goa | Hyderabad

BIRLA INSTITUTE OF TECHNOLOGY AND SCIENCE, PILANI
2025

BIRLA INSTITUTE OF TECHNOLOGY AND SCIENCE, PILANI

CERTIFICATE

This is to certify that the thesis entitled “*Cosmological Models with Symmetric Teleparallel Gravity and its Extension*” and submitted by **Shubham Atmaram Narawade**, ID No. **2021PHXF0039H** for the award of Ph.D. of the Institute embodies original work done by him under my supervision.

Supervisor

Prof. BIVUDUTTA MISHRA

Professor,

BITS-Pilani, Hyderabad Campus

Date:

Declaration of Authorship

I, **Shubham Atmaram Narawade**, declare that this thesis titled, ‘Cosmological Models with Symmetric Teleparallel Gravity and its Extension’ and the work presented in it are my own. I confirm that:

- This work was done wholly or mainly while in candidature for a research degree at this University.
- No portion of this work referred to in this thesis has been submitted in support of an application for another degree or qualification of this or any other university or other institution of learning.
- Where I have consulted the published work of others, this is always clearly attributed.
- Where I have quoted from the work of others, the source is always given. With the exception of such quotations, this thesis is entirely my own work.

Signed:

Date:

To

My Parents, Wife & Friends

Acknowledgements

It gives me great joy to have the chance to offer my sincere gratitude to everyone whose inspirational influences have supported me as I pursue my doctorate.

My supervisor, **Prof. Bivudutta Mishra**, Professor, Department of Mathematics, BITS-Pilani, Hyderabad Campus, is to be sincerely thanked. His tenacity and unwavering excitement motivate me. The chance to collaborate with him has been a wonderful privilege. Along with his superior mathematical knowledge and teaching abilities, his humanism has served as a wonderful model for me. This dissertation would not exist without his committed help and direction.

I would also like to thank my DAC members, **Prof. Pradyumn Kumar Sahoo** and **Prof. Prasant Samantray**, for their insightful questions, insightful comments and constant feedback throughout this research.

I would like to extend my sincere gratitude to the Head of the Department, the DRC Convener and the entire staff of the Department of Mathematics at BITS-Pilani Hyderabad Campus for their assistance, support and encouragement in carrying out my research.

I am also grateful to the Associate Dean of AGRSD BITS-Pilani, Hyderabad Campus.

I gratefully acknowledge BITS-Pilani, Hyderabad Campus, for providing the necessary facilities and financial support during my research endeavors.

I would like to take this opportunity to thank, **Prof. Sunil Kumar Tripathy**, **Prof. Tomohiro Inagaki** and **Mr. Muhammad Azzam Alwan** for providing me with the opportunity to collaborate with them. I have gained a great deal of knowledge from them, for which I am quite grateful.

I would like to express my gratitude to my research team **Dr. Amar**, **Dr. Siddheshwar**, **Dr. Santosh**, **Dr. Lokesh**, **Rahul**, **Kalpana**, **Shivam**, **Priyobarta**. I would also like to acknowledge all my friends at BITS-Pilani, Hyderabad Campus for their unwavering support and encouragement throughout this journey. While not all are mentioned by name, each one has played a vital role in my success.

Most importantly, I would like to thank my parents, wife, brothers, sisters, family members and friends for their love, care and support for my personal life.

Abstract

This thesis investigates late-time cosmic acceleration using modified gravity theories with a focus on $f(Q)$ gravity, as an alternative to the Λ CDM model. The standard cosmological model attributes the acceleration to a cosmological constant, but it faces issues like the unexplained nature of dark matter and dark energy and discrepancies with certain observations. Modified gravity including $f(Q)$ gravity, offers a potential solution by incorporating dynamic dark energy or changes to gravitational interactions, avoiding the need for a constant cosmological term. Also, thesis evaluates the viability of $f(Q)$ gravity by analyzing observational data from Type Ia Supernovae, Hubble parameter measurements and other cosmological datasets. Using statistical tools like Markov Chain Monte Carlo (MCMC) analysis, this work constrains the parameters of $f(Q)$ gravity and compares it to the Λ CDM model.

The chapter 1 provides an overview of background formulation, fundamental gravity theories and cosmological observations. Chapters 2-5 explore the dark energy sector of the Universe within the context of modified gravity, using MCMC methods and extensive datasets obtained from measurements of the background expansion. Our analysis includes the reconstruction as well as the stability of the cosmological model.

In chapter 2, we present a comprehensive analysis of two distinct forms of $f(Q)$, specifically the log-square-root model and the exponential model, within the framework of cosmological evolution driven by dark energy. The equation of state (EoS) parameter for dark energy in both models is derived as a dynamical quantity, with log-square-root model exhibiting quintessence behavior at present and converges to the Λ CDM model at late-time, while exponential model demonstrates phantom behavior. A dynamical system analysis is employed to examine the stability of critical points and phase portraits, revealing the evolutionary behavior of the matter, radiation and dark energy phases.

The chapter 3 delves into the $f(Q)$ gravity framework, investigating the cosmological model by constraining its parameters using cosmological datasets, including recent Hubble data and the Pantheon+SH0ES datasets. An MCMC analysis is performed to constrain the free parameter of the Hubble function, with the results being validated against the BAO dataset. The parametrization of cosmographic parameters results the early deceleration and late-time acceleration transition, with the equation of state parameter indicating a phantom behavior, further supported by the $Om(z)$ diagnostics. Additionally, the current age of the Universe is determined.

In chapter 4, we explore the reconstruction of the $q(z)$ and its impact on the $f(Q)$ gravity, utilizing OHD, SNe Ia and BAO datasets. Two parametrization of $q(z)$ are fitted to the cosmological models using MCMC analysis. The model I, parameterized by a power-law function of redshift,

shows strong alignment with recent higher H_0 measurements, while model II, incorporating logarithmic terms, provides tighter constraints on matter density. Both models successfully recover observationally consistent estimates for the Hubble constant H_0 and matter density Ω_{m_0} , with varying precision in alignment with the Λ CDM model. Statistical comparisons with the Akaike Information Criteria (AIC) and Bayesian Information Criterion (BIC) indicate that these $f(Q)$ models are competitive alternatives to the Λ CDM model in explaining dark energy and cosmic acceleration.

The chapter 5, focuses on the reconstruction of the cosmological model within the framework of $f(Q)$ gravity through non-trivial connection. The dynamic behavior of two models, particularly model within coincident gauge and the reconstructed model are thoroughly studied using the Hubble parameter $H(z)$ and various observational datasets for the comparative analysis. The findings confirm that both the model exhibits quintessence behavior at the present epoch and asymptotically approaches the Λ CDM model at late-time. Additionally, we explore the energy conditions and the violation of strong energy condition supports the accelerating behavior of the models. The scalar perturbation analysis confirms the stability of the reconstructed model with respect to the Hubble parameter. These results provide strong support for $f(Q)$ gravity as a viable alternative to the Λ CDM model, offering compelling insights into the nature of cosmic acceleration and the evolution of the Universe.

The concluding chapter 6 of the thesis summarizes the key findings and discusses the research presented throughout the thesis, highlighting potential future directions for research and applications in the field.

Contents

Certificate	i
Declaration of Authorship	ii
Acknowledgements	iv
Abstract	v
Contents	vii
List of Tables	x
List of Figures	xi
List of Symbols	xiii
List of Abbreviations	xiv
1 Introduction	1
1.1 Geometric Setup	2
1.2 Foundation of Cosmological Dynamics	4
1.2.1 The FLRW metric	5
1.2.2 Redshift in cosmology	6
1.2.3 Energy conservation in cosmology	6
1.2.4 The stress-energy-momentum tensor	8
1.2.5 Energy conditions	9
1.2.6 Cosmographic parameters	10
1.2.7 Overview of the Λ CDM model	11
1.2.8 Successes and shortcomings of standard cosmological model	12
1.3 Exploring Alternative Cosmological Theories	14

1.3.1	Dark energy models	14
1.3.2	Modified gravity models	15
1.4	Symmetric Teleparallelism	16
1.4.1	Geometrical representation	16
1.4.2	Decomposition of Affine connection	17
1.4.3	Symmetric teleparallel equivalent to GR	19
1.4.4	$f(Q)$ extension	19
1.4.4.1	Coincident gauge	20
1.4.4.2	Non-coincident gauge	22
1.5	Basics of Statistics	23
1.5.1	χ^2 model fitting	24
1.5.2	Maximum likelihood analysis	25
1.6	Observational Datasets	27
1.6.1	Hubble measurements	27
1.6.2	Type Ia Supernovae	27
1.6.3	Baryon acoustic oscillations	28
1.7	Stability Analysis	29
1.7.1	Linear stability theory	30
1.7.2	Cosmological scalar perturbation	31
2	Accelerating cosmological models in $f(Q)$ gravity and the phase space analysis	33
2.1	Introduction	34
2.2	Modified field equations	34
2.3	The $f(Q)$ gravity models	35
2.3.1	Log-square-root model	36
2.3.2	Exponential model	38
2.4	Phase space analysis	39
2.5	Results and Conclusion	45
3	Phantom cosmological model with observational constraints in $f(Q)$ gravity	46
3.1	Introduction	47
3.2	Power-law model	47
3.2.1	$H(z)$ parameterization	48
3.3	Observational datasets	49
3.3.1	Hubble dataset	49
3.3.2	Pantheon+SH0ES dataset	49
3.3.3	MCMC analysis and Results	49
3.4	BAO/CMB validation	52
3.4.1	BAO dataset	52
3.4.2	CMB dataset	52
3.5	Cosmographic parameters	54
3.6	Test for the validation	57
3.6.1	$Om(z)$ diagnostic	57
3.6.2	Age of the Universe	57
3.7	Conclusion	58
4	Insights into $f(Q)$ gravity: Modeling through the deceleration parameter	59

4.1	Introduction	60
4.2	Reconstruction of $q(z)$	61
4.3	Observational datasets	62
4.3.1	Hubble dataset	62
4.3.2	Type Ia Supernovae compilation	63
4.3.3	BAO dataset	63
4.4	Impact on $f(Q)$ models	64
4.4.1	Power-law function	64
4.4.2	Logarithmic function	67
4.4.3	Model comparison	69
4.5	Conclusion	70
5	Stable $f(Q)$ gravity model through trivial and non-trivial connection	72
5.1	Introduction	73
5.2	Reconstruction of the $f(Q)$ model	74
5.3	Data analysis and parameter estimation	75
5.4	Comparative analysis	76
5.4.1	Model within coincident gauge	76
5.4.2	Model reconstructed through non-coincident gauge	78
5.4.3	Analyzing stability with scalar perturbation	80
5.5	Conclusion	81
6	Concluding Remarks and Future perspectives	83
References		86
Appendices		104
List of Publications and Presentations		107
Biography		110

List of Tables

1.1	A summary of possible geometries.	6
1.2	Energy conditions with their physical and geometrical significance.	9
2.1	Critical Points and the corresponding cosmology for log-square-root model. . . .	41
2.2	Critical Points and the corresponding cosmology for exponential model.	43
3.1	The marginalized constraining results of the parameters using Hubble and Pantheon+SH0ES data.	51
3.2	The marginalized constraining results of the cosmographic parameters using Hubble and Pantheon+SH0ES data.	55
4.1	Constrained values of free parameters based on the different combinations of OHD, SNe Ia and BAO datasets for the power-law function.	65
4.2	Constrained values of free parameters based on the different combinations of OHD, SNe Ia and BAO datasets for the logarithmic function.	67
4.3	The comparison of the models with the Λ CDM model for OHD+Pantheon and OHD+Pantheon ⁺ datasets.	70
4.4	The comparison of the models with the Λ CDM model for OHD+Pantheon+BAO and OHD+Pantheon ⁺ +BAO datasets.	70
5.1	Best-fit values of parameter space using OHD, Pantheon ⁺ and OHD+Pantheon ⁺ +BAO dataset.	75
6.1	$H(z)$ measurements expressed in $[\text{km s}^{-1} \text{ Mpc}^{-1}]$ units, were obtained using the CC technique, along with the associated errors.	104
6.2	The Pantheon ⁺ compilation includes various samples, detailing the number of SNe Ia utilized in the cosmological sample (N_{SN}) versus the total count from the complete dataset (N_{Tot}) along with the specifics on the redshift range covered. .	105
6.3	The most recent BAO distance dataset includes measurements at six different redshifts.	106

List of Figures

1.1	Depending on the properties of connection, the subclasses of metric-affine geometry. [Credit: Phys. Rev. D. 97, 124025 (2018)]	18
2.1	Evolution of cosmographic parameters as a function of redshift.	36
2.2	Evolution of log-square-root model as a function of redshift.	37
2.3	The behavior of the dynamical parameter for log-square-root model in redshift.	37
2.4	Evolution of exponential model as a function of redshift.	38
2.5	The behavior of the dynamical parameter for exponential model in redshift.	39
2.6	The phase-space portrait for log-square-root model.	41
2.7	Evolution of EoS Parameter and density parameters for log-square-root model. The vertical dashed red line denotes the present time.	43
2.8	The phase-space portrait for exponential model.	44
2.9	Evolution of EoS parameter and density parameters for exponential model. The vertical dashed red line denotes the present time.	45
3.1	MCMC contour plot obtained from the observational datasets for 1σ and 2σ confidence interval.	50
3.2	Error bar plot obtained from the observational datasets.	51
3.3	Error bar plot for the model utilizing BAO/CMB dataset.	54
3.4	The marginalized constraints on the $H(z)$, $q(z)$ and $j(z)$ using redshift values.	56
3.5	Evolution of cosmographic parameters as a function of redshift.	56
3.6	Graphical representation of the test validation of the behavior of the model.	58
4.1	Confidence contours and posteriors for the parameters H_0 , b and n of the power-law function.	65
4.2	Reconstruction of $f(Q)$ model for power-law function. The best analytical match- ing (solid red) to the numerical solution (dashed blue).	66
4.3	Confidence contours and posteriors for the parameters H_0 and b of the logarithmic function.	68
4.4	Reconstruction of $f(Q)$ model for logarithmic function. The best analytical match (solid red) to the numerical solution (dashed blue).	68
5.1	MCMC contour plot obtained from the observational datasets for 1σ and 2σ confidence interval.	75
5.2	The behavior of the dynamical parameters for model within coincident gauge.	77
5.3	The behavior of energy conditions for the model within coincident gauge.	77
5.4	The behavior of the dynamical parameters for the model reconstructed through non-coincident gauge.	79

5.5	The behavior of energy conditions for the model reconstructed through non-coincident gauge.	79
5.6	Evolution of δ and δ_m versus redshift. Herein, we set the initial conditions $\delta(0) = 0.1$ and $\delta_m(0) = 0.01$	81

List of Symbols

H	: Hubble parameter
q	: Deceleration parameter
s	: Snap parameter
j	: Jerk parameter
z	: Redshift
\mathcal{L}_m	: Matter Lagrangian
g_{ij}	: Lorentzian metric
g	: Determinant of g_{ij}
G_{ij}	: Einstein tensor
Λ	: Cosmological constant
Γ_{ij}^k	: General affine connection
$\{\Gamma_{ij}^k\}$: Levi-Civita connection
∇_i	: Covariant derivative
$R_{\sigma ij}^k$: Riemann tensor
R_{ij}	: Ricci tensor
R	: Ricci scalar
T	: Torsion
Q	: Non-metricity scalar
S_M	: Matter action
T_{ij}	: Energy-momentum tensor
\mathcal{T}	: Trace of the energy-momentum tensor
L_{ij}^k	: Disformation tensor
P_{ij}^k	: Super potential
$H_{\mu\nu}^\lambda$: Hyper momentum tensor
χ^2	: Chi-square

List of Abbreviations

GR	: General Relativity
TEGR	: Teleparallel Equivalent to General Relativity
STEGR	: Symmetric Teleparallel Equivalent to General Relativity
Λ CDM	: Λ Cold Dark Matter
EoS	: Equation of State
CMB	: Cosmic Microwave Background
BAO	: Baryon Acoustic Oscillations
MCMC	: Markov Chain Monte Carlo
DE	: Dark Energy
DM	: Dark Matter
MG	: Modified Gravity
FLRW	: Friedmann Lemaître Robertson Walker
MCMC	: Markov Chain Monte Carlo
SNe Ia	: Type Ia Supernova
CC	: Cosmic Chronometers
OHD	: Observational Hubble Data
EC	: Energy Conditions
WEC	: Weak Energy Condition
NEC	: Null Energy Condition
SEC	: Strong Energy Condition
DEC	: Dominant Energy Condition
LC	: Levi Civita
WC	: Weitzenböck Connection
STG	: Symmetric Teleparallel Geometry

Chapter 1

Introduction

The study of cosmology aims to explain the history and future of the Universe, from its birth to ultimate fate. The standard cosmological model is based on the cosmological principle, which states that the Universe is homogeneous and isotropic on large scales. Einstein's General Relativity (GR) Theory expanded upon this by providing a more comprehensive framework for understanding gravity, especially in regions of intense gravitational forces [1, 2]. GR not only predicted black holes but also anticipated the existence of gravitational waves, both of which have since been observed, confirming Einstein's theories. In 1917, he proposed a static model of the Universe, introducing a cosmological constant to counteract gravitational forces [3]. However, the model was abandoned when it became clear that the Universe was not static but expanding. Russian mathematician, Alexander Friedmann found solutions to Einstein's equations that showed an expanding Universe, which set the stage for the Big Bang theory. According to this model, the Universe is believed to have begun from an incredibly hot and dense state approximately 13 billion years ago, which is radically transforming our understanding of its origin [4]. The expansion of the Universe was first observed by Edwin Hubble in 1929 [5], who found that galaxies were receding from us at velocities proportional to their distance, a relationship now known as Hubble's law, $v = H_0 d$ [6]. Following this, Friedmann [4, 7], Lemaître [8], Robertson [9] and Walker [10] presented new solutions to Einstein's field equation for an expanding Universe. These contributions led to the development of the FLRW metric, which became the fundamental aspect of modern cosmology, describing the Universe that is both homogeneous and isotropic at large scales and expanding over time.

This discovery, along with the later detection of the CMB radiation in 1965 by Penzias and Wilson, provided crucial evidence supporting the Big Bang theory and the expansion of the Universe. However, when examining the smaller scales, the Universe is far from the uniform can be observed. It is filled with galaxies, galaxy clusters and vast voids, revealing an inhomogeneous structure at scales smaller than about 350 Mpc [11, 12]. Moreover, the CMB radiation, a remnant of the Big Bang shows minute fluctuations that suggest slight variations in temperature, but these are incredibly small on the order of one part in 10^5 [13]. Following that, significant advances were made in both theoretical and observational fields. Starobinsky [14, 15], Guth [16]

and Linde [17] proposed cosmic inflation in the late 1970s and early 1980s to explain the origin of large-scale structures of the Universe. An exponential expansion is described in this theory, which also addresses the problems of horizons, flatness and monopoles. The first inflationary models were applied by Guth in 1981. He proposed that large-scale structures were formed from the gravitational collapse of perturbations after quantum fluctuations during inflationary periods [16]. The standard cosmological model describes how matter and energy influence the curvature of spacetime, dictating the behavior of the Universe.

In the early 20th century, advancements in technology played a crucial role in confirming the existence of galaxies beyond our own, with observations revealing that these galaxies were all moving away from us [18]. The late 1990s brought a new understanding of the evolution of the Universe. According to observations of SNe Ia in 1998, the Universe is expanding more rapidly than previously believed. According to two groups, Riess and Schmidt [19–21] (High-Z Supernova Search Team), measured the luminosity distances of SNe Ia, which are candles with a fixed intrinsic brightness and Perlmutter (Supernova Cosmology Project) [22], galaxies and clusters are moving apart at an accelerated rate. This discovery which contradicted previous expectations that gravity should slow the expansion, suggested the presence of an unknown force later considered as Dark Energy. More recent observations from the Planck satellite [23] confirmed that ordinary matter constitutes only about 4–5% of the total content of the Universe, with DM and DE making up the rest approximately 25% and 70%, respectively. These findings led to the development of the Λ CDM model, which assumes that the expansion of the Universe is driven by DE and that DM plays a crucial role in structuring the cosmic landscape.

A brief overview of the accelerated expansion of the Universe is presented in this chapter, followed by an introduction to statistical analysis methods and the stability analysis used for reconstruction in cosmology. For more information on modern cosmology, see standard literature [24–29].

1.1 Geometric Setup

The development of the theory of gravitation in the initial phase focuses on establishing a mathematical framework that allows us to express the laws of physics in a covariant manner. This is achieved through the use of vectors and tensors, which are mathematical entities that transform in line with the principles of covariance. This section examines the key differential operations derived from these vectors and tensors. One can find more information on these concepts in [30].

Definition 1.1 (Metric tensor). The metric tensor is a mathematical object that describes the geometry of a coordinate system or manifold. The components of the metric describe lengths, angles and other geometric quantities. The components of the metric tensor are defined as the dot product between basis vectors and is given by

$$g_{\mu\nu} = \vec{e}_\mu \cdot \vec{e}_\nu , \quad (1.1)$$

where, $g_{\mu\nu}$ are the components of the metric tensor and these e 's are the basis vectors in whatever coordinate system we are using.

Definition 1.2 (Christoffel symbol). The Christoffel symbol, derived from the metric tensor, is a key component in differential geometry. It is defined as,

$$\{\alpha_{\mu\nu}\} = \frac{1}{2}g^{\alpha\lambda}(\partial_\mu g_{\nu\lambda} + \partial_\nu g_{\lambda\mu} - \partial_\lambda g_{\mu\nu}) . \quad (1.2)$$

Christoffel symbol is not a tensor itself, despite having three indices and resembling a tensor. By definition, it is symmetric in the lower pair of indices μ and ν . Therefore, in n dimensions, it has $\frac{n(n+1)}{2}$ symmetric components for the lower indices. The third index α can take any value independently, leading to a total of $\frac{n^2(n+1)}{2}$ independent components in n dimensions. The Christoffel symbol plays a crucial role in the computation of covariant derivatives, which extend the concept of partial derivatives to curved spaces.

Definition 1.3 (Covariant derivative). The covariant derivative mathematically defined as,

$$\nabla_\mu A^\nu = \partial_\mu A^\nu + \{\nu_{\mu\lambda}\} A^\lambda . \quad (1.3)$$

An operator ∇ known as covariant derivative, acts on tensors to yield a tensor in a manner that is entirely coordinate independent. Furthermore, the general expression for the covariant derivative is

$$\begin{aligned} \nabla_\lambda A^{\mu_1\mu_2\dots\mu_n}_{\nu_1\nu_2\dots\nu_m} &= \partial_\lambda A^{\mu_1\mu_2\dots\mu_n}_{\nu_1\nu_2\dots\nu_m} + \{\mu_1_{\lambda\sigma}\} A^{\sigma\mu_2\dots\mu_n}_{\nu_1\nu_2\dots\nu_m} + \dots + \{\mu_n_{\lambda\sigma}\} A^{\mu_1\mu_2\dots\sigma}_{\nu_1\nu_2\dots\nu_m} \\ &\quad - \{\sigma_{\lambda\nu_1}\} A^{\mu_1\mu_2\dots\mu_n}_{\sigma\nu_2\dots\nu_m} - \dots - \{\sigma_{\lambda\nu_m}\} A^{\mu_1\mu_2\dots\mu_n}_{\nu_1\nu_2\dots\sigma} \end{aligned} \quad (1.4)$$

Definition 1.4 (Parallel transport). The process of moving a vector along a curve in such a way that its orientation remains unchanged relative to the underlying manifold is known as parallel transport. Consider a path parameterized by $x^\mu(\lambda)$ with a tangent vector given by $\frac{dx^\mu}{d\lambda}$. If a vector A^μ satisfies the condition

$$\frac{dx^\mu}{d\lambda} \cdot \nabla_\mu A^\nu = 0 . \quad (1.5)$$

then it is said to be parallel transported along the path $x^\mu(\lambda)$.

This condition implies that there is no “change” in the components of the vector due to the curvature of the space.

Definition 1.5 (Geodesic). A geodesic is a mathematical concept that extends the notion of a straight line in Euclidean geometry to curved spaces. Given two points connected by a curve, the arc length allows us to quantify the distance traversed along that path. The focus is on those curves, termed geodesics, that minimize this distance, as they are critical in understanding

the intrinsic geometry of the space in question. If the curve or path $x^\mu(\lambda)$ satisfies the equation

$$\frac{d^2x^\mu}{d\lambda^2} + \{\mu_{\delta\sigma}\} \frac{dx^\delta}{d\lambda} \frac{dx^\sigma}{d\lambda} = 0, \quad (1.6)$$

then the curve or path $x^\mu(\lambda)$ is said to be a geodesic. Where $\{\mu_{\delta\sigma}\}$ is the Christoffel symbol.

Definition 1.6 (Non-metricity Tensor). The non-metricity tensor is defined as,

$$Q_{\lambda\mu\nu} = \nabla_\lambda g_{\mu\nu}. \quad (1.7)$$

The non-metricity tensor is symmetric in the last two indices by definition as $Q_{\lambda\mu\nu} = Q_{\lambda(\mu\nu)}$. Expanding the covariant derivative, the dependence of non-metricity in both the metric tensor $g_{\mu\nu}$ and the connection coefficients $\Gamma^\alpha_{\lambda\mu}$ becomes apparent. This relationship is expressed as,

$$Q_{\lambda\mu\nu} = \partial_\lambda g_{\mu\nu} - \Gamma^\alpha_{\lambda\mu} g_{\alpha\nu} - \Gamma^\alpha_{\lambda\nu} g_{\alpha\mu}. \quad (1.8)$$

It is crucial to exercise caution while raising and lowering indices in the context of non-metricity, as the operations of covariant differentiation and index manipulation are no longer commutative. Consequently, one must apply the Leibniz rule whenever covariant derivatives are involved to ensure accuracy in calculations.

Definition 1.7 (Superpotential tensor). The conjugate of the Non-metricity tensor is a tensor of the type (1, 2), called as superpotential tensor and is given by,

$$P^\lambda_{\mu\nu} = -\frac{1}{4}Q^\lambda_{\mu\nu} + \frac{1}{4}\left(Q^\lambda_{\mu\nu} + Q^\lambda_{\nu\mu}\right) + \frac{1}{4}Q^\lambda g_{\mu\nu} - \frac{1}{8}\left(2\tilde{Q}^\lambda g_{\mu\nu} + \delta^\lambda_\mu Q_\nu + \delta^\lambda_\nu Q_\mu\right), \quad (1.9)$$

where, $Q_\alpha = Q_\alpha^\mu \mu$ and $\tilde{Q}_\alpha = Q^\mu_{\alpha\mu}$ are two traces of non-metricity.

Definition 1.8 (Non-metricity scalar). The non-metricity scalar that will play a central role is given by $Q = Q_{\lambda\mu\nu} P^{\lambda\mu\nu}$. A different definition of $Q = -Q_{\lambda\mu\nu} P^{\lambda\mu\nu}$ has been proposed in the literature, which changes the sign of the non-metricity scalar Q . This is important to consider while comparing different $f(Q)$ results.

So far, key mathematical concepts and techniques necessary for developing the mathematical framework have been explored. The focus will now shift to some cosmological aspects.

1.2 Foundation of Cosmological Dynamics

This section provides an overview of the standard cosmological model. For a thorough introduction to cosmology one may refer to Weinberg [24], which delves into critical concepts such as FLRW metric, Hubble parameter, redshift, fluid equations governing cosmic dynamics and an analysis of the successes and limitations inherent in the Λ CDM framework.

1.2.1 The FLRW metric

The cosmological principle states that, on sufficiently large scales, the Universe is both homogeneous and isotropic. Homogeneity means that the Universe appears consistent to observers regardless of their location, while isotropy indicates that there are no favored directions from any given viewpoint. Assuming a homogeneous Universe, any two particles can be transformed to a different coordinate system known as comoving coordinates. These are coordinates which are carried along with the expansion. Because the expansion is uniform, the relationship between real distance \vec{r} and the comoving distance, which can be called as \vec{x} , can be written $\vec{r} = a(t) \vec{x}$. The scale factor, $a(t)$ describes how physical distances evolve over time. The work of Friedmann, Lemaître, Robertson and Walker leads to the following expression for the line element in spherical coordinates, reflecting the geometric characteristics of homogeneity and isotropy while accounting for the expansion of the Universe,

$$ds^2 = -c^2 dt^2 + a^2(t) \left[\frac{dr^2}{1 - \kappa r^2} + r^2 d\theta^2 + r^2 \sin^2 \theta d\phi^2 \right]. \quad (1.10)$$

In spherical geometry, (r, θ, ϕ) represent the comoving spatial coordinates and the spatial curvature is denoted by κ . For convenience, $c = 1$ is set.

Additionally, depending on the value of κ (zero, positive or negative) there are three possible geometries for the Universe.

- **Flat geometry:** These laws are based on the Euclidean geometry axioms (e.g. a straight line is the shortest distance between two points) plus one more axiom, which says parallel straight lines must remain a fixed distance apart. A Universe with the geometry ($\kappa = 0$) is called a flat Universe.
- **Spherical geometry:** A Universe with spherical geometry similar to the surface of the Earth, has a finite size but no boundaries. In spherical geometry, traveling in a straight line would not result in an endless journey. Instead, after covering a certain distance, the traveler would eventually return to the starting point, coming from the opposite direction. This is similar to how a journey starting at the North pole leads back to the same spot after traveling outward, but from the opposite direction. A Universe with $\kappa > 0$ is referred to as a closed Universe because of its finite size.
- **Hyperbolic geometry:** The choice $\kappa < 0$ is referred as the hyperbolic geometry. The hyperbolic geometry is much less familiar than spherical geometry. It is typically represented by a saddle-like surface. While it may be difficult to see how this is consistent with isotropy. In this type of geometry, parallel lines never meet; they violate Euclid's axiom by diverging from each other. The situation $\kappa < 0$ is known as an open Universe.

Additional parameters essential for understanding the dynamics of the expansion of the Universe will be introduced before deriving the Friedmann equations and their solutions.

TABLE 1.1: A summary of possible geometries.

Curvature	Geometry	Angles of triangle	Circumference of circle	Type of Universe
$\kappa > 0$	Spherical	> 180	$< 2\pi r$	Closed
$\kappa = 0$	Flat	$= 180$	$= 2\pi r$	Flat
$\kappa < 0$	Hyperbolic	< 180	$> 2\pi r$	Open

1.2.2 Redshift in cosmology

The observation that nearly everything in the Universe is moving away from us and that this movement accelerates with distance is a key finding in cosmology. As photons travel through space, they are affected by the expansion of the Universe, which stretches their wavelengths. This phenomenon causes photons to lose energy. When these photons start in the visible spectrum, they initially appear blue and energetic but shift to red as their energy decreases. This change in wavelength is known as redshift.

In cosmological terms, by utilizing the observed wavelength (λ_{ob}) and the wavelength at emission (λ_{em}), the redshift is denoted as z and defined by the equation

$$z = \frac{\lambda_{\text{ob}} - \lambda_{\text{em}}}{\lambda_{\text{em}}} . \quad (1.11)$$

According to the Doppler effect, the difference in wavelength relates to the velocity of the object

$$\frac{\lambda_{\text{ob}} - \lambda_{\text{em}}}{\lambda_{\text{em}}} = \frac{dv}{c} , \quad (1.12)$$

where $\lambda_{\text{ob}} > \lambda_{\text{em}}$. The time it takes for light to travel from emission to observation is given by $dt = \frac{dr}{c}$. This leads to

$$\frac{\lambda_{\text{ob}} - \lambda_{\text{em}}}{\lambda_{\text{em}}} = \frac{\dot{a} \frac{dr}{c}}{\dot{a} \frac{dt}{c}} = \frac{\dot{a}}{a} dt = \frac{da}{a} . \quad (1.13)$$

From this, it follows that $\lambda \propto a$, where λ is the instantaneous wavelength. Therefore, redshift can be expressed in terms of the scale factor as:

$$1 + z = \frac{\lambda_{\text{ob}}}{\lambda_{\text{em}}} = \frac{a(t_{\text{ob}})}{a(t_{\text{em}})} . \quad (1.14)$$

The relationship between redshift and the scale factor is crucial for understanding the expansion of the Universe. In the next section, we will delve into the concept of energy conservation in cosmology.

1.2.3 Energy conservation in cosmology

The Friedmann equation provides a framework for understanding cosmic evolution, but it alone cannot fully describe how the scale factor $a(t)$ and energy density ρ change over time. To resolve

this, a concept from thermodynamics specifically the first law can be used as,

$$dQ = dE + p dV , \quad (1.15)$$

where, p is pressure, dQ is the heat exchange, dE is the change in internal energy and dV is the change in volume. In a homogeneous Universe, $dQ = 0$ indicating no bulk heat flow is assumed. This allows us to express energy conservation as,

$$\dot{E} + p\dot{V} = 0 . \quad (1.16)$$

Consider a sphere with a comoving radius r_s that expands with the Universe, giving it a proper radius of $R_s(t) = a(t)r_s$. The volume of this sphere is given by,

$$V(t) = \frac{4}{3}\pi r_s^3 a^3(t) . \quad (1.17)$$

Thus, the rate of change of the volume is

$$\dot{V} = \frac{4}{3}r_s^3(3a^2\dot{a}) = V\left(3\frac{\dot{a}}{a}\right) . \quad (1.18)$$

The internal energy of the sphere can be expressed as,

$$E(t) = V(t)\rho(t) . \quad (1.19)$$

Taking the time derivative, the result is found to be

$$\dot{E} = V\dot{\rho} + \dot{V}\rho = V\left(\dot{\rho} + 3\frac{\dot{a}}{a}\rho\right) . \quad (1.20)$$

Substituting equations for \dot{E} and \dot{V} into the energy conservation equation, the result is

$$V\left(\dot{\rho} + 3\frac{\dot{a}}{a}(\rho + p)\right) = 0 . \quad (1.21)$$

This leads to the fluid equation, which governs the dynamics of the expansion of the Universe

$$\dot{\rho} + 3\frac{\dot{a}}{a}(\rho + p) = 0 . \quad (1.22)$$

This equation must apply to each cosmological component independently, provided there is no interaction between them. Hence for each component i , the following holds

$$\dot{\rho}_i + 3H(\rho_i + p_i) = 0 . \quad (1.23)$$

If the EoS parameter ω_i is introduced for each component, the continuity equation can be rewritten as

$$\dot{\rho}_i + 3H(1 + \omega_i)\rho_i = 0 . \quad (1.24)$$

Rearranging this leads to

$$\frac{d\rho_i}{\rho_i} = -3(1 + \omega_i) \frac{da}{a} . \quad (1.25)$$

The continuity equation can be integrated to find the dependence of energy density on the scale factor, assuming ω_i is constant.

$$\rho_i(a) = \rho_{i0} a^{-3(1+\omega_i)} . \quad (1.26)$$

For specific cases, the energy densities for nonrelativistic matter ($\omega_m = 0$) and radiation ($\omega_r = \frac{1}{3}$) are respectively given as

$$\rho_m(a) = \frac{\rho_{m0}}{a^3} = \rho_{m0}(1+z)^3 , \quad \rho_r(a) = \frac{\rho_{r0}}{a^4} = \rho_{r0}(1+z)^4 . \quad (1.27)$$

This framework enables the modeling of energy density evolution for different components in an expanding Universe.

The next section will focus on exploring how the specific energy-momentum tensor characterizes different categories of matter sources.

1.2.4 The stress-energy-momentum tensor

This section analyzes the properties of the stress-energy-momentum tensor for a Universe characterized by homogeneity and isotropy, filled with a perfect fluid¹. The equation for the stress-energy-momentum tensor is

$$\mathcal{T}_{\mu\nu} = (\rho + p) u_\mu u_\nu + p g_{\mu\nu} . \quad (1.28)$$

In the context of isotropic fluid dynamics, the symbols ρ represent the energy density and p represent the pressure of the fluid, while u_μ denotes the covariant 4-velocity of an observer moving with the fluid. It is important to note that the functions ρ and p are purely time dependent (t) and do not have any spatial dependence. Friedmann Universe is characterized by isotropy and homogeneity, which restrict the possibility of vector-like dependence. Since isotropy forbids vector-like dependence and homogeneity eliminates spatial dependence, therefore only time dependence remains. Again since mathematical quantities are time dependent scalars in an isotropic and homogeneous Universe, they are represented by $f(t)$.

Furthermore, it is important to note that the stress-energy-momentum tensor adheres to the conservation condition represented by the equation $\nabla^\mu \mathcal{T}_{\mu\nu} = 0$, which leads to

$$\dot{\rho} + 3\frac{\dot{a}}{a}(\rho + p) = 0 . \quad (1.29)$$

After outlining the properties of the stress-energy-momentum tensor, attention is now directed to the energy conditions, which impose further constraints on the behavior of matter and energy in the Universe.

¹In the context of a continuous matter component, the absence of shear stress implies that viscosity can be disregarded.

1.2.5 Energy conditions

An energy conditions play a pivotal role in cosmology as they govern how matter and energy behave in spacetime by providing constraints on the stress-energy tensor $T_{\mu\nu}$. These conditions, which are formulated to be coordinate invariant, allow us to understand gravitational systems without detailed knowledge of the matter content. They are essential for the study of singularities, black holes and the dynamics of the Universe, as demonstrated in Penrose and Hawking's singularity theorems [31, 32].

The following energy conditions are derived from the well-known Raychaudhuri equations [33–35],

$$\frac{d\theta}{d\tau} = -\frac{1}{3}\theta^2 - \sigma_{\mu\nu}\sigma^{\mu\nu} + \omega_{\mu\nu}\omega^{\mu\nu} - R_{\mu\nu}u^\mu u^\nu, \quad (1.30)$$

$$\frac{d\theta}{d\tau} = -\frac{1}{2}\theta^2 - \sigma_{\mu\nu}\sigma^{\mu\nu} + \omega_{\mu\nu}\omega^{\mu\nu} - R_{\mu\nu}n^\mu n^\nu, \quad (1.31)$$

where θ is the expansion scalar, $\sigma^{\mu\nu}$ represents shear and $\omega_{\mu\nu}$ denotes rotation associated with the geodesic congruences defined by vectors u^μ and n^μ . These conditions are typically expressed by constructing scalars from $T_{\mu\nu}$ using arbitrary timelike vectors t^μ or null vectors n^μ [36, 37]. In cosmology, EC are used to define normal matter and help establish general properties of

Energy conditions	Physical form	Geometrical form	Perfect fluid
WEC	$T_{\mu\nu}t^\mu t^\nu \geq 0$	$G_{\mu\nu}t^\mu t^\nu \geq 0$	$\rho \geq 0,$ $\rho + p \geq 0$
NEC ^c	$T_{\mu\nu}\xi^\mu \xi^\nu \geq 0$	$R_{\mu\nu}\xi^\mu \xi^\nu \geq 0$	$\rho + p \geq 0$
SEC	$(T_{\mu\nu} - \frac{1}{2}g_{\mu\nu})t^\mu t^\nu \geq 0$	$R_{\mu\nu}t^\mu t^\nu \geq 0$	$\rho + p \geq 0,$ $\rho + 3p \geq 0$
DEC	$T_{\mu\nu}t^\mu t^\nu \geq 0$ and $T_{\mu\nu}t^\mu$ is non-space-like	$G_{\mu\nu}t^\mu t^\nu \geq 0$ and $G_{\mu\nu}t^\mu$ is non-space-like	$\rho \geq p $

TABLE 1.2: Energy conditions with their physical and geometrical significance.

the Universe. The four main EC are the Weak Energy Condition, Null Energy Condition, Strong Energy Condition and Dominan Energy Condition. In terms of validity, significance and interpretation, each of these EC has its own advantages and limitations. Additionally, each condition imposes different constraints on the energy density, ρ and pressure, p of matter.

- **WEC** states that the energy density must be non-negative ($\rho \geq 0$) and the pressure must satisfy $\rho + p \geq 0$, ensuring that energy is physically meaningful and not excessively negative.
- **NEC** requires that $\rho + p \geq 0$. It allows for negative energy density if compensated by sufficiently large pressure, playing a role in the study of lightlike geodesics and black hole horizons.

- **SEC** is key for understanding the large-scale structure and evolution of the Universe. It implies that $\rho + p \geq 0$ and $\rho + 3p \geq 0$, which suggests that gravity is attractive and leads to a decelerating expansion of the Universe under normal matter conditions. It is also important in analyzing cosmic phenomena such as the formation of singularities in black holes and the Big Bang.
- **DEC** combines WEC with a requirement that the energy flux be non-spacelike, meaning that $\rho \geq |p|$. This ensures that the energy density is non-negative and at least as large as the absolute value of pressure, implying that matter behaves in a physically reasonable way.

The SEC is particularly important for understanding the acceleration phenomena in the Universe. Therefore, the upcoming discussion will concentrate on the SEC.

The following section discusses the cosmological parameters that are commonly considered.

1.2.6 Cosmographic parameters

Cosmologists aim to determine the scale factor $a(t)$, which describes the expansion of the Universe. In models where the contents of the Universe are well understood, this scale factor can be derived from the Friedmann equations. However, establishing $a(t)$ for the actual Universe is complex. The scale factor itself is not directly measurable; it must be inferred from our limited and sometimes imperfect observations [29]. According to the cosmological principle, the scale factor represents a fundamental degree of freedom that governs the dynamics of the Universe. The scale factor $a(T)$ is determined as a Taylor expansion [24] around the present time t_0 . This gives

$$a(t) \approx a(t_0) + \dot{a}(t_0)\Delta t + \frac{\ddot{a}(t_0)}{2!}\Delta t^2 + \frac{\dddot{a}(t_0)}{3!}\Delta t^3 + \frac{a^{(iv)}(t_0)}{4!}\Delta t^4 + \frac{a^{(v)}(t_0)}{5!}\Delta t^5 + \dots, \quad (1.32)$$

which recovers signal causality if one assumes $\Delta t \equiv t - t_0 > 0$. From the above expansion of $a(t)$, one defines

$$H \equiv \frac{1}{a} \frac{da}{dt}, \quad q \equiv -\frac{1}{aH^2} \frac{d^2a}{dt^2}, \quad j \equiv \frac{1}{aH^3} \frac{d^3a}{dt^3}, \quad s \equiv \frac{1}{aH^4} \frac{d^4a}{dt^4}, \quad l \equiv \frac{1}{aH^5} \frac{d^5a}{dt^5}. \quad (1.33)$$

These functions can be directly constrained by observations, as they are model independent quantities by construction, i.e. they do not rely on the specific form of the DE fluid. They are known in the literature as the Hubble parameter (H), the deceleration parameter (q), the jerk parameter (j), the snap parameter (s) and the lerk parameter (l) [38, 39]. Once these functions are determined at the present time, they are referred to as the cosmographic series. This is the set of coefficients usually derived in cosmography from observations. Rewriting $a(t)$ in terms of the cosmographic series gives

$$a(t) \approx 1 + H_0\Delta t - \frac{q_0}{2!}H_0^2\Delta t^2 + \frac{j_0}{3!}H_0^3\Delta t^3 + \frac{s_0}{4!}H_0^4\Delta t^4 + \frac{l_0}{5!}H_0^5\Delta t^5 + \dots, \quad (1.34)$$

The scale factor is normalized by setting $a(t_0) = 1$. Reformulating Eq. (1.32) into the form shown in Eq. (1.34) describes the significance of each parameter within the cosmographic series. Each term reveals distinct dynamical characteristics, with the parameter s and the parameter l specifically influencing the profile of Hubble's flow in the high redshift regime. It is essential for the Hubble parameter to be positive to ensure the continued expansion of the Universe. Furthermore, the parameters q and j characterize the kinematics at lower redshift domains. Notably, the value of q at any instant provides insight into whether the Universe is undergoing acceleration or deceleration and hints at the nature of the cosmological fluid driving these dynamics.

Attention is now directed to the simplest model of the Universe, which will serve as the foundation for the discussion.

1.2.7 Overview of the Λ CDM model

The Λ CDM model is designed to explain the dynamics of the Universe, specifically the phenomenon of accelerated expansion. This framework includes GR while incorporating dark energy characterized by a negative EoS parameter, conventionally represented as a cosmological constant. Within GR, the introduction of a cosmological constant permits accelerated expansion; however, the fundamental origins of this DE remains unexplained. This topic will be examined in further detail in the subsequent sections. For this discussion, natural units are employed where c and \hbar (the reduced Planck constant) are set to unity, unless stated otherwise.

In 1915, Einstein's theory of GR was derived from the Einstein-Hilbert action, which is given by

$$S = \int d^4x \sqrt{-g} \left[\frac{1}{2\kappa} (R + 2\Lambda) + L_m \right], \quad (1.35)$$

where $\kappa = 8\pi G$ and Λ is the cosmological constant. The Einstein field equation can be obtained by the variation of the Einstein-Hilbert action with respect to the metric tensor, leads to

$$G_{\mu\nu} + \Lambda g_{\mu\nu} = \kappa \mathcal{T}_{\mu\nu}. \quad (1.36)$$

Additionally, the cosmological equations of the Λ CDM model, commonly referred to as the Friedmann equations, are explored. The equations are derived using the FLRW metric (1.10), the stress-energy-momentum (1.28) and Eq. (1.36), resulting in

$$H^2 = \frac{8\pi G}{3}\rho - \frac{k}{a^2} + \frac{\Lambda}{3}, \quad (1.37)$$

$$2\dot{H} + 3H^2 = -8\pi Gp - \frac{k}{a^2} + \Lambda. \quad (1.38)$$

Combining equations (1.37) and (1.38) gives

$$\frac{\ddot{a}}{a} = -\frac{4\pi G}{3}(\rho + 3p) + \frac{\Lambda}{3}, \quad (1.39)$$

which is known as the acceleration equation. If $\ddot{a} > 0$, the Universe experiences acceleration, while $\ddot{a} < 0$ indicates a decelerating Universe. For the geometry of the Universe to be flat corresponding to $k = 0$, there is a specific density that must be present for a given value of the Hubble parameter, H . This density is referred to as the critical density ρ_c and it is calculated as,

$$\rho_c = \frac{3H^2}{8\pi G} . \quad (1.40)$$

The critical density is a key concept, but it does not always match the actual density of the Universe because the Universe does not have to be perfectly flat. As a result, it is often more useful to express the density of the Universe in relation to the critical density, rather than quoting its absolute value directly. This quantity is known as the density parameter Ω and defined as

$$\Omega_i(t) = \frac{\rho_i(t)}{\rho_c(t)} = \frac{8\pi G}{3} \frac{\rho_i(t)}{H^2(t)} , \quad (1.41)$$

where i denotes the sum over matter, radiation, spatial curvature and vacuum. One can rewrite the Friedmann equation (1.37) as

$$1 = \Omega_m(t) + \Omega_r(t) + \Omega_k(t) + \Omega_\Lambda(t) .$$

$$\Omega_m(t) = \frac{8\pi G}{3H^2} \rho_m(t) , \quad \Omega_r(t) = \frac{8\pi G}{3H^2} \rho_r(t) , \quad \Omega_k(t) = -\frac{k}{H^2 a^2} , \quad \Omega_\Lambda(t) = \frac{8\pi G}{3H^2} \rho_\Lambda , \quad \rho_\Lambda = \frac{\Lambda}{8\pi G} \quad (1.42)$$

For flat geometry ($k = 0$), $\Omega_m + \Omega_r + \Omega_\Lambda = 1$, i.e. $\Omega_{total} = 1$ at all times. The values of Ω_i change over time, so at the present moment, they are referred to as Ω_{i_0} . This allows us to understand how different components of the Universe such as matter, dark energy and radiation contribute to the overall density relative to the critical density at the specific time.

$$H(z) = H_0 \sqrt{\left(\Omega_{r_0} (1+z)^4 + \Omega_{m_0} (1+z)^3 + \Omega_{k_0} (1+z)^2 + \Omega_{\Lambda_0} \right)} . \quad (1.43)$$

The Planck collaboration [40] findings provided precise values for the parameters in Eq. (1.43), refining our understanding of the composition and evolution of the Universe. The next section explores both the successes and limitations of the standard cosmological model.

1.2.8 Successes and shortcomings of standard cosmological model

The standard cosmological model Λ CDM has been remarkably successful in describing the evolution of the Universe and structure. It incorporates both the theory of GR and the concept of a cosmological constant (Λ) to account for various observed phenomena. Here are some of the major successes of the Λ CDM model:

- **Cosmic evolution and structure formation:** The Λ CDM model successfully explains the large-scale structure of the Universe, including the formation and distribution of

galaxies and galaxy clusters. It incorporates the effects of DM and DE to describe how structures form and evolve over time through gravitational interactions.

- **Primordial nucleosynthesis:** The model accurately predicts the abundances of light elements such as Helium, Deuterium and Lithium, as observed in the Universe today. These predictions stem from the processes of primordial nucleosynthesis that occurred during the first few minutes after the Big Bang.
- **CMB:** The Λ CDM model aligns well with observations of the CMB, which provides a snapshot of the Universe approximately 380,000 years after the Big Bang. The model reproduces the observed temperature fluctuations and the angular power spectrum of the CMB with high precision.
- **Accelerated expansion of the Universe:** The model accounts for the observed accelerated expansion of the Universe, attributed to DE. Observations of distant supernovae and the large-scale structure of the Universe support this explanation, fitting well with the predictions made by Λ CDM.

Despite these successes, the Λ CDM model faces several significant challenges:

- **Cosmological constant problem:** There is a profound discrepancy between the theoretical and observed values of the cosmological constant, which differs by about 60 orders of magnitude. Theoretical estimates based on quantum field theory suggest a value of $10^{-60} M_{Pl}^4$, whereas observations indicate a value of $10^{-120} M_{Pl}^4$ [41]. This discrepancy is known as the cosmological constant problem.
- **Horizon problem:** The Λ CDM model encounters the horizon problem, which refers to the difficulty in explaining the uniform temperature of the Universe across regions that are not in causal contact. The widely accepted resolution is the theory of cosmic inflation, which proposes that the Universe underwent exponential expansion during its early stages [42].
- **Cosmological coincidence problem:** The model suggests that the Universe is in a transitional phase between the matter-dominated era and a period of accelerated expansion driven by DE. Observations show that the densities of DE and DM are of comparable magnitude, which raises questions about why these quantities are so similar [43].
- **DM:** While Λ CDM assumes the presence of DM, which is non-baryonic and interacts only through gravity, no direct detection of DM particles has been achieved. The model relies on DM to explain phenomena such as the rotational curves of galaxies and the formation of large-scale structures [44–46].
- **H_0 tension:** There is a notable discrepancy between the local measurements of the Hubble constant (H_0) and those derived from CMB observations. This discrepancy, known as H_0 tension, amounts to approximately 4.4σ tension [47].

- σ_8 **tension:** There is also tension regarding the amplitude of cosmic structure growth. The Planck collaboration estimates $S_8 = \sigma_8 \sqrt{\Omega_m/0.3} = 0.834 \pm 0.016$ [48, 49], while the KIDS-450 collaboration finds $S_8 = 0.745 \pm 0.039$ [50], resulting in about 2σ tension.

These challenges highlight the need for alternative theories or modifications to the Λ CDM model. The following sections will explore various models that attempt to address these limitations and extend beyond the standard Λ CDM framework.

1.3 Exploring Alternative Cosmological Theories

Given the limitations of the Λ CDM model discussed previously, it is essential to explore alternative approaches that extend beyond Λ CDM and GR. This section will discuss potential alternatives to GR, driven by the shortcomings associated with the cosmological constant. These alternatives generally fall into two categories: DE models and Modified Gravity models.

1.3.1 Dark energy models

These models introduce a DE component characterized by either a static or dynamic equation of state. Rather than relying on the cosmological constant Λ , DE models modify the matter side of Einstein's equation, typically by incorporating additional fluid components.

- There have been several dynamical dark energy models proposed with time dependent EoS parameter during the evolution of the Universe. Some common dynamical dark energy models, as functions of redshift z , are Chevallier-Polarski-Linder (CPL) model [51], Jassal-Bagla-Padmanbhan (JBP) model [52], Barboza-Alcaniz parameterization [53] and Wetterich parameterization [54] and many more.
- The quintessence scalar field model is a prominent framework for describing dynamical DE. This model involves a scalar field that is minimally coupled to matter, characterized by a time dependent scalar field ϕ and an associated potential $V(\phi)$. The negative pressure generated by the scalar field drives a decrease in the potential over time. Quintessence models are classified according to the form of the potential. In scenarios where $V(\phi) \ll \dot{\phi}^2$, the EoS parameter approximates to $\omega \approx 1$, resembling stiff matter and yielding negligible contributions to DE. Conversely, when $V(\phi) \gg \dot{\phi}^2$, the EoS parameter approaches $\omega \approx -1$, akin to a cosmological constant. For intermediate cases where $-1 < \omega < 1$, the energy density behaves as $\rho \propto a^{-m}$, facilitating accelerated expansion for $0 \leq m < 2$. For a deeper exploration of the diverse quintessence potentials and their implications for late-time cosmic acceleration [55–58].
- Caldwell [59] introduced the phantom field model of DE was proposed to explain the late-time cosmic acceleration. In this model, the kinetic term carries a negative sign,

leading to negative kinetic energy, which leads to an accelerated expansion of the Universe to an infinite size within a finite amount of time, a scenario known as the big rip. Scalar field models whose EoS evolution mimics that of the phantom field are called quintom models. These models combine features of both quintessence and phantom fields, allowing for a more flexible description of DE behavior, particularly in the transition between different epochs of cosmic acceleration [60, 61].

- The K-essence scalar field model describes an inflationary model of the early Universe, also known as K-inflation [62–64]. Unlike quintessence models, which primarily rely on the potential energy term to drive accelerated expansion, K-essence models are characterized by a dominant kinetic contribution to the energy density, which plays a key role in explaining late-time cosmic acceleration.

1.3.2 Modified gravity models

There is an alternative approach to explaining the late-time acceleration of the Universe that involves modifying Einstein's GR. Various modified gravity theories propose mechanisms for accelerated expansion without relying on a dark energy component [65, 66]. These theories include $f(R)$ gravity [67–73], scalar-tensor models [74–79], $f(T)$ gravity [80–84], $f(Q)$ gravity [85–90] and other extended gravitational theories [91–95]. As a result of these alternative frameworks present different mechanisms to explain cosmic acceleration, each highlighting distinct aspects of fundamental properties and dynamics of the gravity.

- **$f(R)$ gravity** is a generalization of the Einstein-Hilbert action, where the Ricci scalar R is replaced by a more general function $f(R)$. This allows for different gravitational behaviors and dynamics. $f(R)$ gravity can provide alternative explanations for the accelerated expansion of the Universe, without relying on dark energy. Different choices of $f(R)$ can lead to varied cosmological models and predictions.
- **$f(T)$ gravity** is a modified theory of gravity based on the TEGR. It uses the torsion scalar T instead of the Ricci scalar to describe gravitational interactions. $f(T)$ gravity offers different predictions for cosmic expansion and structure formation compared to $f(R)$ gravity, potentially providing new insights into the accelerated expansion of the Universe.
- **$f(Q)$ gravity** is a modified theory that extends GR by considering a function of the non-metricity scalar Q . This theory utilizes the non-metricity of spacetime, which refers to the variation of the metric tensor. $f(Q)$ gravity provides an alternative framework for understanding cosmic acceleration by modifying the role of non-metricity, leading to different cosmological models and predictions.

We discuss one of the popular theory of modified gravity in the next section.

1.4 Symmetric Teleparallelism

To better understand DM and DE, various modified theories of gravity have been proposed that go beyond the standard framework of GR. These theories address a number of observed and theoretical inconsistencies. By combining primordial inflation and cosmic acceleration, modified gravity offers a promising solution. It could also help reconcile gravity with quantum mechanics and the electromagnetic, weak nuclear and strong nuclear interactions as well.

GR can be represented through two equivalent geometric frameworks: the teleparallel representation and the curvature representation. In the teleparallel representation, non-metricity and curvature vanish while torsion remains non-zero; conversely, in the curvature representation, torsion and non-metricity are zero, but curvature is non-zero. Another equivalent approach is the symmetric teleparallel gravity, where the basic geometry of the gravitational action is represented by the non-metricity Q of the metric, which defines the variation of the length of a vector during the parallel transport around a close loop.

1.4.1 Geometrical representation

The geometry associated with non-metricity will be explored in this section. Consider the vectors defined on a differential manifold equipped with a connection and a metric $g_{\mu\nu}$ are u^μ and v^μ . The $u \cdot v = u^\mu v^\nu g_{\mu\nu}$ is the inner product of these vectors. When parallel transporting two vectors along a curve C with the parametrization $x^\mu = x^\mu(\lambda)$, the implications of non-metricity during the transport process can be analyzed by examining the covariant derivative of the metric tensor.

$$\tilde{\nabla}_\lambda(u \cdot v) = \frac{dx^\alpha}{d\lambda} \left(\tilde{\nabla}_\alpha u^\mu \right) v_\mu + \frac{dx^\alpha}{d\lambda} \left(\tilde{\nabla}_\alpha v^\nu \right) u_\nu + \frac{dx^\alpha}{d\lambda} \left(\tilde{\nabla}_\alpha g_{\mu\nu} \right) u^\mu v^\nu . \quad (1.44)$$

The condition of parallel transport of u^μ and v^μ leads to

$$\frac{dx^\alpha}{d\lambda} \left(\tilde{\nabla}_\alpha u^\mu \right) = 0 , \quad \text{and} \quad \frac{dx^\alpha}{d\lambda} \left(\tilde{\nabla}_\alpha v^\mu \right) = 0 , \quad (1.45)$$

and hence

$$\tilde{\nabla}_\lambda(u \cdot v) = Q_{\alpha\mu\nu} \frac{dx^\alpha}{d\lambda} u^\mu v^\nu . \quad (1.46)$$

This shows that parallel transporting two vectors around a curve changes their inner product. Equalizing the two vectors gives

$$\tilde{\nabla}_\lambda(|u|^2) = Q_{\alpha\mu\nu} \frac{dx^\alpha}{d\lambda} u^\mu u^\nu . \quad (1.47)$$

The discussion highlights the variation in the magnitude of a vector during parallel transport along a specified curve. Consequently, in a space characterized by non-metricity, the length of a vector is not invariant under parallel transport.

1.4.2 Decomposition of Affine connection

In metric-affine spacetime, the connection $\Gamma^\lambda_{\sigma\rho}$ and the metric $g_{\mu\nu}$ are treated independently. This allows for more general formulations of covariant derivatives and parallel transport compared to the standard metric-compatible cases found in GR. The covariant derivative of a \mathcal{T}^λ_ν in a metric-affine spacetime is given by the expression

$$\nabla_\mu \mathcal{T}^\lambda_\nu = \partial_\mu \mathcal{T}^\lambda_\nu + \Gamma^\lambda_{\mu\alpha} \mathcal{T}^\alpha_\nu - \Gamma^\alpha_{\mu\nu} \mathcal{T}^\lambda_\alpha . \quad (1.48)$$

Here, ∇_μ denotes the covariant derivative, ∂_μ is the partial derivative. The term $\Gamma^\lambda_{\mu\alpha} \mathcal{T}^\alpha_\nu$ adjusts for the change in the tensor component \mathcal{T}^λ_ν due to the connection, while $\Gamma^\alpha_{\mu\nu} \mathcal{T}^\lambda_\alpha$ accounts for the variation in the covariant indices. As known from differential geometry (see, e.g., [96, 97]), generic affine connection can be decomposed into three parts [98],

$$\Gamma^\lambda_{\mu\nu} = \left\{ {}^\lambda_{\mu\nu} \right\} + K^\lambda_{\mu\nu} + L^\lambda_{\mu\nu} , \quad (1.49)$$

the Levi-Civita connection of the metric $g_{\mu\nu}$,

$$\left\{ {}^\lambda_{\mu\nu} \right\} \equiv \frac{1}{2} g^{\lambda\beta} (\partial_\mu g_{\beta\nu} + \partial_\nu g_{\beta\mu} - \partial_\beta g_{\mu\nu}) , \quad (1.50)$$

contortion

$$K^\lambda_{\mu\nu} \equiv \frac{1}{2} g^{\lambda\beta} (T_{\mu\beta\nu} + T_{\nu\beta\mu} + T_{\beta\mu\nu}) = -K_{\nu\mu}^\lambda , \quad (1.51)$$

and disformation

$$L^\lambda_{\mu\nu} \equiv \frac{1}{2} g^{\lambda\beta} (-Q_{\mu\beta\nu} - Q_{\nu\beta\mu} + Q_{\beta\mu\nu}) = L^\lambda_{\nu\mu} . \quad (1.52)$$

In metric-affine spacetimes, the connection $\Gamma^\lambda_{\mu\nu}$ governs various geometric properties, including torsion, non-metricity and curvature. These quantities are defined as follows:

Torsion is given by,

$$T^\lambda_{\mu\nu} \equiv \Gamma^\lambda_{\mu\nu} - \Gamma^\lambda_{\nu\mu} . \quad (1.53)$$

Torsion measures the failure of the connection to be symmetric in its lower indices.

Curvature is given by the Riemann curvature tensor

$$R^\sigma_{\rho\mu\nu} \equiv \partial_\mu \Gamma^\sigma_{\nu\rho} - \partial_\nu \Gamma^\sigma_{\mu\rho} + \Gamma^\alpha_{\nu\rho} \Gamma^\sigma_{\mu\alpha} - \Gamma^\alpha_{\mu\rho} \Gamma^\sigma_{\nu\alpha} . \quad (1.54)$$

Curvature describes how the connection fails to be locally flat.

By imposing constraints on the connection, different geometric frameworks emerge shown in Fig. 1.1. These frameworks are categorized as [99],

- **Riemann-Cartan geometry:** This geometry is obtained by assuming that the non-metricity $Q_{\rho\mu\nu}$ vanishes, but torsion $T^\lambda_{\mu\nu}$ and curvature $R^\sigma_{\rho\mu\nu}$ are generally non-zero.

- **Teleparallel geometry:** In this case, curvature $R^\sigma_{\rho\mu\nu}$ is zero, leading to parallel transport of vectors being path-independent. Torsion and non-metricity are generally non-zero.
- **Torsion-free geometry:** This geometry is characterized by a vanishing torsion $T^\lambda_{\mu\nu}$, but non-metricity and curvature are allowed to be non-zero.
- **LC connection and Riemann geometry:** By setting both torsion $T^\lambda_{\mu\nu}$ and non-metricity $Q_{\rho\mu\nu}$ to zero, the connection is simplified to the Levi-Civita connection. This connection is metric-compatible and torsion-free, which is a defining characteristic of Riemannian geometry.
- **WC:** This is characterized by vanishing non-metricity $Q_{\rho\mu\nu}$ and curvature $R^\sigma_{\rho\mu\nu}$, leading to a specific class of teleparallel geometries.
- **STG:** In this case, torsion $T^\lambda_{\mu\nu}$ and curvature $R^\sigma_{\rho\mu\nu}$ are both zero, leading to symmetric teleparallel geometry.
- **Minkowski Space:** This is the case where torsion $T^\lambda_{\mu\nu}$, non-metricity $Q_{\rho\mu\nu}$ and curvature $R^\sigma_{\rho\mu\nu}$ are all zero, representing flat spacetime.

To denote specific situations based on these properties, the labeled notation are used, such as $\overset{\text{STG}}{\Gamma}{}^\lambda_{\mu\nu}$ for a geometry with generalized symmetric teleparallel properties, $\overset{\text{WC}}{\nabla}_\mu$ for a geometry with the Weitzenböck connection and $\overset{\text{LC}}{R}{}^\sigma_{\rho\mu\nu}$ for the Riemann curvature tensor in Levi-Civita connection. The best approach to relax Riemannian constraints is now clear from the discussion above. Specifically, to explore non-Riemannian geometry, a generic affine connection that accommodates both torsion and non-metricity is needed. This type of connection naturally incorporates the degrees of freedom associated with torsion and non-metricity. Let us discuss more about non-metricity teleparallel theory.

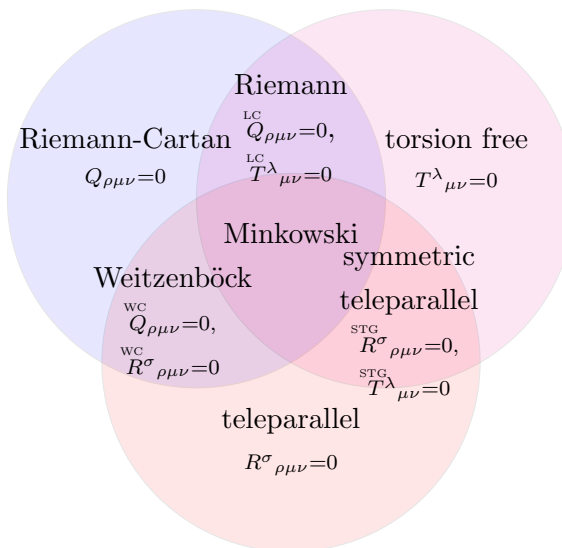


FIGURE 1.1: Depending on the properties of connection, the subclasses of metric-affine geometry.
 [Credit: Phys. Rev. D. 97, 124025 (2018)]

1.4.3 Symmetric teleparallel equivalent to GR

In the presence of a metric $g_{\mu\nu}$, not only the curvature and torsion can be defined, but also the non-metricity. The most general even-parity second order quadratic form of the non-metricity is [100]

$$Q = \frac{1}{4}Q_{\alpha\beta\gamma}Q^{\alpha\beta\gamma} - \frac{1}{2}Q_{\alpha\beta\gamma}Q^{\beta\alpha\gamma} - \frac{1}{4}Q_{\alpha}Q^{\alpha} + \frac{1}{2}Q_{\alpha}\tilde{Q}^{\alpha}. \quad (1.55)$$

The general quadratic action incorporating appropriate Lagrange multipliers is then

$$S_Q = \int d^4x \left[\frac{1}{16\pi G} \sqrt{-g} Q + \lambda_{\alpha}^{\beta\mu\nu} R^{\alpha}_{\beta\mu\nu} + \lambda_{\alpha}^{\mu\nu} T^{\alpha}_{\mu\nu} \right]. \quad (1.56)$$

Here, Eq. (1.56) have a 5-parameter family of quadratic theories. The next step is to explore this space of theories and identify if any specific case can reproduce an equivalent of GR. However, the existence of an equivalent to GR for a torsion-free connection can be demonstrated again, which leads to

$$R(\Gamma) = \mathcal{R}(g) + Q + \nabla_{\alpha}(Q^{\alpha} - \tilde{Q}^{\alpha}). \quad (1.57)$$

The second postulate of STEGR asserts that the curvature of the affine connection vanishes (i.e. $R(\Gamma) = 0$) implies that the relation $\mathcal{R}(g) = -Q - \nabla_{\alpha}(Q^{\alpha} - \tilde{Q}^{\alpha})$ and consequently, the action

$$\mathcal{S}_{\text{STEGR}} = \frac{1}{16\pi G} \int d^4x \sqrt{-g} Q. \quad (1.58)$$

According to the generalized Gauss theorem, the term $\nabla_{\alpha}(Q^{\alpha} - \tilde{Q}^{\alpha})$ is discarded, as a term amounts to a mere boundary term which can thus have no influence on the field equations [101]. The STEGR [102], is characterized by its distinction from the Hilbert action, which differs solely by a total derivative. This property ensures that the dynamics of STEGR align with those of GR. Notably, in the TEGR framework, the quadratic form Q exhibits a unique symmetry realized up to a total derivative.

The difference between the invariant Q and the Ricci scalar is simply a boundary term. The framework defined by Q , which excludes this boundary contribution, represents a specific class of special STG models, analogous to an enhanced version of GR.

1.4.4 $f(Q)$ extension

The general $f(Q)$ gravity can be achieved by extending STEGR through the incorporation of an action defined by an arbitrary $f(Q)$ function as

$$S = \int d^4x \sqrt{-g} \left[\frac{1}{2\kappa} f(Q) + L_m \right]. \quad (1.59)$$

A particular choice of non-metricity scalar and the associated action results in the recovery of General Relativity when $f(Q) = Q$. Varying action (1.59) with respect to $g_{\mu\nu}$ yields the field

equation [85]

$$\frac{2}{\sqrt{-g}} \nabla_\alpha (\sqrt{-g} f_Q P^\alpha_{\mu\nu}) + \frac{1}{2} g_{\mu\nu} f + f_Q \left(P_{\mu\alpha\beta} Q_\nu^{\alpha\beta} - 2 Q_{\alpha\beta\mu} P^{\alpha\beta}_{\nu} \right) = \kappa T_{\mu\nu} . \quad (1.60)$$

Recently, the covariant formulation to this field equation has been developed and successfully applied to study geodesic deviations and various phenomena within the cosmological context [103]. So Eq. (1.60) can be rewritten as

$$f_Q \overset{\circ}{G}_{\mu\nu} + \frac{1}{2} g_{\mu\nu} (Q f_Q - f) + 2 f_{QQ} P^\lambda_{\mu\nu} \overset{\circ}{\nabla}_\lambda Q = \kappa T_{\mu\nu} , \quad (1.61)$$

where, $\overset{\circ}{G}_{\mu\nu} = R_{\mu\nu} - \frac{1}{2} g_{\mu\nu} R$, with R and $R_{\mu\nu}$ are the Riemannian Ricci scalar and tensor respectively and f_Q is derivative of f with respect to Q . Varying the action with respect to the connection leads to

$$\nabla_\mu \nabla_\nu (\sqrt{-g} f_Q P^\lambda_{\mu\nu} + H^\lambda_{\mu\nu}) = 0 , \quad (1.62)$$

where $H^\lambda_{\mu\nu} = -\frac{1}{2} \frac{\delta(\sqrt{-g} \mathcal{L}_m)}{\delta \Gamma^\lambda_{\mu\nu}}$ denotes the hyper momentum tensor density. Furthermore, the additional restriction over the connection may deducted, $\nabla_\mu \nabla_\nu (H^\lambda_{\mu\nu}) = 0$. As follows from Eq. (1.62)

$$\nabla_\mu \nabla_\nu (\sqrt{-g} f_Q P^\lambda_{\mu\nu}) = 0 . \quad (1.63)$$

While considering the variation of action with respect to connection, there are two ways to incorporate symmetric teleparallelism. The first approach involves the use of inertial variation [104], where the connection is set in its pure-gauge form within the action. The second approach involves the consideration of a general connection in the action, but with the introduction of Lagrange multipliers to compensate for curvature and torsion [98].

1.4.4.1 Coincident gauge

The flatness condition imposes that the connection remains purely inertial, which allows it to be expressed in terms of a general element Λ^α_β from $GL(4, \mathbb{R})$. This formulation, combined with the absence of torsion, results in the additional constraint $\partial_{[\mu} \Lambda^\alpha_{\nu]} = 0$. Consequently, the general element from $GL(4, \mathbb{R})$ that governs the connection can be parameterized by a set of functions ξ^λ as,

$$\Gamma^\alpha_{\mu\nu} = \frac{\partial x^\alpha}{\partial \xi^\lambda} \partial_\mu \partial_\nu \xi^\lambda . \quad (1.64)$$

The term $\frac{\partial x^\alpha}{\partial \xi^\lambda}$ is interpreted as the inverse of the Jacobian matrix $\frac{\partial \xi^\lambda}{\partial x^\alpha}$. This assertion indicates that within any coordinate system $\{x^0, x^1, x^2, x^3\}$, A four independent functions $\{\xi^0, \xi^1, \xi^2, \xi^3\}$ for which the Jacobian matrix $\frac{\partial \xi^\mu}{\partial x^\nu}$ is invertible can be selected, characterized by a non-zero determinant. This configurational freedom permits the construction of a flat and torsionless connection as expressed in Eq. (1.64). It is important to note that the construction of such connections is not unique; a whole family of connections is permissible under this framework.

While this freedom to choose a connection holds no significant consequence in STEGR, it does bear substantial implications in modified theories like $f(Q)$ gravity.

Moreover, Eq. (1.64) illustrates an intriguing attribute of flat and torsionless connections: they can be globally set to zero through an appropriate coordinate choice. Specifically, for any given flat and torsionless connection, it invariably conforms to the form outlined in Eq. (1.64) with certain functions ξ^μ . Thus, by selecting coordinates such that $x^\mu = \xi^\mu$, a scenario where the connection is identically zero can be achieved, as $\partial_\mu \partial_\nu \xi^\lambda = 0$. This scenario is referred to as the coincident gauge. In this context, the covariant derivative ∇_α simplifies to the partial derivative ∂_α , meaning that $Q_{\alpha\mu\nu} = \partial_\alpha g_{\mu\nu}$. This indicates that the Levi-Civita connection can be expressed in terms of the disformation tensor with the relationship $\{\lambda_{\mu\nu}\} = -L^\alpha_{\mu\nu}$.

Notably, excluding the boundary terms, this formulation specifically leads to the Einstein-Hilbert action for GR. A key advantage of this approach is its reliance solely on first derivatives of the metric, which ensures a well-posed variational principle that circumvents the need for Gibbons-Hawking-York boundary terms [105]. Despite the implementation of diffeomorphism invariance, this principle is realised only up to a total derivative, leading to an action that is contingent on the choice of coordinates. It might seem surprising that the diffeomorphisms while using them to define the coincident gauge, but there are no inconsistencies in doing so. This is because, just like the TEGR is special due to its unique symmetry, the theory being discussed is also special among quadratic formulations because it has a stronger four-parameter gauge symmetry. Consequently, the complete framework actually possesses an eight-parameter gauge symmetry. In the coincident gauge, an additional symmetry appears as a diffeomorphism symmetry. Unlike in TEGR, where the metric and connection are interrelated, the non-metricity formulation of GR treats the connection as fundamentally a pure gauge. As a result, all dynamics are described by the metric, which operates in a trivially connected spacetime. It is important to note that the fields ξ^α that parameterize the connection play a role akin to Stückelberg fields associated with invariance under coordinate transformations. In this context, the coincident gauge can be viewed as the corresponding unitary gauge.

To derive the generalized Friedmann equations, start with a flat FLRW metric (i.e. $\kappa = 0$). The most commonly used matter component considered in this framework is a perfect cosmic fluid, characterized by its stress-energy-momentum tensor (1.28). Incorporating the equation presented in (1.60) yields the corresponding set of equations as,

$$Qf_Q - \frac{f}{2} = \rho, \quad (1.65)$$

$$f_Q \dot{H} + \dot{f}_Q H = -\frac{1}{2}(\rho + p). \quad (1.66)$$

It is worth noting that the standard Friedmann equations of GR can be obtained if $f(Q) = Q$ is substituted. Some of the relevant studies can be seen in Refs. [86, 88, 89, 106–111] within the framework of coincident gauge.

1.4.4.2 Non-coincident gauge

In the context of gravitational theories, adopting a non-coincident gauge, where $\Gamma_{\mu\nu}^\alpha \neq 0$, indicates the selection of a coordinate system that diverges from the standard Riemannian structure found in GR. This choice can significantly influence the formulation of the gravitational field equations and the definition of various physical quantities. The non-metricity tensor is crucial for capturing the effects of non-metricity on gravitational dynamics. By using a non-coincident gauge, researchers can explore the implications of these modifications in detail. This approach can lead to different physical interpretations and solutions compared to conventional GR, particularly in terms of how the gravitational field interacts with matter.

These connections can be classified into three types, based on K_1 , K_2 and K_3 given by [112],

$$\begin{aligned}\Gamma_{tt}^t &= K_1, \quad \Gamma_{rr}^t = K_2, \quad \Gamma_{\theta\theta}^t = K_2 r^2, \\ \Gamma_{tr}^r &= \Gamma_{rt}^r = \Gamma_{t\theta}^\theta = \Gamma_{\theta t}^\theta = \Gamma_{t\phi}^\phi = \Gamma_{\phi t}^\phi = K_3, \\ \Gamma_{r\theta}^\theta &= \Gamma_{\theta r}^\theta = \Gamma_{r\phi}^\phi = \Gamma_{\phi r}^\phi = \frac{1}{r}, \quad \Gamma_{\theta\theta}^r = -r, \\ \Gamma_{\phi\phi}^r &= -r \sin^2 \theta, \quad \Gamma_{\phi\phi}^t = K_2 r^2 \sin^2 \theta, \\ \Gamma_{\theta\phi}^\phi &= \Gamma_{\phi\theta}^\phi = \cot \theta, \quad \Gamma_{\phi\phi}^\theta = -\cos \theta \sin \theta.\end{aligned}\tag{1.67}$$

Using the definition of non-metricity scalar, Eqs. (1.8) and (1.67), the non-metricity scalar can be obtained as,

$$Q = -6H^2 + 9HK_3 + 3K_3(K_1 - K_3) + \frac{3K_2H}{a^2} - \frac{3K_2(K_1 + K_3)}{a^2}.\tag{1.68}$$

Meanwhile this connection should satisfy the curvature-free condition and this gives the constraints about three free parameters K_1 , K_2 and K_3

$$\begin{aligned}K_3(K_1 - K_3) - \dot{K}_3 &= 0, \\ K_2(K_1 - K_3) + \dot{K}_2 &= 0, \\ \kappa + K_2K_3 &= 0.\end{aligned}$$

Consider three different connections for $\kappa = 0$, each defined as,

- Connection I: $K_1 = \gamma(t)$, $K_2 = K_3 = 0$;
- Connection II: $K_1 = \gamma(t) + \frac{\dot{\gamma}(t)}{\gamma(t)}$, $K_2 = 0$, $K_3 = \gamma(t)$;
- Connection III: $K_1 = -\frac{\dot{\gamma}(t)}{\gamma(t)}$, $K_2 = \gamma(t)$, $K_3 = 0$,

where γ is the non-vanishing function of t . For each connection, the resulting field equations are different. The non-metricity scalar Q and Friedmann equations for each connection are

For Connection I:

$$Q = -6H^2 , \quad (1.69)$$

$$3H^2 f_Q + \frac{1}{2}(f - Qf_Q) = \rho , \quad (1.70)$$

$$-2\frac{d(f_Q H)}{dt} - 3H^2 f_Q - \frac{1}{2}(f - Qf_Q) = p . \quad (1.71)$$

For Connection II:

$$Q = -6H^2 + 9\gamma H + 3\dot{\gamma} , \quad (1.72)$$

$$3H^2 f_Q + \frac{1}{2}(f - Qf_Q) + \frac{3\gamma}{2}\dot{Q}f_{QQ} = \rho , \quad (1.73)$$

$$-2\frac{d(f_Q H)}{dt} - 3H^2 f_Q - \frac{1}{2}(f - Qf_Q) + \frac{3\gamma}{2}\dot{Q}f_{QQ} = p . \quad (1.74)$$

For Connection III:

$$Q = -6H^2 + \frac{3\gamma H}{a^2} + \frac{3\dot{\gamma}}{a^2} , \quad (1.75)$$

$$3H^2 f_Q + \frac{1}{2}(f - Qf_Q) - \frac{3\gamma}{2a^2}\dot{Q}f_{QQ} = \rho , \quad (1.76)$$

$$-2\frac{d(f_Q H)}{dt} - 3H^2 f_Q - \frac{1}{2}(f - Qf_Q) + \frac{\gamma}{2a^2}\dot{Q}f_{QQ} = p , \quad (1.77)$$

where ρ denotes the energy density, including baryonic matter, cold dark matter and radiation and p represents the pressure. In the case of connection I, the non-metricity scalar Q and the Friedmann equations (1.69) - (1.71) are independent of the function γ , aligning with the results obtained under the coincident gauge where $\Gamma^\lambda_{\mu\nu} = 0$ in the flat FLRW metric.

1.5 Basics of Statistics

This section will focus on fundamental statistical techniques crucial for cosmological reconstruction. The best-fit values for the parameters can be derived through two main approaches: by minimizing a specific objective function utilizing optimization methods or by maximizing the likelihood function through marginalization. Another method involves using MCMC analysis, which efficiently marginalizes the posterior probability distribution across the parameter space to obtain constraints on the parameters of interest.

1.5.1 χ^2 model fitting

The χ^2 statistic is a widely used tool in statistical analysis, particularly for assessing the goodness of fit of a model to observational data. It quantifies the deviation between observed data and the corresponding theoretical predictions, considering the uncertainties in the measurements. This approach is commonly applied in various fields such as physics, astronomy and economics, where data is often subject to measurement errors and uncertainties.

Let $\{f_i\}$ represent the set of measured values at data points indexed by i and $\{f_{i,\text{obs}}\}$ denote the corresponding observed data points. The corresponding theoretical predictions, $f_{i,\text{th}}(\{\theta\})$, depend on a set of model parameters $\{\theta\}$. The standard deviation or uncertainty of each measurement is represented by σ_i .

The χ^2 is defined as,

$$\chi^2 = \sum_i \frac{[f_{i,\text{obs}} - f_{i,\text{th}}(\{\theta\})]^2}{\sigma_i^2} . \quad (1.78)$$

This expression compares the difference between the observed and theoretical values, weighting the discrepancies by the inverse of the variance (i.e., the square of the standard deviation). This allows more reliable measurements to contribute more significantly to the overall statistic.

Moreover, in many experimental setups, the data points are not independent but may exhibit correlation due to various factors such as measurement conditions or systematic errors. In such cases, the uncertainty in the measurements is not simply described by individual σ_i 's but rather by a covariance matrix Cov_{ij} , which represents the correlation between different data points. Then the generalized form of the χ^2 is give by

$$\chi^2 = \sum_{i,j} \left[f_{i,\text{obs}} - f_{i,\text{th}}(\{\theta\}) \right]^T \left(\text{Cov}_{ij} \right)^{-1} \left[f_{j,\text{obs}} - f_{j,\text{th}}(\{\theta\}) \right] , \quad (1.79)$$

where symbol T as a superscript represents the transpose of a matrix. The combined χ^2_{tot} for statistical analysis with a combination of n datasets is defined by adding up the χ^2 associated with individual datasets.

$$\chi^2_{\text{tot}} = \sum_m \chi^2_m , \quad (1.80)$$

where n represents the datasets considered for that specific combination. This form of the χ^2 statistic is necessary when dealing with correlated errors, as it properly adjusts for the dependencies between the measurements, ensuring that the covariance structure of the data is incorporated into the analysis.

To determine the optimal set of model parameters $\{\theta\}$, the goal is to minimize the χ^2 function. The set of parameters $\{\theta_{\text{best}}\}$ that minimizes χ^2 provides the best fit to the observed data. To assess the quality of the fit, it is useful to consider the χ^2_{red} , which normalizes χ^2 by the number

of degrees of freedom d . The reduced χ^2 is given by

$$\chi_{red}^2 = \frac{\chi^2}{d} , \quad d = N - k .$$

N : The number of data points, k : The number of parameters in the model (1.81)

The value of χ_{red}^2 provides an indication of the goodness of fit.

- If $\chi_{red}^2 = 1$, the model is considered to be a good fit to the data, with the observed deviations being consistent with the experimental uncertainties.
- If $\chi_{red}^2 > 1$, the model does not fit the data well and it suggests that the uncertainties might have been overestimated or the model is inappropriate.
- If $\chi_{red}^2 < 1$, it suggests over-fitting, where the model fits the data too perfectly, possibly due to the inclusion of too many parameters or underestimation of the uncertainties.

Additionally, the difference between the minimized χ^2 and χ_{min}^2 at a given set of parameter values, $\Delta\chi^2 = \chi^2 - \chi_{min}^2$, can be used to determine the confidence intervals for a specific mode at the 1σ (68%) and 2σ (95%) levels.

In the context of MCMC, χ^2 minimization plays a key role in efficiently exploring the parameter space. The MCMC algorithm generates a sequence of parameter sets, forming a Markov chain, which ultimately converges to the distribution of parameters that minimize the χ^2 function. This process enables a thorough exploration of the parameter space, accounting for uncertainties and correlations between parameters. By minimizing χ^2 , MCMC analysis yields robust parameter estimates and provides valuable insights into how well the model fits the data. This method is widely used in diverse fields such as cosmology, particle physics and statistical modeling, as it can handle complex models and large datasets effectively.

1.5.2 Maximum likelihood analysis

Bayesian inference is a statistical approach that provides a framework for updating the probability distribution of model parameters in light of new data. It is based on Bayes' theorem, which relates the posterior probability of parameters $\{\theta\}$ to the prior probability and the likelihood of the observed data \mathcal{D} . With prior information I , the posterior probability distribution is given by,

$$P(\{\theta\}|\mathcal{D}, I) = \frac{P(\{\theta\}|I)P(\mathcal{D}|\{\theta\}, I)}{P(\mathcal{D}|I)} , \quad (1.82)$$

where, $P(\mathcal{D}/\{\theta\}, I)$ denotes the probability of obtaining the data \mathcal{D} given the parameters $\{\theta\}$ with respect to I , also referred to as the likelihood \mathcal{L} and $P(\{\theta\}/I)$ represents the prior probabilities. Additionally, the global likelihood serving as a normalization factor is denoted and

given by,

$$P(\mathcal{D}/I) = \int_{\theta_1} \dots \int_{\theta_n} P(\{\theta\}|I) P(\mathcal{D}|\{\theta\}, I) d\theta_1 \dots d\theta_n, \quad (1.83)$$

such that

$$\int_{\theta_1} \dots \int_{\theta_n} P(\{\theta\}|\mathcal{D}, I) d\theta_1 \dots d\theta_n = 1. \quad (1.84)$$

To evaluate the goodness of fit between the model and the data, the likelihood function $P(\mathcal{D}/\{\theta\}, I)$ is often related to the χ^2 function, which is commonly used in many practical applications. The likelihood can be expressed in terms of the χ^2 statistic as

$$\mathcal{L}(\{\theta\}) = \exp\left(-\frac{\chi^2}{2}\right). \quad (1.85)$$

Therefore, it can be observed that the maximized value of the likelihood function \mathcal{L} corresponds to minimized value of χ^2 .

To estimate the posterior distribution of the parameters $\{\theta\}$, MCMC analysis is used, which allow for efficient sampling of the parameter space. The goal is to approximate the posterior distribution $P(\{\theta\}|\mathcal{D}, I)$ by utilizing the sampled sets and to generate a sequence of parameter sets $\{\theta\}$. One of the most widely used MCMC algorithms is the Metropolis-Hastings algorithm. The Metropolis-Hastings algorithm works by proposing a new set of parameters $\{\theta^{new}\}$ based on the current set $\{\theta\}$ and then evaluates the likelihood ratio between the new and current sets of parameters and decides whether to accept or reject the proposed set according to this ratio. Specifically, the acceptance probability is given by,

$$A = \min\left(1, \frac{P(\mathcal{D}|\{\theta^{new}\}, I)}{P(\mathcal{D}|\{\theta\}, I)}\right), \quad (1.86)$$

where $P(\mathcal{D}|\{\theta\}, I)$ and $P(\mathcal{D}|\{\theta^{new}\}, I)$ are the likelihoods of the current and proposed parameter sets, respectively. If the proposed set is accepted, it becomes the next state in the chain; otherwise, the chain stays at the current set. Over time, the MCMC chain will explore the parameter space, with the probability of being in any given region of the space proportional to the likelihood of that region. This enables the chain to converge to the posterior distribution. The algorithm will tend to spend more time in regions of high likelihood, allowing for an efficient search for the best-fitting parameter values. Once the MCMC chain has run for a sufficient number of iterations and reached equilibrium, the samples from the chain to estimate the posterior distribution of the parameters can be utilized. From the MCMC samples, the marginalized posterior distributions for each parameter by integrating over the other parameters can be computed. These marginal distributions provide the parameter values along with their uncertainties. Therefore, the MCMC analysis resembles χ^2 minimization, but it marginalizes the parameters instead of optimizing them.

Foreman-Mackey et al. [113] developed the ensemble sampler for MCMC in Python, emcee ². As part of our analysis, a two-dimensional confidence contours using the Python module GetDist

²<https://github.com/dfm/emcee>

³ are visualized, developed by Lewis [114]. The Python gallery ChainConsumer ⁴ to visualize these contours are used.

1.6 Observational Datasets

Cosmological observations have played a crucial role in understanding the expansion history and dynamics of the Universe. This discussion provides a brief overview of significant cosmological discoveries that enhance our understanding of cosmic evolution.

1.6.1 Hubble measurements

The Hubble dataset provides valuable insights into the detailed history of the expansion of the Universe. Direct measurements of $H(z)$ at various redshifts serve as a key cosmological data, which are obtained from the ages of the most massive and passively evolving galaxies. These Hubble measurements are derived using two primary techniques: the galaxy differential age method (often referred to as the CC method) and radial BAO size method [115].

Reference [116, 117] have presented 13 $H(z)$ values derived from the BC03 and MaStro stellar population synthesis models [118], which are included in the CCB and CCM compilations, respectively. Furthermore, [119, 120] have provided 5 $H(z)$ measurements using the BC03 model, which have been integrated into the CCB compilation. The combined MaStro/BC03 $H(z)$ values, totaling 2 measurements, are presented in [121]. In addition, [122] introduced an alternative SPS model, distinct from both MaStro and BC03, providing 11 $H(z)$ measurements known as the CCH compilation, along with 26 points derived from the BAO method [123]. Our analysis incorporates a total of 32 $H(z)$ measurements spanning a redshift range of $0.07 \leq z \leq 1.965$ [124].

1.6.2 Type Ia Supernovae

When a white dwarf star explodes after reaching the Chandrasekhar mass limit, typically by accreting mass from a companion star then a SNe Ia occurs. These events are crucial as standard candles for measuring cosmic distances due to their predictable luminosity. In 1998, Riess et al. [19] used observations of 16 distant and 34 nearby SNe Ia from the Hubble Space Telescope to discover the accelerated expansion of the Universe. This finding was confirmed in 1999 by Perlmutter et al. [22], who analyzed 18 nearby supernovae from the Calan-Tololo survey and 42 high-redshift SNe Ia. Since then, numerous surveys have contributed to the study of SNe Ia, including the Sloan Digital Sky Survey (SDSS) Supernova Survey [125, 126], the Lick Observatory Supernova Search (LOSS) [127, 128], the Nearby Supernova Factory (NSF)

³<https://github.com/cmbant/getdist>

⁴<https://github.com/Samreay/ChainConsumer>

[129, 130], the Supernova Legacy Survey (SNLS) [131, 132] and the Higher-Z Team [133, 134]. More recently, the Union 2.1 dataset, containing 580 SNe Ia, was released [135].

The Pantheon⁺ (PN⁺ & SH0ES) analysis [136] is an updated version of the original Pantheon study. The primary distinction between the two lies in the inclusion of additional data in the Pantheon⁺ compilation. While the original Pantheon analysis utilized a sample of 1048 SNe Ia to investigate the expansion history of the Universe, the Pantheon⁺ analysis incorporates an even larger sample of 1701 SNe Ia, providing a more extensive dataset for cosmological studies. The term “PN⁺ & SH0ES” as referred to in the Pantheon⁺ analysis in Ref. [137], incorporates the SH0ES Cepheid host distance anchors ([138]) in the likelihood which helps to break the degeneracy between the parameter when analyzing SNe Ia alone. This comprehensive dataset includes distance moduli derived from 1701 light curves of 1550 spectroscopically confirmed SNe Ia, gathered from 18 distinct surveys. The Pantheon⁺ analysis encompasses a broader redshift range of $0.00122 < z < 2.2613$, in contrast to the original Pantheon dataset, which is limited to redshifts above $z < 0.01$. This expanded range allows for a more thorough evaluation of systematic uncertainties, resulting in better-constrained parameters.

1.6.3 Baryon acoustic oscillations

BAO refer to the periodic density fluctuations in baryonic matter created by sound waves propagating through the early Universe [139, 140]. Like SNe Ia, BAO serves as a standard ruler in cosmology, providing a means to study the expansion history of the Universe. The imprint of BAO on the matter power spectrum can be detected through galaxy cluster surveys at low redshifts ($z < 1$) [141]. Additionally, BAO signatures can be observed in reionization-era emissions, offering valuable information about the early Universe at higher redshifts ($1.5 \leq z \leq 2.0$) [142].

By analyzing the apparent magnitude of BAO in astronomical data, one can calculate the Hubble parameter and angular diameter distance, providing key cosmological insights. Numerous surveys, including the Two-degree-Field Galaxy Redshift Survey (2dFGRS) [143] and the SDSS [144, 145], have focused on BAO measurements. Among these, SDSS has been especially successful, with regular data releases, including the eighth one (SDSS DR8) in 2011.⁵

Recent observational efforts, such as the Dark Energy Spectroscopic Instrument (DESI) surveys [146], SNe Ia [19, 22], the Wilkinson Microwave Anisotropy Probe [147], the CMB [148] and the Baryon Oscillation Spectroscopic Survey (BOSS) [149], have prompted further exploration into potential modifications and extensions to GR. These datasets are central to ongoing efforts to refine our understanding of cosmic acceleration and to explore alternatives to the standard cosmological model.

⁵ www.sdss3.org/dr8/

1.7 Stability Analysis

A dynamical system can be understood as any system that evolves over time or through iterations, described by a space (phase space) and a mathematical rule that governs its evolution. In this context, the phase space is a collection of variables that describe the state of the system and the mathematical rule (often in the form of differential equations or iterated maps) determines how the state changes over time. This abstract formulation applies to systems ranging from simple mechanical systems like a pendulum to complex phenomena such as the behavior of the human brain or the entire Universe.

There are two primary categories of dynamical system based on how time is treated: continuous and discrete. Continuous dynamical systems are governed by Ordinary Differential Equation, which describe how the state of the system changes continuously with respect to an independent variable. On the other hand, discrete dynamical systems are governed by iterated maps or difference equations, where the state evolves in discrete steps rather than continuously. For the purpose of this discussion is to focus on continuous systems, particularly in fields like cosmology, where the evolution of the Universe is described by the Einstein field equations - a set of ODE.

Consider an n -dimensional phase space, $X \subset \mathbb{R}^n$, where each point in this space represents the state of the system. The state is described by a vector of variables (x_1, x_2, \dots, x_n) , which represent positions or other physical quantities depending on the system being modeled. The time evolution of these variables is governed by a set of ODE [150],

$$\dot{x}_i = f_i(x_1, \dots, x_n), \quad i = 1, \dots, n \quad (1.87)$$

where $f_i : X \rightarrow X$ are smooth functions defining how each state variable x_i changes over time. The system is said to be autonomous if the equations do not explicitly depend on the independent variable t . In a more compact form, this system can be expressed as a vector field $f(x)$ on \mathbb{R}^n as,

$$\dot{x} = f(x) . \quad (1.88)$$

Here, $\dot{x} = (\dot{x}_1, \dot{x}_2, \dots, \dot{x}_n)$ is the derivative of the state vector $x = (x_1, x_2, \dots, x_n)$ with respect to time and $f(x) = (f_1(x), f_2(x), \dots, f_n(x))$.

The evolution of the system can be visualized in the phase space, where each point represents a possible state of the system and its trajectory is determined by the initial conditions. A solution to the system of ODE with an initial condition $x(0) = x_0$ traces a curve (trajectory or orbit) in phase space. This curve represents the evolution of the system over time, starting from the initial state x_0 . The behavior of the system can be studied by observing the flow of trajectories in phase space.

An important aspect of dynamical systems is the concept of critical points (or fixed points), which are points in phase space where the derivatives of all state variables are zero (i.e. $f(x_0) = 0$) [151]. These critical points can represent equilibrium states of the system. The stability of

these points is crucial for understanding the long-term behavior of the system. A critical point is stable (or Lyapunov stable) if solutions that start close to it remain close over time. It is asymptotically stable if solutions not only remain close but also converge to the critical point. On the other hand, an unstable critical point causes nearby solutions to move away from it. The nature of stability can be analyzed through linearization, where the system is approximated by a linear model near the critical point, providing insights into the behavior of solutions in its neighborhood.

Through the study of these concepts, dynamical systems offer powerful tools for understanding a wide range of physical, biological and cosmological phenomena from simple mechanical systems to the complex evolution of the Universe itself. Analyzing the trajectories in phase space and the stability of critical points provide insights into the behavior of the system, allows prediction of future states and helps understand the underlying principles governing its evolution.

1.7.1 Linear stability theory

To linearize the system near a critical point, a Taylor expansion of $f(x)$ around x_0 is used. Since $f(x_0) = 0$ by definition of a critical point, the system to the first order expanded as

$$f(x) \approx J(x_0)(x - x_0) , \quad (1.89)$$

where $J(x_0)$ is the Jacobian matrix of the system evaluated at x_0 and $x - x_0$ represents small perturbations from the critical point. Thus, the linearized system becomes

$$\dot{x} = J(x_0)(x - x_0) . \quad (1.90)$$

This approximation holds when the deviations from x_0 are small and the system behaves in a linear manner around the critical point. The evolution of the state near x_0 is now governed by the Jacobian matrix, which encodes the local behavior of the system.

The Jacobian matrix $J(x_0)$ is a matrix of partial derivatives representing how the components of the vector field $f(x)$ change with respect to each state variable at the critical point x_0 as

$$J(x_0) = \begin{pmatrix} \frac{\partial f_1}{\partial x_1} & \dots & \frac{\partial f_1}{\partial x_n} \\ \vdots & \ddots & \vdots \\ \frac{\partial f_n}{\partial x_1} & \dots & \frac{\partial f_n}{\partial x_n} \end{pmatrix}_{x=x_0} . \quad (1.91)$$

The matrix $J(x_0)$ is crucial for determining the nature of the critical point. To understand the stability of x_0 , the eigenvalues of the Jacobian matrix are examined. The eigenvalues give insight into how small perturbations evolve over time. The stability of a critical point x_0 depends on the eigenvalues of $J(x_0)$. The classification of fixed points as,

- **Hyperbolic point :** A point is considered hyperbolic if all eigenvalues of the Jacobian matrix have non-zero real parts. In this case, the linearized system adequately describes

the stability of the critical point and the analysis using the Jacobian matrix suffices to determine whether the point is an attractor, repeller or saddle [150–152].

- *Stable point (Attractor)* - If all the eigenvalues of $J(x_0)$ have negative real parts, the trajectories near x_0 will converge to x_0 indicating that x_0 is a stable attractor. This is the case for stable nodes.
- *Unstable point (Repeller)* - If all the eigenvalues have positive real parts, trajectories will diverge from x_0 making it an unstable point or repeller. The system tends to move away from x_0 , as seen in unstable nodes.
- *Saddle point* - If the eigenvalues of $J(x_0)$ have mixed signs, the point is a saddle. Trajectories will be attracted to x_0 along the directions associated with negative real parts but repelled along directions with positive real parts.
- *Spiral* - In systems with complex eigenvalues (when the real part is non-zero and the imaginary part is also present), the fixed point may behave as a spiral. The direction of the spiral depends on the sign of the real part of the eigenvalues. A stable spiral occurs when the real part is negative, causing the trajectories to spiral inward, while an unstable spiral occurs when the real part is positive, causing the trajectories to spiral outward.
- **Non-Hyperbolic point :** If at least one eigenvalue of the Jacobian matrix has a real part equal to zero, the system is non-hyperbolic and the standard linear stability theory is inadequate for determining the stability of the critical point. In such cases, the behavior of trajectories near the critical point can be more complicated and non-linear methods such as central manifold theory, Lyapunov methods or bifurcation analysis are often used to classify these points. Non-hyperbolic points can exhibit neutrally stable behavior or can be a center (in the case of purely imaginary eigenvalues).

This section covers the essential elements of linear stability analysis, offering a comprehensive understanding of how critical points in dynamical systems can be classified and the tools required for more advanced stability analysis when necessary.

1.7.2 Cosmological scalar perturbation

In stability analysis within the context of modified gravity, the focus is on understanding how small deviations from a homogeneous and isotropic Universe influence its overall stability and evolution. Typically, cosmological models assume a background Universe that is homogeneous and isotropic. However, real Universe is not perfectly homogeneous and small fluctuations in density and other quantities inevitably arise. These fluctuations can evolve over time, either growing or diminishing, depending on the underlying cosmological model and the perturbation.

In this context, the investigation focuses on how small perturbations in the Hubble parameter $H(t)$ and the matter density $\rho(t)$ impact the evolution of the Universe. The Hubble parameter $H(t)$,

which governs the rate of expansion of the Universe, is perturbed by a small term δ , such that $H(t) \rightarrow H(t)(1+\delta)$. Similarly, the matter density $\rho(t)$, which describes the distribution of matter in the Universe, is perturbed by a small deviation δ_m by $\rho(t) \rightarrow \rho(t)(1+\delta_m)$. The perturbations δ and δ_m are assumed to be small in magnitude, representing first-order perturbations from the homogeneous background. These perturbations can be thought of as small fluctuations in the Hubble parameter and the matter density around their background. By analyzing these perturbations, the stability of the cosmological model in the presence of small fluctuations can be assessed. Specifically, the goal is to determine whether these perturbations will grow or decay over time, which provides important information about the late-time behavior of the Universe. If the perturbations grow uncontrollably, the model may indicate an unstable or unrealistic cosmological evolution. Conversely, if the perturbations diminish, the system is considered stable and the Universe will tend to return to its homogeneous state.

In modified gravity theories, the presence of such small fluctuations is crucial. Modified gravity can lead to a very different evolution of perturbations compared to standard GR, depending on its specific form. Modified gravity theories, for instance, may predict that perturbations in the Hubble parameter or the matter density will behave in a manner inconsistent with observations [66, 153, 154]. Therefore, investigating the stability of these perturbations is not only important for understanding the behavior of the Universe in modified gravity but also for ensuring that these theories are consistent with current observational data. If perturbations in the Hubble parameter or matter density behave in a way that aligns with observations, it would lend support to the validity of the modified gravity theory. Conversely, if these perturbations grow too large or evolve in an unphysical manner, it may indicate that the theory needs to be adjusted or abandoned.

Overall, the stability analysis of small perturbations provides a powerful tool to test the robustness of cosmological models, especially in modified gravity frameworks and ensures that they align with the observable Universe. By systematically examining how small deviations evolve, one can gain insights into the dynamical behavior of the Universe and assess whether these deviations are consistent with a stable and observable cosmological evolution.

The subsequent chapters apply the symmetric teleparallel gravity or $f(Q)$ gravity theory previously discussed to address specific challenges mentioned above.

Chapter 2

Accelerating cosmological models in $f(Q)$ gravity and the phase space analysis

* The work, in this chapter, is covered by the following publication:

S. A. Narawade, Shashank P. Singh and B. Mishra, “Accelerating cosmological models in $f(Q)$ gravity and the phase space analysis”, *Phys. of the Dark Universe* **42** (2023) 101282.

2.1 Introduction

Before we consider the $f(Q)$ gravity as a viable alternative to GR, one of the crucial issue of $f(Q)$ gravity to be addressed, i.e. the stability of its cosmological models. One among several stability analysis is the dynamical stability analysis [155] that studies the behavior of a model under small perturbations. To be specific, it aims at to find the model coming back to the original state or evolve into a different solution. This analysis further provides an accurate prediction on the behaviour of the model pertaining to the physical scenario and thereby resulted in a robust theoretical framework. One can refer some articles on dynamical system analysis in modified theories of gravity [111, 156–161].

This chapter focuses mainly on the history of the evolution of the Universe using one of the most universally accepted methodology, namely dynamic system analysis. In this chapter, we explored the different phases of the Universe such as radiation, matter and the current accelerating phase. As part of this study, the Friedmann equations are used in framing the autonomous dynamical system. In addition, the well-motivated forms of $f(Q)$ gravity are considered as well in framing the autonomous dynamical system. In addition, we discussed the critical points in relation to the deceleration and EoS parameter. We also analyzed the phase portraits for both models in order to examine their stability. The result may provide some crucial insights into the viability of $f(Q)$ gravity and its possible contribution in understanding the structure and evolution of the Universe. This chapter is structured as, in section 2.2, the formulation of $f(Q)$ gravity with some adjustment and its corresponding field equations are introduced. Section 2.3 presents Hubble parameter for the dynamical analysis, along with two cosmological models, each with a specific form of $f(Q)$. In section 2.4, a dynamical system analysis is conducted to identify the critical points and explore their behavior. Finally, the results and conclusion are discussed in section 2.5.

2.2 Modified field equations

The field equations for $F(Q) = Q + f(Q)$ in perfect fluid from Eqs. (1.65) and (1.66) can be obtained as [162],

$$\rho = \frac{1}{2}(Q + 2Qf_Q - f), \quad (2.1)$$

$$p = \frac{1}{2}(f - Q - 2Qf_Q) - 2\dot{H}(2Qf_{QQ} + f_Q + 1). \quad (2.2)$$

We denote $f(Q) = f$ and $f_Q = \frac{\partial f}{\partial Q}$ and also we consider that the Universe is filled with dust and radiation fluids. Hence,

$$\rho = \rho_m + \rho_r, \quad p = p_r = \frac{1}{3}\rho_r,$$

with ρ_m and ρ_r represents the energy density for the matter and radiation phase respectively. Then from Eqs. (2.1) and (2.2), we get

$$3H^2 = \rho_{total} = \rho_r + \rho_m + \rho_{DE}, \quad (2.3)$$

$$2\dot{H} + 3H^2 = -p_{total} = -p_r - p_m - p_{DE}, \quad (2.4)$$

where p_m , p_r respectively denotes the pressure of matter and radiation phase; ρ_{DE} and p_{DE} be the energy density and pressure of DE phase, which can be expressed as,

$$\begin{aligned} \rho_{DE} &= \frac{f}{2} - Qf_Q, \\ p_{DE} &= 2\dot{H}(2Qf_{QQ} + f_Q) + Qf_Q - \frac{f}{2}. \end{aligned}$$

To note, the above two equations satisfies the conservation equation of the energy momentum tensor, which can be expressed as, $\dot{\rho} + 3H(\rho + p) = 0$. Now, the total EoS parameter and the EoS parameter due to DE can be obtained respectively as,

$$\omega_{total} = \frac{p_{total}}{\rho_{total}} = -1 + \frac{\Omega_m + \frac{4}{3}\Omega_r}{2Qf_{QQ} + f_Q + 1}, \quad (2.5)$$

$$\omega_{DE} = \frac{p_{DE}}{\rho_{DE}} = -1 + \frac{4\dot{H}(2Qf_{QQ} + f_Q)}{f - 2Qf_Q}. \quad (2.6)$$

The density parameter pertaining to pressure-less matter, radiation are given in (1.41) and for DE it is represented as,

$$\Omega_{DE} = \frac{\rho_{DE}}{3H^2}. \quad (2.7)$$

The EoS parameter describes the present state of the Universe. A bunch of cosmological observations recently constrained the current value of the EoS parameter to be, $\omega = -1.29^{+0.15}_{-0.12}$ [163], $\omega = -1.3$ [164], Supernovae Cosmology Project, $\omega = -1.035^{+0.055}_{-0.059}$ [165]; WAMP+CMB, $\omega = -1.079^{+0.090}_{-0.089}$ [148]; Plank 2018, $\omega = -1.03 \pm 0.03$ [166] or $\omega = -1.33^{+0.31}_{-0.42}$ [167].

These field equations provide the foundation for studying the dynamics of the Universe within the context of $f(Q)$ gravity. In the next section, we will explore Hubble parameter, deceleration parameter and jerk parameter which help us understand the cosmic evolution and along with the dynamic behaviour of the specific $f(Q)$ models.

2.3 The $f(Q)$ gravity models

To solve the above system and to analyse the behaviour of the dynamical parameters, we consider some form of Hubble parameter H and the function $f(Q)$. The Hubble parameter, $H = \xi + \frac{\eta}{t}$ corresponds to the scale factor, $a(t) = e^{\xi t}t^\eta$, known as the hybrid scale factor [168–171]. Subsequently, the non-metricity scalar becomes, $Q = 6H^2 = 6(\xi + \frac{\eta}{t})^2$. This form of Hubble parameter further provides a time varying deceleration parameter $(q = -1 + \frac{\eta}{(\xi t + \eta)^2})$, which can simulate a cosmic transition from early deceleration to late-time acceleration. The

deceleration parameter $q \approx -1 + \frac{1}{\eta}$ when $t \rightarrow 0$ and $q \approx -1$ when $t \rightarrow \infty$. To realise the positive deceleration at early Universe for the transient Universe, the scale factor parameter η should be $0 < \eta < 1$. The transition can occur at $t = -\frac{\eta}{\xi} \pm \frac{\sqrt{\eta}}{\xi}$. We will restrict to the positivity of the second term and ignore the negativity. This is because the negativity of the second term would provide negative time, which may lead to unphysical situation at the Big Bang scenario. In that case also the parameter η restricted to $0 < \eta < 1$, since the cosmic transit may have occurred at, $t = \frac{-\eta + \sqrt{\eta}}{\xi}$. The jerk parameter, $j = 1 - \frac{3\eta}{(\eta + \xi t)^2} + \frac{2\eta}{(\eta + \xi t)^3}$. We have used the parameter values for model analysis as $\xi = 0.965$ and $\eta = 0.60$ [168]. The deceleration parameter shows a transient behaviour with the transition occurs at $z = 1.34$. It reduces from early time to late-time and at present its value is, $q_0 = -0.46$ [Fig. 2.1a]. The evolution of jerk parameter remains entirely in the range $0 < j < 1$. It reduces from early time and attained the minimum value at present and eventually converges to 1 at the late-time [Fig. 2.1b].

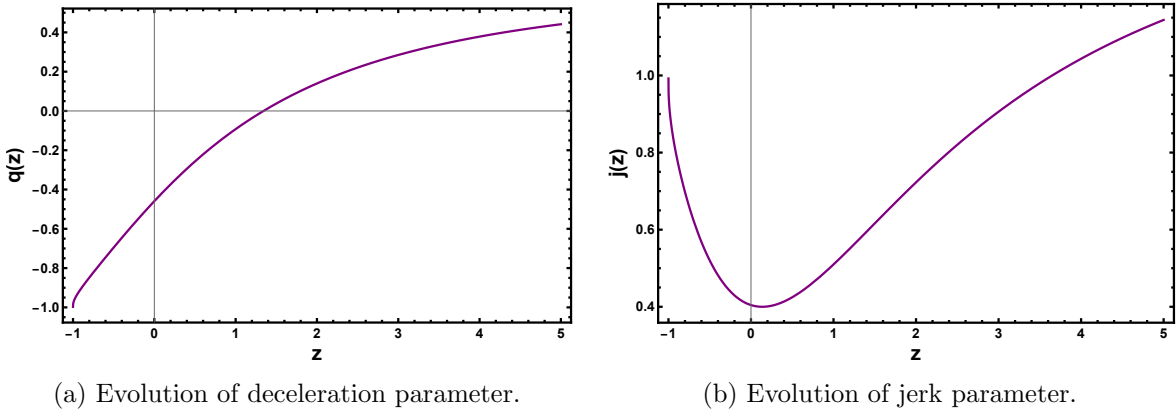


FIGURE 2.1: Evolution of cosmographic parameters as a function of redshift.

2.3.1 Log-square-root model

We first consider the logarithmic form of $f(Q)$ [172] as,

$$f(Q) = nQ_0 \sqrt{\frac{Q}{\lambda_1 Q_0}} \ln \frac{\lambda_1 Q_0}{Q} , \quad (2.8)$$

where n and $\lambda_1 > 0$ are free parameters; $Q_0 = 6H_0^2$, where $H_0 = 70.7 \text{ km s}^{-1} \text{ Mpc}^{-1}$ [173] represents the present value of H . For $n = 0$, one can recover the GR equivalent model.

At the outset, we have studied the evolutionary behaviour of the function $f(Q)$ by plotting the graphs $\frac{f(Q)}{H_0^2}$ vs z and f_Q vs z where z is redshift [89]. We wish to analyse $\frac{f(Q)}{H_0^2}$ and f_Q as functions of redshift since the Hubble parameter is related to the scale factor as $H = \frac{\dot{a}}{a}$. One can see from Fig. 2.2a as time passes, $\frac{f(Q)}{H_0^2}$ shows a decreasing behavior and gradually vanishes. Whereas, f_Q [Fig. 2.2b] starts with a lower positive value, increases over time and remains positive throughout. Substituting Eq. (2.8) into Eqs. (2.1), (2.2) and (2.5), we obtain

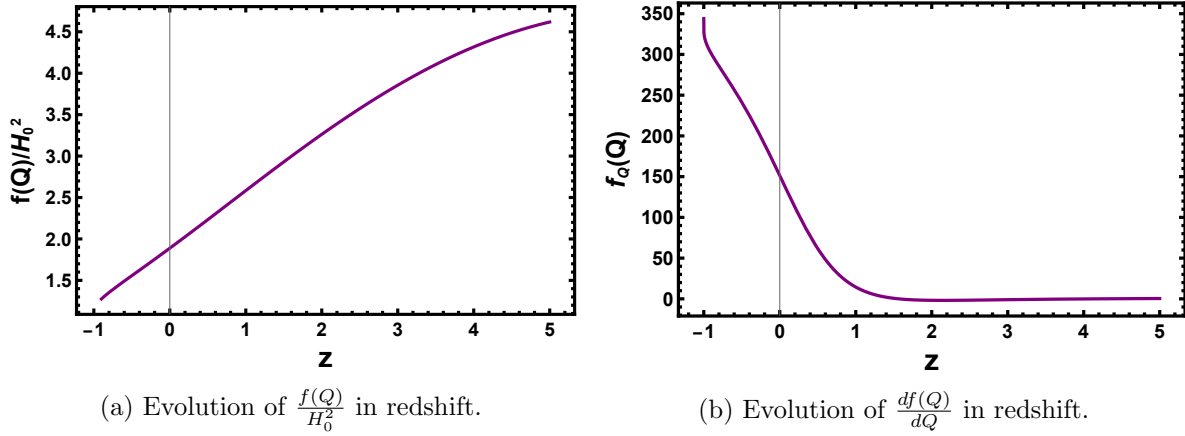


FIGURE 2.2: Evolution of log-square-root model as a function of redshift.

$$p_{total} = \frac{\lambda_1 \Omega_r (z+1)^4 \sqrt{\frac{H^2(z)}{\lambda_1 Q_0}} - 3\sqrt{6} H^2(z)n + \sqrt{6} H(z)n(z+1)H_z(z)}{3\lambda_1 \sqrt{\frac{H^2(z)}{\lambda_1 Q_0}}} , \quad (2.9)$$

$$\rho_{total} = H(z)Q_0n\sqrt{\frac{6}{\lambda_1 Q_0}} + \Omega_r(z+1)^4 + \Omega_m(z+1)^3 , \quad (2.10)$$

$$\omega_{total} = \frac{\lambda_1 \Omega_r (z+1)^4 \sqrt{\frac{H^2(z)}{\lambda_1 Q_0}} - 3\sqrt{6} H^2(z)n + \sqrt{6} H(z)n(z+1)H_z(z)}{3\sqrt{\frac{H^2(z)}{\lambda_1 Q_0}} \left(\sqrt{6}\lambda_1 Q_0 n \sqrt{\frac{H^2(z)}{\lambda_1 Q_0}} + \lambda_1(z+1)^3(\Omega_m + \Omega_r z + \Omega_r) \right)} , \quad (2.11)$$

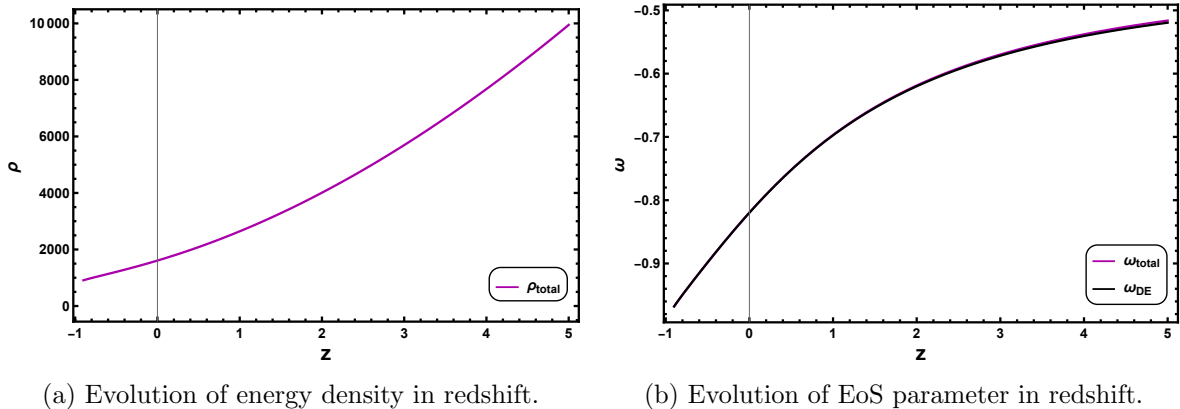


FIGURE 2.3: The behavior of the dynamical parameter for log-square-root model in redshift.

where H_z denotes the derivative of H with respect to z . The parameters ξ , η , n , Q_0 and λ_1 determine the evolutionary behavior of total energy density and EoS parameters. The model parameter has been chosen in such a way that a positive energy density can be obtained Fig. 2.3a. The total energy density is showing decreasing behavior from early epoch to late epoch and remains positive throughout. The total EoS parameter shows quintessence behavior at present epoch, whereas it converges to Λ CDM at late epoch [Fig. 2.3b]. At $z = 0$, the value of total EoS parameter observed to be ≈ -0.82 . The behaviour of DE EoS parameter remains almost same

with that of total EoS parameter. The parameter scheme for the plots is $\xi = 0.965$, $\eta = 0.60$, $n = 1$, $Q_0 = 29990$, $\lambda_1 = 0.35$, $\Omega_m = 0.3$ and $\Omega_r = 0.00001$.

2.3.2 Exponential model

As a second model, we consider an exponential function of $f(Q)$ [88] as,

$$f(Q) = Q e^{\frac{\mu \lambda_2}{Q}} - Q , \quad (2.12)$$

where λ_2 is the free parameter. In the cosmological framework, the model gives rise to a scenario without Λ CDM as a limit, having the same number of free parameters as Λ CDM. In this model, in certain time period of cosmic history, the term $\frac{\mu}{Q}$ decreases, which ends up making the model as polynomial one. We can see the behavior of $\frac{f(Q)}{H_0^2}$ and f_Q in Fig. 2.4. In this model

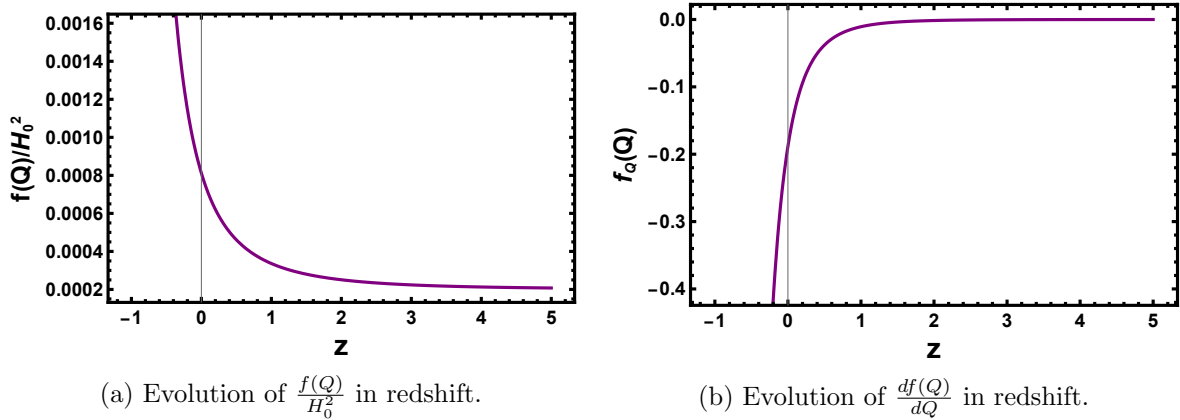


FIGURE 2.4: Evolution of exponential model as a function of redshift.

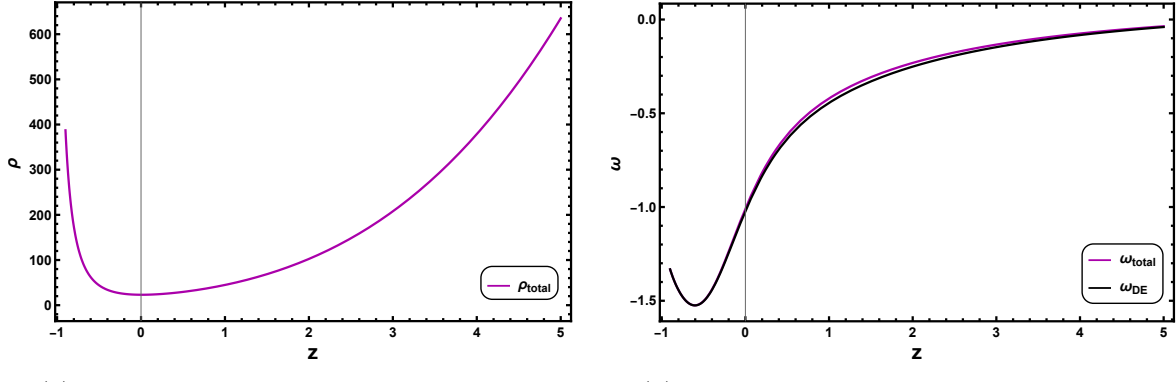
also, the normalized non-metricity function $\frac{f(Q)}{H_0^2}$ increases with cosmic time due to exponential form of model [Fig. 2.4a]. However, the functional f_Q becomes a decreasing function of the redshift [Fig. 2.4b]. The motivation behind these plots is that the non-metricity scalar Q at the FLRW background assumes $6H^2$. To analyse the dynamic behavior of the model, the dynamical parameters can be derived from Eqs. (2.1), (2.2) and (2.5) by incorporating Eq. (2.12) as,

$$\rho_{total} = \frac{1}{6} e^{\frac{\lambda_2 \mu}{6H^2(z)}} \left(\frac{\lambda_2 \mu}{H^2(z)} + 3 \right) + 3H^2(z) + (z+1)^3(\Omega_m + \Omega_r z + \Omega_r) , \quad (2.13)$$

$$\begin{aligned} p_{total} = & -3H^2(z) + 2H(z)(z+1)H_z(z) + \frac{1}{3}\Omega_r(z+1)^4 , \\ & - \frac{e^{\frac{\lambda_2 \mu}{6H^2(z)}} (9H^3(z)(3H^2(z) + \lambda_2 \mu) + \lambda_2 \mu(z+1)H_z(z)(9H^2(z) + \lambda_2 \mu))}{54H^5(z)} , \end{aligned} \quad (2.14)$$

$$\omega_{total} = \frac{-3H^2(z) + 2H(z)(z+1)H_z(z) + \frac{1}{3}\Omega_r(z+1)^4}{\frac{1}{6} e^{\frac{\lambda_2 \mu}{6H^2(z)}} \left(\frac{\lambda_2 \mu}{H^2(z)} + 3 \right) + 3H^2(z) + (z+1)^3(\Omega_m + \Omega_r z + \Omega_r)}$$

$$-\frac{e^{\frac{\lambda_2 \mu}{6H^2(z)}} (9H^3(z) (3H^2(z) + \lambda_2 \mu) + \lambda_2 \mu (z + 1) H_z(z) (9H^2(z) + \lambda_2 \mu))}{54H^5(z) \left(\frac{1}{6} e^{\frac{\lambda_2 \mu}{6H^2(z)}} \left(\frac{\lambda_2 \mu}{H^2(z)} + 3 \right) + 3H^2(z) + (z + 1)^3 (\Omega_m + \Omega_r z + \Omega_r) \right)}. \quad (2.15)$$



(a) Evolution of energy density in redshift. (b) Evolution of EoS parameter in redshift.

FIGURE 2.5: The behavior of the dynamical parameter for exponential model in redshift.

Fig. 2.5a shows the evolutionary behavior of total energy density that remains positive throughout the evolution and at present time it attains the minimum value. The total EoS parameter remains entirely in the negative domain and decreases from early time. The present value has been obtained as, $\omega_{total} = -1.01$ [Fig. 2.5b]. At present the DE EoS parameter remains alike to that of total EoS parameter though there was a marginal change noticed at early time. The parameter scheme for the plots is $\xi = 0.965$, $\eta = 0.60$, $\mu = 6.5$, $\lambda_2 = 6.5$, $\Omega_m = 0.3$ and $\Omega_r = 0.00001$.

The evolutionary behaviors of the dynamical parameters for both the log-square-root model and exponential model have been established and now we proceed to investigate the phase space analysis of these models to further explore their stability and the potential for cosmological solutions.

2.4 Phase space analysis

Any group of elements that evolves over time is a dynamical system, whether they are real or even artificial. The dynamical system is based on differential equations associated with time derivatives. So, it is unlike that there exists any universal theory of dynamical systems. The evolution rule that governs the dynamical system should therefore be analyzed in various ways to find its characteristics [150, 174, 175]. In order to probe the evolutionary dynamics of the theory, we use dynamical systems instead of solving the non-linear differential equations that describes the majority of cosmological models. The stability can be analysed in various methods, some of them are Jacobi stability, Kosambi-Cartan-Chern (KCC) theory or Lyapunov methods. We shall use the Jacobi stability analysis in this problem. We shall perform the dynamical system analysis of the background equations of the two models and will focus on its stability [176, 177]. To do so, we consider 3-dimensionless parameters, x , y and σ , which may give detailed idea

about DE and transform the field equations in terms of the dynamical variables as,

$$x = \frac{f}{6H^2}, \quad y = -2f_Q, \quad \sigma = \frac{\rho_r}{3H^2}.$$

Subsequently, Eq. (2.7) reduces to,

$$\Omega_r = \sigma, \quad \Omega_{DE} = x + y, \quad \Omega_m = 1 - x - y - \sigma, \quad \frac{\dot{H}}{H^2} = \frac{-(3 - 3x - 3y + \sigma)}{2(2Qf_{QQ} + f_Q + 1)}.$$

Here, prime (') represents differentiation with respect to the number of e-folds of the Universe, $N = \ln a$. Then we can differentiate x , y and σ with respect to N to obtain,

$$x' = -\frac{\dot{H}}{H^2}(2x + y) = \frac{(3 - 3x - 3y + \sigma)(2x + y)}{2(2Qf_{QQ} + f_Q + 1)}, \quad (2.16)$$

$$y' = -\frac{\dot{H}}{H^2}(4Qf_{QQ}) = (3 - 3x - 3y + \sigma) \left[1 + \frac{(y - 2)}{2(2Qf_{QQ} + f_Q + 1)} \right], \quad (2.17)$$

$$\sigma' = -\sigma \left[4 + 2 \frac{\dot{H}}{H^2} \right] = \sigma \left[\frac{(3 - 3x - 3y + \sigma)}{(2Qf_{QQ} + f_Q + 1)} - 4 \right]. \quad (2.18)$$

Now, we can redefine ω_{total} and ω_{DE} as

$$\omega_{total} = -1 - \frac{2}{3} \frac{\dot{H}}{H^2}, \quad \omega_{DE} = -1 - \frac{1}{3(x + y)} \left[y' + \frac{\dot{H}}{H^2} y \right].$$

For $f(Q) = nQ_0 \sqrt{\frac{Q}{\lambda_1 Q_0}} \ln \left(\frac{\lambda_1 Q_0}{Q} \right)$, one can express Eqs. (2.16)-(2.18) in terms of dynamical variables as,

$$x' = \frac{(2x + y)(3 - 3x - 3y + \sigma)}{(2 - x - y)}, \quad (2.19)$$

$$y' = \frac{x(3x + 3y - 3 - \sigma)}{(2 - x - y)}, \quad (2.20)$$

$$\sigma' = \frac{2\sigma(\sigma - x - y - 1)}{(2 - x - y)}. \quad (2.21)$$

Moreover, the total EoS parameter and EoS parameter for DE can be written in dynamical variables as,

$$\omega_{total} = -1 - \frac{2}{3} \left(\frac{3x + 3y - \sigma - 3}{2 - x - y} \right), \quad \omega_{DE} = -\frac{3 - \sigma}{3(2 - x - y)}.$$

Table 2.1 provides the critical points and the cosmological behaviour at these points. The details description of each critical point has been narrated below. In Fig. 2.6, the 2D and 3D phase portrait have been given to understand the stability of these points.

- **Critical point A_1 (0, 0, 1) :** The corresponding EoS parameter and deceleration

Name	Point/Curve	Ω_m	Ω_r	Ω_{DE}	q	ω_{total}	ω_{DE}	Phase of Universe	Stability
A_1	$(0, 0, 1)$	0	1	0	1	$\frac{1}{3}$	$-\frac{1}{3}$	Radiation dominated	Unstable Node
B_1	$(0, 0, 0)$	1	0	0	$\frac{1}{2}$	0	$-\frac{1}{2}$	Matter dominated	Unstable Saddle
C_1	$(x, 1-x, 0)$	0	0	1	-1	-1	-1	Dark Energy dominated	Stable Node

TABLE 2.1: Critical Points and the corresponding cosmology for log-square-root model.

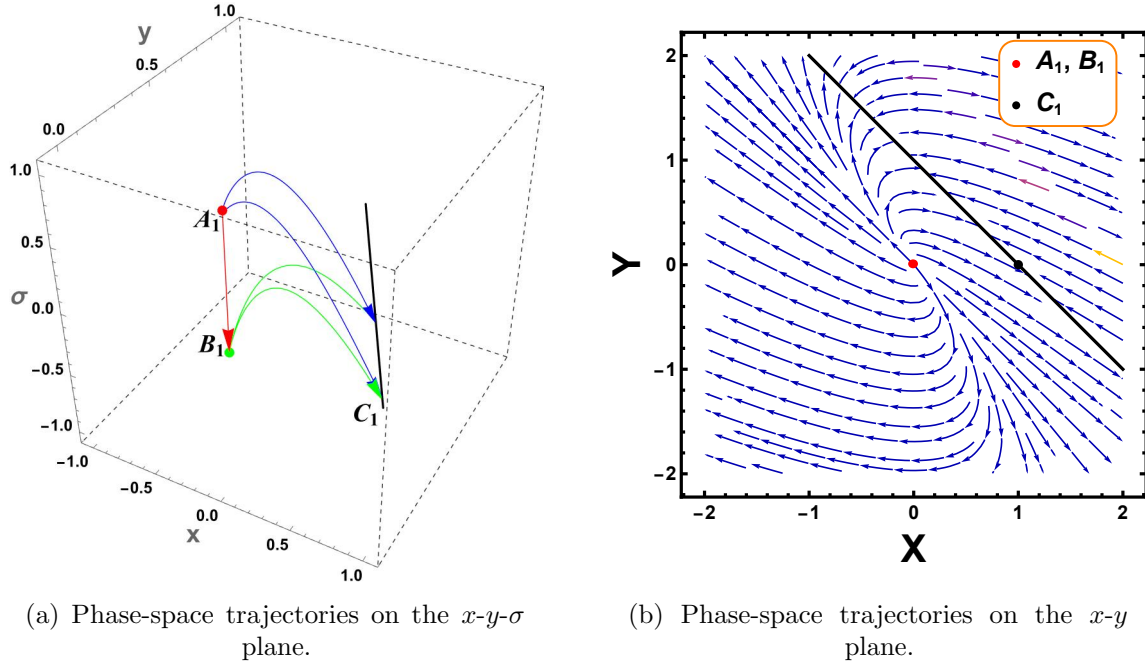


FIGURE 2.6: The phase-space portrait for log-square-root model.

parameter is $\omega_{total} = \frac{1}{3}$ and $q = 1$ respectively. This behaviour of the critical point leads to the decelerating phase of the Universe. The density parameters are, $\Omega_{DE} = 0$, $\Omega_m = 0$ and $\Omega_r = 1$. This critical point is an unstable node because it contains all positive eigenvalues of the Jacobian matrix,

$$\{2, 2, 1\}.$$

- **Critical point $B_1 (0, 0, 0)$** : The critical point leads to the decelerating phase of the Universe, since the EoS parameter corresponding to this critical point is $\omega_{total} = 0$ and deceleration parameter is $q = \frac{1}{2}$. The corresponding density parameter are $\Omega_{DE} = 1$, $\Omega_m = 0$ and $\Omega_r = 0$. The critical point shows unstable saddle behaviour. The eigenvalues

for corresponding critical point shows positive and negative signature as shown below:

$$\left\{ \frac{3}{2}, \frac{3}{2}, -1 \right\}.$$

- **Curve of critical points $C_1(x, 1-x, 0)$:** At this point, $\Omega_{DE} = 1$, $\Omega_m = 0$ and $\Omega_r = 0$, i.e. the Universe shows DE dominated phase. The accelerated DE dominated Universe is confirmed by the corresponding value of the EoS parameter ($\omega_{total} = -1$) and value of the deceleration parameter ($q = -1$). Jacobian matrices with critical points have negative real parts and zero eigenvalues. Further, there is only one vanishing eigenvalue and therefore the dimension of the set of eigenvalues equals its number. As a result, the set of eigenvalues is normally hyperbolic, the critical point associated with it cannot be a global attractor [178, 179]. This critical point, shows stable node behaviour. The corresponding eigenvalues are given below:

$$\{-4, -3, 0\}.$$

From the phase portrait [Fig. 2.6], we can see that the critical point A_1 is unstable node, where as curve $[(x, 1-x, 0)]$ is stable node. The B_1 is unstable saddle point. Fig. 2.6a describes the trajectories for critical points, where A_1 is the repeller, so it repels every trajectory and C_1 is the attractor, so it absorbs every trajectory coming towards it. The B_1 is saddle therefore, it absorbs the trajectories coming from A_1 and repel the trajectories originated from itself. Fig. 2.6b, one can observe that the stability is not only specific to the single point but also in the entire curve $(x, 1-x, 0)$. This kind of stability behaviour may be due to the fact that irrespective of the value of the dynamical variable x , it exhibits the stable behaviour. It may be due to the nature of the dynamical variable x . The 3D portrait shows the trajectory behaviour of the model starting from repeller point A_1 to the saddle point B_1 and then it is moving from B_1 to the stable curve C_1 . Further, the evolution plot for log-square-root model has been given in Fig. 2.7 utilizing the initial conditions $x = 10^{-15}$, $y = 10^{-6}$ and $\sigma = 10^{-1}$. From the evolution curve, the present value of DE EoS parameter is -0.80 whereas the value obtained using the hybrid scale factor is -0.82 . Hence in both the approaches, we can get similar value at present time and the Universe shows quintessence behaviour. At present the value of density parameters for DE and matter obtained as ≈ 0.7 and ≈ 0.3 respectively.

For, $f(Q) = Qe^{\frac{\mu\lambda_2}{Q}} - Q$, we can get the system of differential equations as,

$$x' = \frac{(3 - 3x - 3y + \sigma)(2x + y)}{2 - y + 4(x + 1)[\ln(x + 1)]^2}, \quad (2.22)$$

$$y' = \frac{4(x + 1)(3 - 3x - 3y + \sigma)[\ln(x + 1)]^2}{2 - y + 4(x + 1)[\ln(x + 1)]^2}, \quad (2.23)$$

$$\sigma' = 2\sigma \left[\frac{3 - 3x - 3y + \sigma}{2 - y + 4(x + 1)[\ln(x + 1)]^2} - 2 \right]. \quad (2.24)$$

On a similar note, we can obtain the EoS parameters as,

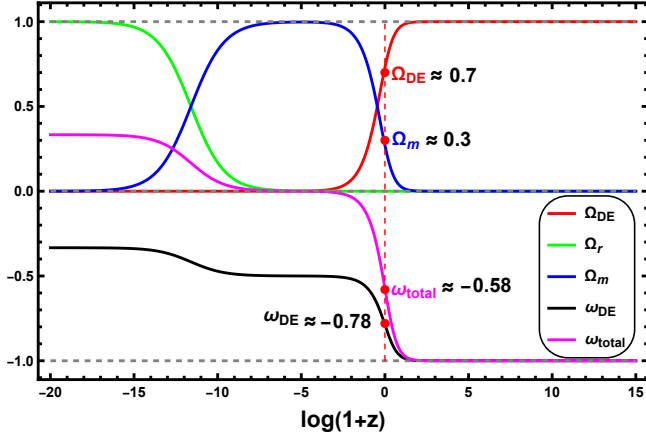


FIGURE 2.7: Evolution of EoS Parameter and density parameters for log-square-root model. The vertical dashed red line denotes the present time.

$$\begin{aligned} \omega_{total} &= -1 + \frac{6(x+y-1) - 2\sigma}{3(2-y+4(x+1)[\ln(x+1)]^2)}, \\ \omega_{DE} &= \frac{-4(\sigma+3)[\ln(x+1)]^2 - 2x(6[\ln(x+1)]^2(x+1) + 2\sigma[\ln(x+1)]^2 + 3) + y(\sigma-3)}{3(x+y)(2-y+4(x+1)[\ln(x+1)]^2)}. \end{aligned}$$

Name	Point/Curve	Ω_m	Ω_r	Ω_{DE}	q	ω_{total}	ω_{DE}	Phase of Universe	Stability
A_2	(0, 0, 1)	0	1	0	1	$\frac{1}{3}$	-	Radiation dominated	Unstable Node
B_2	(0, 0, 0)	1	0	0	$\frac{1}{2}$	0	-	Matter dominated	Unstable Saddle
C_2	$(x, 1-x, 0)$	0	0	1	-1	-1	-1	Dark Energy dominated	Stable Node

TABLE 2.2: Critical Points and the corresponding cosmology for exponential model.

Table 2.2 provides the critical points and the cosmological behaviour at these points. The details description of each critical point has been narrated below. In Fig. 2.8, the 2D and 3D phase portrait have been given to understand the stability of these points.

- **Critical point A_2 (0, 0, 1)** : The critical point leads to the decelerating phase of the Universe, since the EoS parameter and deceleration parameter corresponding to this critical point is $\omega_{total} = \frac{1}{3}$ and $q = 1$ respectively. The corresponding density parameter are $\Omega_{DE} = 0$, $\Omega_m = 0$ and $\Omega_r = 1$. This critical point shows unstable behaviour. The

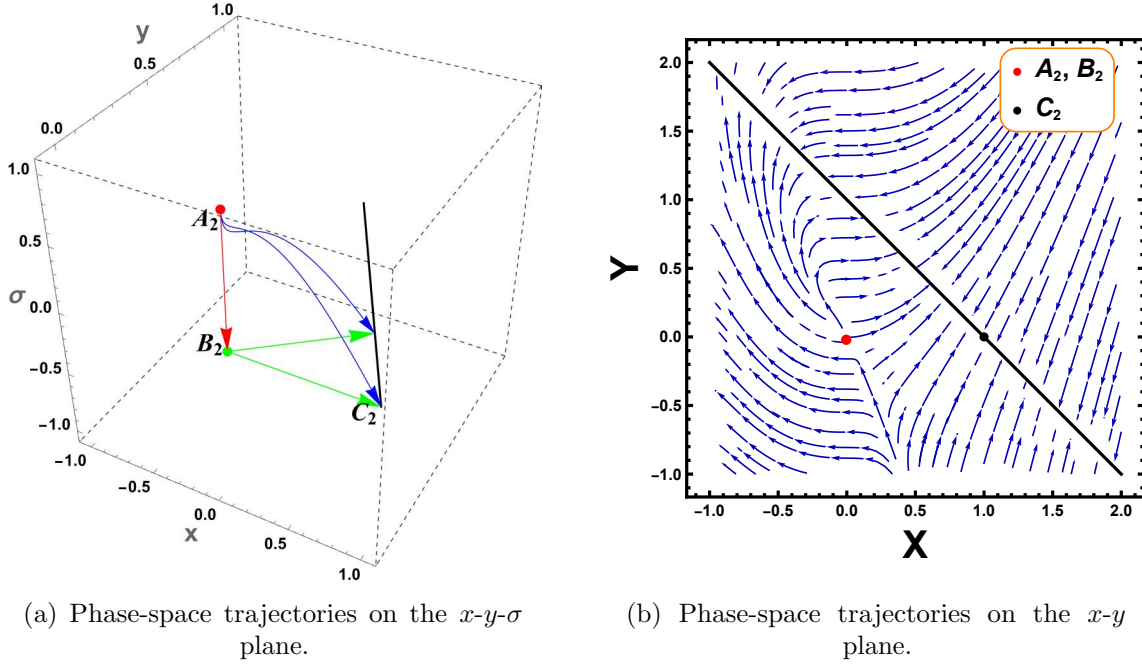


FIGURE 2.8: The phase-space portrait for exponential model.

eigenvalues for the corresponding critical point shows positive signature as given below:

$$\{4, 1, 0\}.$$

- **Critical point B_2 $(0, 0, 0)$** : At this point, $\Omega_{DE} = 0$, $\Omega_m = 1$ and $\Omega_r = 0$, i.e. the Universe shows matter dominated phase. The decelerated matter dominated Universe is confirmed by the corresponding value of the EoS parameter ($\omega_{total} = 0$) and deceleration parameter $q = \frac{1}{2}$. Jacobian matrices with critical points have positive, negative real parts and zero eigenvalues. This critical point shows unstable saddle behaviour. The corresponding eigenvalues are given below:

$$\{3, -1, 0\}.$$

- **Curve of critical point C_2 $(x, 1-x, 0)$** : The corresponding EoS parameter is $\omega_{total} = -1$ and deceleration parameter is $q = -1$. This behaviour of the critical point leads to the accelerating phase of the Universe. Also, density parameters are $\Omega_{DE} = 1$, $\Omega_m = 0$ and $\Omega_r = 0$. This critical point is a stable node because it contains negative real part and zero eigenvalues of the Jacobian matrix.

$$\{0, -4, -3\}.$$

The phase portrait, which shows comparable trajectory plots, is an important tool in the study of dynamical systems. The stability of the models can be tested using the phase portrait. The phase portrait for system given in Eqs. (2.22)-(2.24) is shown in Fig. 2.8. The figure 2.8a shows the trajectories in x - y - σ (3D) plane and figure 2.8b shows the trajectories in x - y (2D) plane,

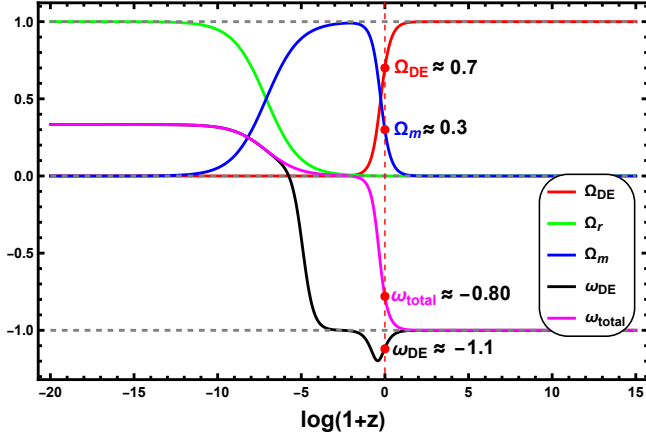


FIGURE 2.9: Evolution of EoS parameter and density parameters for exponential model. The vertical dashed red line denotes the present time.

since $\sigma = 0$ is an invariant sub-manifold. Here, also the stability obtained along the curve $(x, 1 - x, 0)$. This again shows the role of the dynamical variable x . Similar to log-square-root model, the 3D phase portrait for exponential model shows attracting behaviour at critical curve C_2 . All the repelling trajectories going away from critical points A_2 and B_2 and moving towards the stable curve C_2 . From the evolution plot [Fig. 2.9], the present value of $\omega_{DE} = -1.1$ which is almost same as that of the value obtained through the scale factor. The initial conditions are taken as $x = 10^{-15}$, $y = 10^{-6}$ and $\sigma = 10^{-1}$.

2.5 Results and Conclusion

In this chapter, we explored cosmological models within the framework of symmetric teleparallel gravity or $f(Q)$ gravity, by introducing two distinct models: a log-square-root model and an exponential model. Both models were examined using a time varying deceleration parameter to capture the transition of the Universe from early deceleration to late-time acceleration. A log-square-root model demonstrates a quintessence behavior at present, converging to Λ CDM at late-time, while exponential model shows a phantom behavior.

The dynamical system analysis revealed that both models exhibit unstable behavior during the radiation and matter phases but attain stability in the de Sitter phase, consistent with the desired features of an accelerating Universe. The phase portraits and critical points underscore the ability of the model to transition through different cosmological eras, with stable nodes indicating a late-time de Sitter phase. These findings support the potential of non-metricity gravity to produce stable cosmological models that align with the observed late-time cosmic acceleration, offering insights into the evolutionary history of the Universe. The study highlights the importance of the EoS parameter and the role of model parameters in constraining the behavior of dynamical parameters, confirming the stability of the models through comprehensive analysis.

Chapter 3

Phantom cosmological model with observational constraints in $f(Q)$ gravity

* The work, in this chapter, is covered by the following publication:

S. A. Narawade and B. Mishra, “Phantom cosmological model with observational constraints in $f(Q)$ gravity”, *Ann. der Phys.* **535** (2023) 2200626.

3.1 Introduction

In recent years, significant advancements have been made in cosmological models through the integration of observational data. Seikel et al. [180] introduced new consistency tests for the Λ CDM model, formulated in terms of the Hubble parameter $H(z)$. The acceleration of the expansion of the Universe has been studied by parametrize the EoS parameter of DE with analyses based on four distinct sets of Type Ia supernovae data [181]. Wei et al. [182] tested ten cosmological models against the Hubble data set to validate their predictions. Farooq et al. [183] constrained both spatially flat and curved dark energy models by utilizing $H(z)$ data from the redshift range (0.07, 2.36). Mukherjee et al. [184] discussed a parametric reconstruction of the jerk parameter, which represents the third order time derivative of the scale factor in a dimensionless form. Additionally, for a bulk viscous anisotropic Universe, the Hubble parameter values obtained using various datasets Hubble, Pantheon and Hubble+Pantheon are $H_0 = 69.39 \pm 1.54 \text{ } \text{km s}^{-1} \text{Mpc}^{-1}$, $70.016 \pm 1.65 \text{ } \text{km s}^{-1} \text{Mpc}^{-1}$ and $69.36 \pm 1.42 \text{ } \text{km s}^{-1} \text{Mpc}^{-1}$ respectively [185].

Based on the analysis of dynamical stability in previous chapters, this chapter carried out an observational analysis to validate and assess the compatibility of theoretical models with observational data in $f(Q)$ gravity. To do that, we have obtained the Hubble parameter in redshift with some algebraic manipulation from the considered form of $f(Q)$. By performing statistical analysis using the MCMC method, we constrained the free parameters of the $f(Q)$ model, ensuring that it accurately reflects the observed behavior of the Universe. The incorporation of the BAO dataset in this analysis compare the constrained values of free parameter with cosmological observations. Additionally, the study of cosmographic parameters and the $Om(z)$ diagnostic provides further insight into the dynamics of cosmic acceleration, helping to evaluate the performance of the model and its potential to describe key observational features like cosmic expansion and dark energy. This chapter divided into seven sections. In section 3.2, we parametrized the Hubble parameter from the well motivated power-law $f(Q)$ model. The free model parameters are constrained through the MCMC technique and the observational datasets in section 3.3. The section 3.4 validated the Hubble parameter and the constrained model parameters utilizing the BAO dataset. In section 3.5 the cosmographic parameters introduced, while section 3.6 discusses the $Om(z)$ diagnostic and the age of the Universe. Finally, the results and conclusions are presented in section 3.7.

3.2 Power-law model

To obtain the cosmological parameters, a well-defined form of $f(Q)$ is needed, so that the analysis of the cosmological model can be performed. Capozziello et al. [186] have assumed the Pade's approximation approach to compute a numerical reconstruction of the cosmological observables up to high redshifts. This can reduce the convergence issues associated with standard cosmographic methods and provides an effective method for describing cosmological observables

up to high redshifts. To reconstruct $f(Q)$ through a numerical inversion procedure, utilizing the relation $Q = 6H^2$, the function that provides the best analytical match to the numerical results is given by

$$f(Q) = \alpha + \beta Q^n , \quad (3.1)$$

where α , β and n are free model parameters, the parameter $n > 1$ is a real number responsible for the accelerating phase in the early Universe [187]. There are several $f(Q)$ models which shares the same background evolution as in Λ CDM, while leaving precise and measurable effects on cosmological observable. But with the increase in redshift, the function $f(Q) = \alpha + \beta Q^n$ suggests small deviations from the Λ CDM model. For $\alpha = 0$, $\beta = 1$ and $n = 1$, one can recover the aforementioned class of theories with the same background evolution as in GR.

3.2.1 $H(z)$ parameterization

The model parameters present in Eq. (3.1) will regulate the dynamical behaviour of the model. The value of the model parameters α , β and n to be chosen in such a way that the deceleration parameter attain the value, $q_0 = -0.54$ [188–190]. From the relationship between scale factor and redshift, $a(t) = \frac{1}{1+z}$, one can get, $H = \frac{-\dot{z}}{1+z}$. Now, from Eqs. (1.65) and (1.66), we obtain

$$\dot{H} = \frac{-(1+\omega)}{4} \frac{2Qf' - f}{2Qf'' + f'} . \quad (3.2)$$

Subsequently,

$$\frac{dH}{dz} = \frac{(1+\omega)}{4H(1+z)} \frac{2Qf' - f}{2Qf'' + f'} , \quad (3.3)$$

Substituting Eq. (3.1) in Eq. (3.3), we get

$$H(z) = H_0 \left[\sqrt{\frac{\alpha + (1+z)^{3(1+\omega)}}{2\beta n 6^n - \beta 6^n}} \right]^{\frac{1}{n}} , \quad (3.4)$$

where H_0 is the present value of the Hubble parameter. Now, our aim is to put constraint on the parameters α , β , n and ω using the cosmological datasets. For dark energy dominated phase (ω is constant) and matter dominated phase ($\omega = 0$), we obtain the following relation for the Hubble parameter, which is analogous to epsilon model given in [191],

$$H(z)^2 = H_0^2 \left[\left(1 - \frac{\alpha + 1}{\beta(2n-1)6^n} \right) (1+z)^3 + \frac{1}{\beta(2n-1)6^n} (1+z)^{3(1+\omega)} + \frac{\alpha}{\beta(2n-1)6^n} \right]^{\frac{1}{n}} . \quad (3.5)$$

The parametrization of $H(z)$ derived above will be used to place constraints on the model parameters through various observational datasets, which are discussed in the next section. These datasets will provide the required observational information to test the validity of the model.

3.3 Observational datasets

3.3.1 Hubble dataset

By estimating their differential evolution, early type galaxies offer measurements of the Hubble parameter. The process of compilation these observations is referred to as the cosmic chronometers method. The list of 32 data points of Hubble parameter in the redshift range $0.07 \leq z \leq 1.965$ with errors (see [Appendices](#)). By minimizing the chi-square value, we determine the mean values of the model parameters α , β and n . The Chi-square function can be given as,

$$\chi_{\text{OHD}}^2(p_s) = \sum_{i=0}^{32} \frac{[H_{th}(z_i, p_s) - H_{obs}(z_i)]^2}{\sigma_H^2(z_i)} , \quad (3.6)$$

where $H_{th}(z_i, p_s)$ represents the Hubble parameter with the model parameters, $H_{obs}(z_i)$ represents the observed Hubble parameter values and $\sigma_H^2(z_i)$ is the standard deviation.

3.3.2 Pantheon+SH0ES dataset

The Pantheon+SH0ES sample dataset consists of 1701 light curves of 1550 distinct Type Ia Supernovae ranging in redshift from $z = 0.00122$ to 2.2613 [\[137\]](#). The model parameters are to be fitted by comparing the observed and theoretical value of the distance moduli. The distance moduli with nuisance parameter μ_0 can be defined as,

$$\mu(z, \theta) = 5\log_{10}[d_L(z, \theta)] + \mu_0 , \quad (3.7)$$

where d_L is the dimensionless luminosity distance defined as,

$$d_L(z) = (1+z) \int_0^z \frac{dz^*}{E(z^*)} , \quad \left(E(z) = \frac{H(z)}{H_0} \right) \quad (3.8)$$

where z^* is variable change to define integration from 0 to z . The χ^2 is given by,

$$\chi_{SN}^2(z, \theta) = \sum_{i=1}^{1701} \frac{[\mu(z_i, \theta)_{th} - \mu(z_i)_{obs}]^2}{\sigma_\mu^2(z_i)} , \quad (3.9)$$

where $\sigma_\mu^2(z_i)$ is the standard error in the observed value. In order to calculate χ_{SN}^2 , we use the fact that the SNe Ia dataset corresponds to redshifts below 2 so that we can neglect the contribution from radiation in Einstein's equation.

3.3.3 MCMC analysis and Results

To obtain tight constraints on the parameters of the $f(Q)$ model, the MCMC analysis will be used to perform the test. This analysis will produce proficient fits of α , β , ω and n upon

minimization of a total χ^2 . Also, this analysis will produce selection criteria, which will allow us to draw some conclusions. The panels on the diagonal in corner MCMC plot shows the $1D$ curve for each model parameter obtained by marginalizing over the other parameters, with a thick line curve to indicate the best fit value. The off diagonal panels show $2D$ projections of the posterior probability distributions for each pair of parameters, with contours to indicate 1σ (Blue) and 2σ (Light Blue) regions.

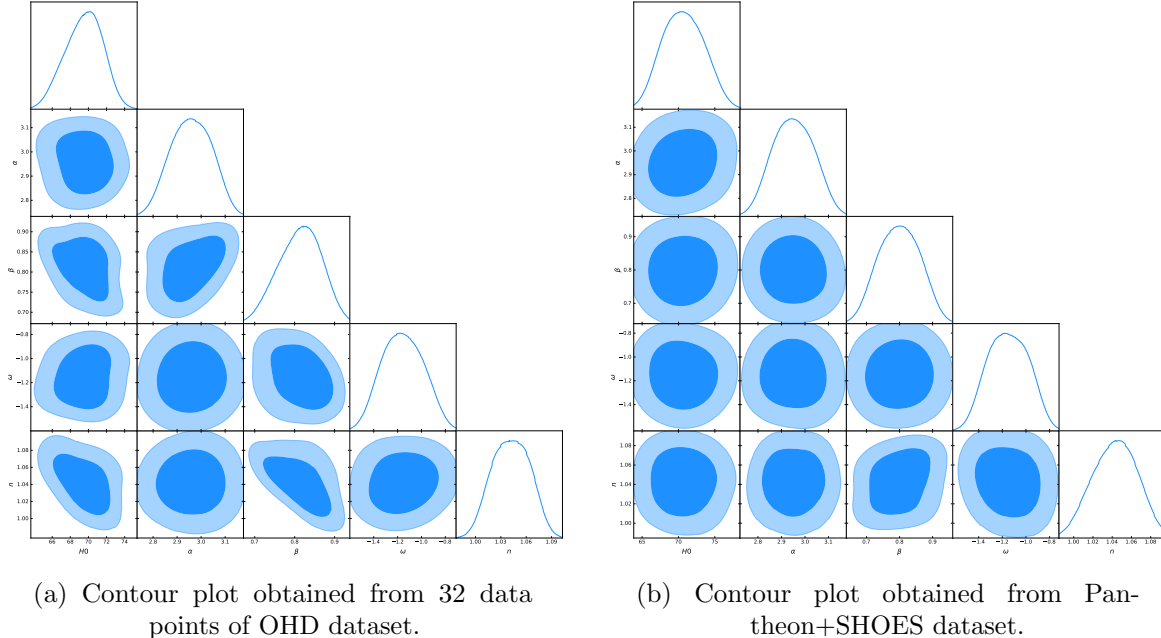


FIGURE 3.1: MCMC contour plot obtained from the observational datasets for 1σ and 2σ confidence interval.

The best fit values of α , β , ω and n are obtained from the triangle plot Fig. 3.1a through Hubble data and in triangle plot Fig. 3.1b using Pantheon+SHOES data with 1σ and 2σ confidence intervals. All the obtained values are listed in Table 3.1. In Fig. 3.2a, the curve for distance modulo has been given as the distance modulo can also expressed in Hubble parameter Eq. (3.5). Here, the solid red line passed in the middle through the error bar plots [Fig. 3.2a], where we used best fit values from Table 3.1 to plot the error bar plot. Also, in Fig. 3.2b, we have shown the error bar plots of $H(z)$ and $H(z)/(1+z)$ [Fig. 3.2c] using the best fit values obtained in Table 3.1. The dotted line represents the Λ CDM line and the solid red line represents the best fit curve for Hubble rate. It can be observed that in both the figures, the solid red line is traversing at the middle of the error bars. We have marginalized value of H_0 as $69.5^{+2.3}_{-1.9} km s^{-1} Mpc^{-1}$ and $70.7 \pm 2.7 km s^{-1} Mpc^{-1}$ respectively with Hubble data and Pantheon+SHOES datasets. The detailed values of the parameters are given in Table 3.1. For the subsequent study, we follow $H_0 = 70.7 \pm 2.7 km s^{-1} Mpc^{-1}$.

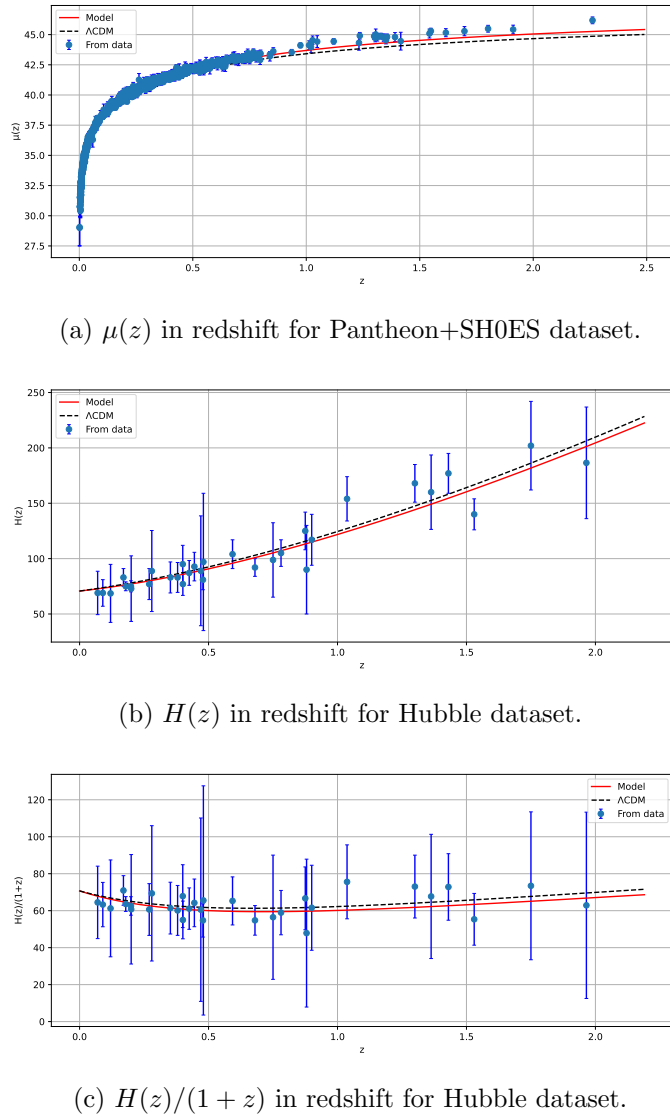


FIGURE 3.2: Error bar plot obtained from the observational datasets.

Parameters	Hubble dataset	Pantheon+SH0ES dataset
H_0	$69.5^{+2.3}_{-1.9}$	70.7 ± 2.7
ω	-1.16 ± 0.17	-1.15 ± 0.17
α	2.96 ± 0.082	2.951 ± 0.082
β	0.813 ± 0.059	0.796 ± 0.0059
n	1.041 ± 0.021	1.043 ± 0.022

TABLE 3.1: The marginalized constraining results of the parameters using Hubble and Pantheon+SH0ES data.

The constraints derived from the Hubble and Pantheon+SH0ES datasets provide valuable insights into the model parameters. To further strengthen these results and test the consistency of the

model, we now proceed to validate the parameters using BAO/CMB dataset, as outlined in the next section.

3.4 BAO/CMB validation

In Λ CDM observations, the BAO standard ruler measurements are self consistent with CMB observations, as demonstrated by several galaxy surveys. As mentioned, our model has a similar background to Λ CDM but shows slight deviations at high redshift. So we can obtain stringent constraints on cosmological parameters by using this measurements. To map distance-redshift relationships, measuring the BAOs in large scale clustering patterns of galaxies is a promising technique. Also, BAO provides an independent way to measure the expansion rate of the Universe and also can describe the rate of change of expansion throughout the evolution history.

3.4.1 BAO dataset

The angular diameter distance through the clustering perpendicular to the line of sight can be measured using the BAO signals. Moreover, the expansion rate of the Universe $H(z)$ can be measured by the clustering along the line of sight. At the photon decoupling epoch, the comoving sound horizon can be defined as,

$$r_s(z_*) = \frac{c}{\sqrt{3}} \int_0^{1/(1+z_*)} \frac{d\tilde{z}}{\tilde{z}^2 H(\tilde{z}) \sqrt{1 + \tilde{z} (3\Omega_{b0}/4\Omega_{\gamma0})}} , \quad (3.10)$$

where, Ω_{b0} and $\Omega_{\gamma0}$ respectively represent the present value of the baryon and photon density parameter and z_* is the redshift of photon decoupling. According to WMAP7 [192], here we use, $z_* = 1091$. The expression for the comoving angular-diameter distance $[d_A(z_*)]$ and the dilation scale $[D_V(z)]$ are respectively,

$$d_A(z_*) = \int_0^{z_*} \frac{d\tilde{z}}{H(\tilde{z})} , \quad D_V(z) = \left[\frac{(d_A(z))^2 c z}{H(z)} \right]^{\frac{1}{3}} . \quad (3.11)$$

The epoch at which baryons were released from photons called as drag epoch (z_d). At this epoch, the photon pressure is no longer able to avoid gravitational instability of the baryons. We use the value, $z_d = 1020$ [193].

3.4.2 CMB dataset

The CMB is leftover radiation from the Big Bang or the time when the Universe starts evolution. In order to confront the dark energy models to CMB data, the distance priors method is more

appropriate [194, 195]. Using the CMB temperature power spectrum, this method measures two distance ratios:

- (i) The acoustic scale, measures the ratio of the angular diameter distance to the decoupling epoch. At decoupling epoch, it also measures the size of the comoving sound horizon. This first distance ratio can be expressed as,

$$l_A = \pi \frac{d_A(z_*)}{r_s(z_*)} .$$

- (ii) The second one is at decoupling time, the ratio of angular diameter distance and the Hubble ratio, called the shift parameter. This can be expressed as,

$$R = \sqrt{\Omega_m H_0^2 r(z_*)} .$$

The acoustic scale is used to obtain the BAO/CMB constraints. Combining these results with the WMAP7-year [192] and WMAP9-year [196] the value $l_A = 302.44 \pm 0.80$ and $l_A = 302.35 \pm 0.65$ respectively. Percival et al. [197] measured $\frac{r_s(z_d)}{D_V(z)}$, at $z = 0.2$ and $z = 0.35$. The WiggleZ team [198] obtained results at $z = 0.44$, $z = 0.60$ and $z = 0.73$ and the 6dF Galaxy Survey also reported a new measurement of $\frac{r_s(z_d)}{D_V(z)}$ at $z = 0.106$ [199]. By using the WMAP 7 [192], recommended values for $r_s(z_d)$ and $r_s(z_*)$ we get, $\frac{r_s(z_d)}{r_s(z_*)} = 1.045 \pm 0.016$. The BAO/CMB constraints $\frac{d_A(z_*)}{D_V(z_{BAO})}$ also exhibited in Table 6.3, along with the values for $\frac{d_A(z_*)}{D_V(z_{BAO})} \frac{r_s(z_d)}{r_s(z_*)}$. The χ^2 for the BAO/CMB can be written as,

$$\chi_{\text{BAO/CMB}}^2 = X^T C^{-1} X , \quad \text{where} \quad X = \begin{pmatrix} \frac{d_A(z_*)}{D_V(0.106)} - 30.95 \\ \frac{d_A(z_*)}{D_V(0.200)} - 17.55 \\ \frac{d_A(z_*)}{D_V(0.350)} - 10.11 \\ \frac{d_A(z_*)}{D_V(0.440)} - 8.44 \\ \frac{d_A(z_*)}{D_V(0.600)} - 6.69 \\ \frac{d_A(z_*)}{D_V(0.730)} - 5.45 \end{pmatrix} ,$$

and the inverse of covariance matrix C is given by [200],

$$C^{-1} = \begin{pmatrix} 0.48435 & -0.101383 & -0.164945 & -0.0305703 & -0.097874 & -0.106738 \\ -0.101383 & 3.2882 & -2.45497 & -0.0787898 & -0.252254 & -0.2751 \\ -0.164945 & -2.45497 & 9.55916 & -0.128187 & -0.410404 & -0.447574 \\ -0.0305703 & -0.0787898 & -0.128187 & 2.78728 & -2.75632 & 1.16437 \\ -0.097874 & -0.252254 & -0.410404 & -2.75632 & 14.9245 & -7.32441 \\ 0.106738 & -0.2751 & -0.447574 & 1.16437 & -7.32441 & 14.5022 \end{pmatrix} .$$

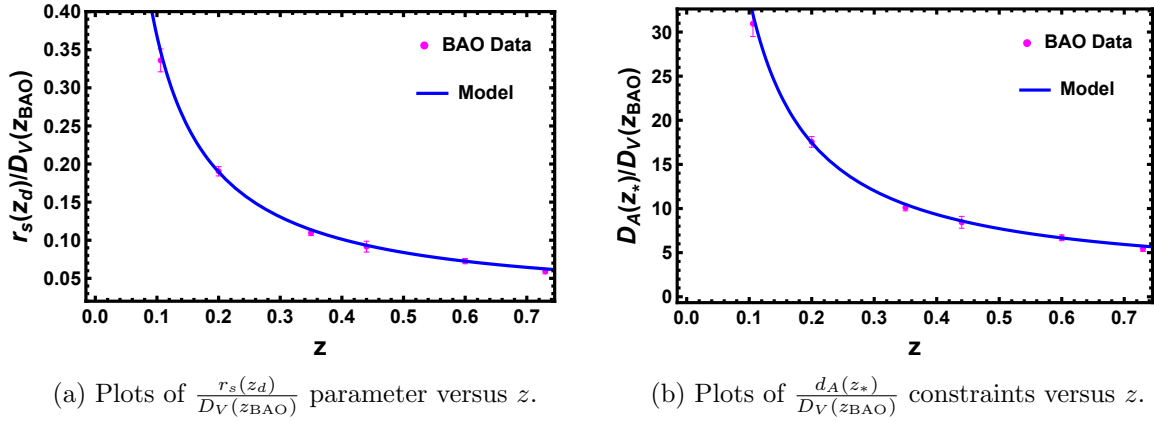


FIGURE 3.3: Error bar plot for the model utilizing BAO/CMB dataset.

The plot for the distilled parameter and BAO/CMB constraints has been made using the $H_0 = 70.7 \text{ km s}^{-1} \text{ Mpc}^{-1}$, $\omega = -1.15$, $\alpha = 2.95$, $\beta = 0.796$ and $n = 1.043$ that we obtained in Table 3.1. The values which we have obtained in our results are best suited with the observational values of the BAO/CMB, as can be seen in Fig. 3.3.

The BAO/CMB datasets have validated the model parameters, ensuring their consistency with observational data. To gain a deeper understanding of the cosmological dynamics, we now proceed to explore the cosmographic parameters, which provide an alternative way to analyze the evolution of the Universe and test the predictions of the model, as discussed in the following section.

3.5 Cosmographic parameters

As explained in the cosmographic series (1.32), the Hubble parameter is derived from the scale factor. The second and third derivative of the cosmographic series, the deceleration parameter (q) and jerk parameter (j) can be determined respectively. The Hubble parameter indicates the rate of the expansion of the Universe and it is a key element in characterizing the evolution of the Universe. For the expanding behaviour of the Universe, the Hubble parameter must be positive. The negative and positive sign of the deceleration parameter respectively gives the information on the accelerating and decelerating behaviour of the Universe. Now, using (3.5), these parameters can be expressed in redshift as,

$$\begin{aligned} q(z) &= -1 + \frac{(1+z)H_z(z)}{H(z)}, \\ j(z) &= q(z)[1+2q(z)] + (1+z)q_z(z). \end{aligned} \quad (3.12)$$

The interval on the value of q (q_0 denotes the present value) describes the behaviour of the Universe as follow:

- (i) The Universe experiences expanding behaviour and undergoes deceleration phase for $q_0 > 0$. During this phase, one can obtain pressureless barotropic fluid or matter dominated Universe. However, the results from cosmological observations do not favor positive q_0 . This situation would have occurred during early Universe.
- (ii) The expanding and accelerating Universe represents for $-1 < q_0 < 0$, which is the present status of the Universe.
- (iii) The entire cosmological energy budget is dominated by a de Sitter fluid for $q_0 = -1$, representing a cosmic component with a constant energy density that remains unchanged as the Universe expands. This is the case of inflation during the very early Universe.

From Eq. (3.12), the present value of the jerk parameter can be, $j_0 = 2q_0^2 + q_0 + q_{z|_0}$. We wish to keep, $-1 < q_0 < -0.5$, which requires $2q_0^2 + q_0 > 0$. Hence, if $q_0 < -0.5$, then j_0 is linked to the sign of the variation of q . Accordingly the behaviour of this geometrical parameter can be interpreted as follows:

- (i) when j_0 is negative, there is no change of the behaviour from the present phase to the accelerated phase. The dark energy influences early time dynamics without any change since the start of evolution.
- (ii) when j_0 vanishes, the accelerating parameter tends smoothly to a precise value, without any change in its behavior.
- (iii) when j_0 is positive, there was a precise point during the evolution when the acceleration of the Universe began. The corresponding redshift can be referred as the transition redshift, at which the effect of dark energy becomes significant. As a consequence, it indicates the presence of further cosmological resources. In order to constrain the DE EoS, one would need to measure the transition redshift z_{tr} directly. To note here, the slope of the Universe gets changed by changing the sign of j_0 .

In Fig. 3.4, we have marginalized the z -values for the present values of $H(z)$, $q(z)$ and $j(z)$. In Table 3.2 the best fit present value of $H(z)$, $q(z)$ and $j(z)$ are given, as obtained from the Hubble and Pantheon+SH0ES data using marginalized model parameter values.

Parameters	Hubble dataset	Pantheon+SH0ES dataset
$H(z)$	$69.5^{+2.3}_{-1.9}$	70.7 ± 2.7
$q(z)$	-0.59 ± 0.07	-0.61 ± 0.067
$j(z)$	1.117 ± 0.02	1.122 ± 0.02

TABLE 3.2: The marginalized constraining results of the cosmographic parameters using Hubble and Pantheon+SH0ES data.

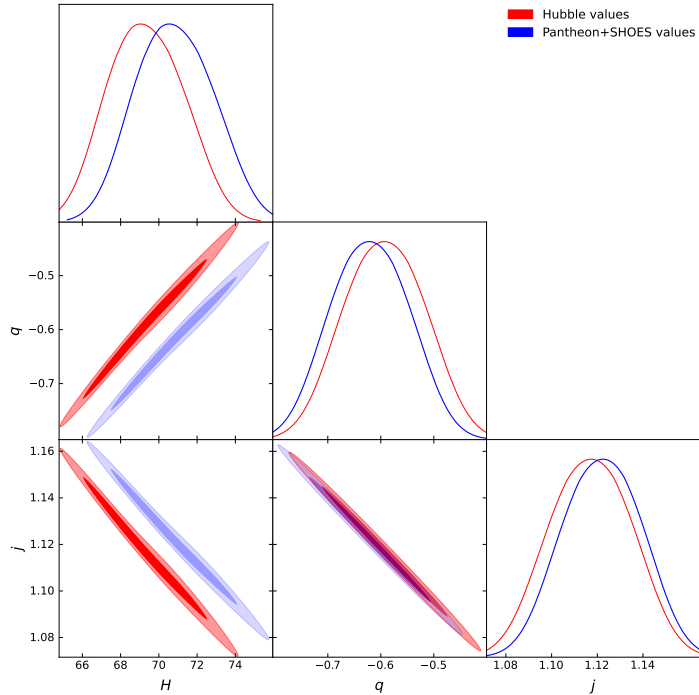


FIGURE 3.4: The marginalized constraints on the $H(z)$, $q(z)$ and $j(z)$ using redshift values.

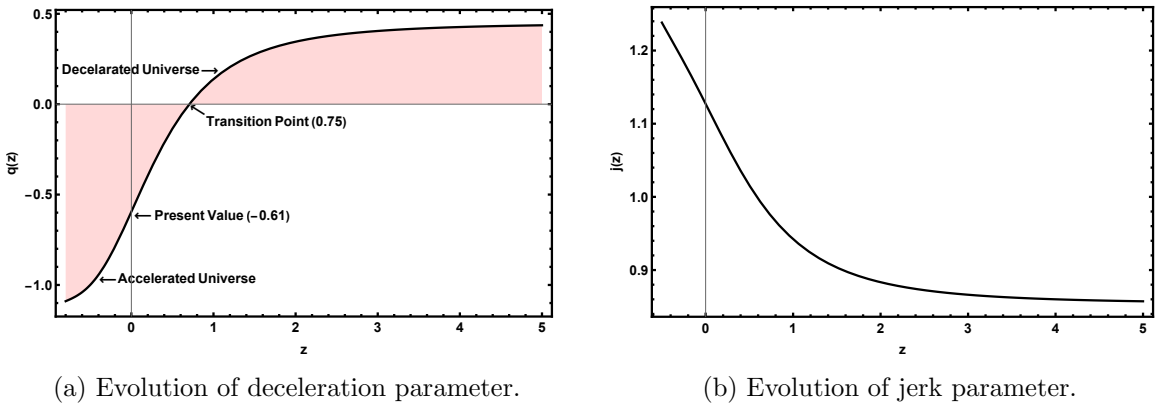


FIGURE 3.5: Evolution of cosmographic parameters as a function of redshift.

The transition of the deceleration parameter from early deceleration to late-time acceleration is illustrated in Fig. 3.5a. This transition occurs at approximately $z_t \approx 0.75$, indicating a shift from a decelerating phase to an accelerating phase with the present value of the deceleration parameter being $q_0 \approx -0.61$. Recently performed measurements have determined that the value of the deceleration parameter for the current cosmic epoch is within the range of $q_0 = -0.528^{+0.092}_{-0.088}$ [201] and transition from deceleration to acceleration at $z_t = 0.60^{+0.21}_{-0.12}$ [80, 202]. From Fig. 3.5b, we can observe that $j > 0$, which verify that there exists a transition time when the Universe modifies its expansion.

The next step is to test the validity of the model using observational tools like the $Om(z)$ diagnostic and the age of the Universe.

3.6 Test for the validation

It is possible to verify the validity of any cosmological model through some theoretical and observational tests. For this discussion, we examine the $Om(z)$ cosmological test as a possible way to authenticate our derived model. To validate the model, we calculated the age of the Universe.

3.6.1 $Om(z)$ diagnostic

The $Om(z)$ diagnostic has been introduced as an alternative approach to test the accelerated expansion of the Universe with the phenomenological assumption, EoS, $p = \rho\omega$ filling the Universe with the perfect fluid. The $Om(z)$ diagnostic provides a null test to the Λ CDM model [203]. Also, there are evidences available in the literature on its sensitiveness with the EoS parameter [204–206]. The nature of $Om(z)$ slope differs between dark energy models because: the positive slope indicates the phantom phase $\omega < -1$ and the negative slope indicates the quintessence region $\omega > -1$. The $Om(z)$ diagnostic can be defined as,

$$Om(z) = \frac{E^2(z) - 1}{(1+z)^3 - 1},$$

$$Om(z) = \frac{\left(\frac{\alpha}{\beta 6^n(2n-1)} + (z+1)^3 \left(-\frac{\alpha}{\beta 6^n(2n-1)} - \frac{1}{\beta 6^n(2n-1)} + 1\right) + \frac{(z+1)^{3(\omega+1)}}{\beta 6^n(2n-1)}\right)^{1/n} - 1}{(z+1)^3 - 1}. \quad (3.13)$$

In Fig. 3.6a, $Om(z)$ shows the positive behavior and that confirms the phantom like behavior of model.

3.6.2 Age of the Universe

The age-redshift relationship determining the age of the Universe as a function of redshift, $t_U(z)$ is given by [207],

$$t_U(z) = \int_z^\infty \frac{d\tilde{z}}{(1+\tilde{z})H(\tilde{z})}. \quad (3.14)$$

The age of the Universe at any redshift is inversely proportional to $H_0 = H(z=0)$ as shown in Eq. (3.14). Now, Using Eq. (3.5) the age of the Universe can be computed as,

$$H_0(t - t_0) = \int_0^z \frac{d\tilde{z}}{(1+\tilde{z})E(\tilde{z})},$$

$$H_0 t_0 = \lim_{z \rightarrow \infty} \int_0^z \frac{d\tilde{z}}{(1+\tilde{z})E(\tilde{z})}. \quad (3.15)$$

The Fig. 3.6b shows the behavior of time with redshift. It is found that $H_0(t_0 - t)$ converges to 0.9791 as $z \rightarrow \infty$. Utilizing this, we can calculate the current age of the Universe as

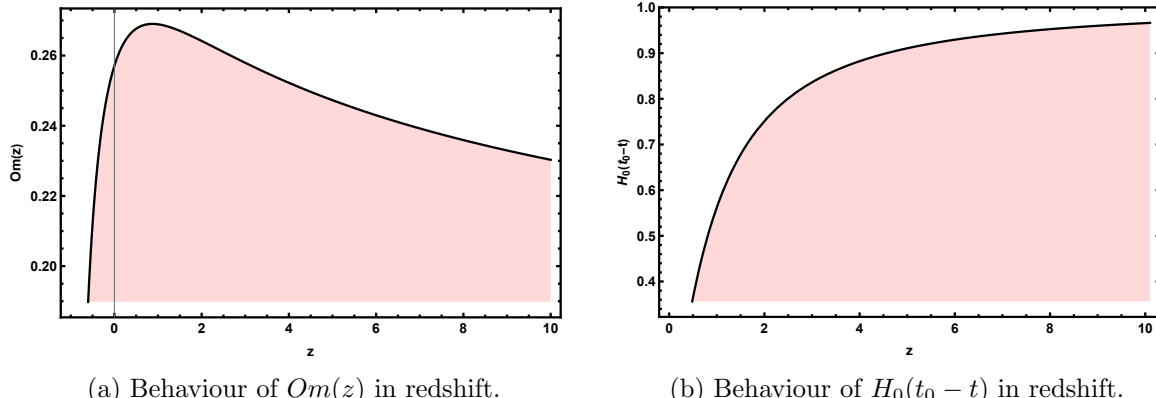


FIGURE 3.6: Graphical representation of the test validation of the behavior of the model.

$t_0 = 0.9791H_0^{-1} \approx 13.85$ Gyrs which is quite close to the age calculated from the Planck result $t_0 = 13.78 \pm 0.020$ Gyrs. So, the results obtained in the model are in consistent with current data.

3.7 Conclusion

In this chapter, we explored cosmological models by considering higher powers of non-metricity in the function $f(Q)$ and derived the expression for the Hubble parameter as a function of redshift. The $H(z)$ parameter was then constrained using the Hubble and the Pantheon+SH0ES datasets. We rebuild $H(z)$ and the distance modulus over 32 data points within the redshift range $0.07 \leq z \leq 1.965$ using a χ^2 minimization technique. Further analysis of the Pantheon+SH0ES data, consisting of 1701 SNe Ia apparent magnitude measurements, was conducted to obtain the best-fit values of model parameters and the EoS parameter through MCMC analysis. The results align well with the Λ CDM model, as shown by the error bar plots and the obtained parameter values listed in Table 3.1. Using the BAO dataset, we have validated our results. We further constrained the expansion history $H(z)$ and the $Om(z)$ diagnostic analysis provided a null test for the Λ CDM model. The transition from deceleration to acceleration occurred at a redshift of approximately $z_t \approx 0.75$, with a deceleration parameter $q_0 \approx -0.61$. The EoS parameter values derived from the Hubble and Pantheon+SH0ES datasets, -1.16 ± 0.17 and -1.15 ± 0.17 respectively suggest phantom behavior. Additionally, the age of the Universe was calculated based on the constrained Hubble parameter. Our models were compared with the concordance Λ CDM model through the cosmographic and $Om(z)$ parameters. The deviation from the Λ CDM model may indicate potential interactions between dark energy and dark matter, with our models favoring a phantom phase at this epoch.

Chapter 4

Insights into $f(Q)$ gravity: Modeling through the deceleration parameter

* The work, in this chapter, is covered by the following publication:

S. A. Narawade and B. Mishra, “Insights into $f(Q)$ gravity: Modeling through the deceleration parameter”, *J. High Energy Astrop.* **45** (2025) 409.

4.1 Introduction

Building on the analysis of the $f(Q)$ model in comparison to observational datasets discussed in the previous chapter, we now explore into alternative cosmological frameworks via reconstruction method. This approach aims to enhance our understanding of the late-time acceleration of the Universe. By incorporating the reconstruction method, observational data can be directly integrated into cosmological models, enhancing our understanding of the Universe and improving the accuracy of future surveys. One of the key advantages of reconstruction is that it is independent of the specific gravity model used in cosmological studies. In this approach, two methods are used: the parametric reconstruction, which establishes a kinematic model with free parameters and constrains the parameters through statistical analysis of observational data. The second one is non-parametric reconstruction, which derives models directly from observational data by using statistical procedures. Various cosmological parameters, such as the Hubble parameter [191, 208], the deceleration parameter [209, 210] and the jerk parameter [184, 211] have proven to be effective in exploring the accelerating Universe with parametric reconstruction. The parametrization of dynamical parameters such as pressure, energy density and EoS [58, 212] has been widely studied.

In this chapter, we began with the investigating the reconstruction of the deceleration parameter through the parametrization. Then the free parameters of the parameterized $q(z)$ are constrained using the observational datasets. Further, we have consider parametrized $H(z)$ obtained from $q(z)$ to reconstruct the $f(Q)$ models by applying the numerical approach with appropriate boundary conditions. Also, the statistical comparisons using AIC and BIC reveal a competitive performance with the Λ CDM model, positioning these $f(Q)$ models as promising alternatives for explaining DE and cosmic acceleration. This chapter aims to find viable alternatives to the standard Λ CDM model through the reconstruction of the deceleration parameter. It is therefore possible to replace the Λ CDM model effectively by reconstructing the $f(Q)$ gravity model using the deceleration parameter, providing an alternative explanation to the accelerating expansion of the Universe that does not rely on the cosmological constant. The chapter is organized as follows: The reconstruction of deceleration parameter are presented in section 4.2. The cosmological datasets are given in section 4.3. Our primary findings are presented in section 4.4, where we constrain the free parameters of both models based on the datasets. This section also features the reconstruction of the $f(Q)$ model, utilizing two forms of the deceleration parameter. Furthermore, we provide a comparative analysis of our results against the standard model of cosmology, employing the AIC and the BIC for evaluation. Finally, we summarize our main results in section 4.5.

4.2 Reconstruction of $q(z)$

By combining the Taylor series for $a(t)$ given in Eq. (1.32) and the scale factor-redshift relation provided in Eq. (1.14), we can rewrite Eq. (1.33) as,

$$q(z) \equiv \frac{1}{2} \frac{(1+z)}{H(z)^2} \frac{d}{dz} (H(z)^2) - 1 , \quad (4.1)$$

$$j(z) \equiv - \left[\frac{1}{2} \frac{(1+z)^2}{H(z)^2} \frac{d^2}{dz^2} (H(z)^2) - \frac{(1+z)}{H(z)^2} \frac{d}{dz} (H(z)^2) + 1 \right] . \quad (4.2)$$

It is obvious that Eq. (4.1) lead to a homogeneous Euler equation when $q = \text{constant}$. Under this assumption, Eq. (4.1) can be solved as,

$$E^2(z) = \frac{H^2(z)}{H_0^2} = C_1(1+z)^{2(1+\nu)} , \quad (4.3)$$

where C_1 is an arbitrary constant and H_0 stands for the current value of a Hubble parameter. A definition of the $E(z) = \frac{H(z)}{H_0}$ can then be used to replace $E(z)$ in Eq. (4.1). The constants in Eq. (4.1) and $H(z)$ can be determined without any fundamental change. In order to understand the physical meanings of the constants in Eq. (4.3), one can refer to a particular cosmological model. From Eq. (4.3), it is clear that if $q = \frac{1}{2}$, the above expression reduces to the Einstein-de Sitter solution, which is represented by [213],

$$E(z) = \left[C_1(1+z)^3 \right]^{\frac{1}{2}} . \quad (4.4)$$

This solution describes a matter-dominated Universe with no cosmological constant, where the expansion rate is solely determined by the matter content. It is clear that C_1 becomes the matter density term Ω_{m_0} . By evaluating deviation of $q(z)$ from $\frac{1}{2}$ or some other value in the past, we are able to determine how far it has strayed, but the calculation depends on the functional form of $q(z)$. The proposed reconstruction of deceleration parameter could be similar to the methods for studying the interaction between DE and DM based on phenomenological models [214], one possible proposal in reconstructing deceleration parameter is

$$q(z) = \frac{1}{2} + b \frac{g(z)}{E^2(z)} , \quad (4.5)$$

where b is constant and needs to be constrained and $g(z)$ is an arbitrary function of redshift z . The different choice of $g(z)$ will lead to different reconstructions of $q(z)$. It is possible to solve Eq. (4.1) analytically under certain models of $g(z)$ with this kind of assumption. As a result, Eq. (4.1) becomes more symmetric by satisfying both sides of the equation which are composed of a constant term and a E^{-2} term.

Using this method, we phenomenologically parameterize the $q(z)$ and solve the Euler equation. The first parametrization $f(z) = (1+z)^n$ simplifies modeling the dependence of the Hubble parameter on redshift. For $n = 4$, it represents the radiation-dominated era, while $n = 0$

corresponds to the standard Λ CDM model. Additionally, inspired by the reconstruction of the jerk parameter [211], we incorporate $f(z) = \ln(1 + z)$ as a secondary parametrization for our analysis.

- Model I
$$q(z) = \frac{1}{2} + b \frac{(1+z)^n}{E^2(z)}, \quad (4.6)$$

- Model II
$$q(z) = \frac{1}{2} + b \frac{\ln(1+z)}{E^2(z)}. \quad (4.7)$$

Substituting these equations into Eq. (4.1), we can obtain the solutions of $E(z)$,

- Power-law
$$E^2(z) = C_1(1+z)^3 + \frac{2b(1+z)^n}{n-3}, \quad (4.8)$$

- Logarithmic
$$E^2(z) = C_1(1+z)^3 - \frac{2b}{9} \left[1 + 3 \ln(1+z) \right]. \quad (4.9)$$

The coefficients C_1 and b arise from the process of solving Eq. (4.1) which is a first order differential equation. Another constraint that $E(z=0) = 1$ gives a relationship between the constants C_1 and b

- Power-law
$$C_1 = 1 - \frac{2b}{n-3},$$
- Logarithmic
$$C_1 = 1 + \frac{2b}{9}.$$

In the next section, the observational data has been explain to constrain the free parameters for each of the model listed above.

4.3 Observational datasets

The model and cosmological parameters are constrained using the MCMC sampler by exploring the posteriors of the parameter space and varying them across a wide range of conservative priors discussed in section 3.3.3. The MCMC analysis below will utilize OHD, SNe Ia and BAO as our baseline dataset. With different combinations of observational datasets, we test the free parameter for the Hubble parameter derived from the deceleration parameter. We have used the *emcee* package, which is available at Ref. [113], to perform an MCMC analysis of every model and dataset combination.

4.3.1 Hubble dataset

The differential age method is widely used to estimate the expansion rate of the Universe at redshift z . The Hubble parameter can then be predicted using $(1+z)H(z) = -\frac{dz}{dt}$. The dataset includes 32 measurements of the Hubble parameter, spanning a redshift range of $0.07 \leq z \leq 1.965$ [124]. The mean value of the parameters is determined by minimizing the chi-square value given in section 3.3.1.

4.3.2 Type Ia Supernovae compilation

We used SNe Ia data as a baseline for MCMC analyses, with the chi-square formula outlined in section 3.3.2. Our analysis uses two SNe Ia datasets: Pantheon [215] and Pantheon⁺ [136], with the latter being an updated version of Pantheon (see 1.6.2).

4.3.3 BAO dataset

In this work, we have extended the BAO dataset by incorporating additional measurements from various surveys, including the BOSS DR11 quasar Lyman-alpha measurements at $z_{\text{eff}} = 2.4$ [216], the SDSS Main Galaxy Sample at $z_{\text{eff}} = 0.15$ [217] and the six-degree Field Galaxy Survey at $z_{\text{eff}} = 0.106$ [199]. Furthermore, the $H(z)$ values and the angular diameter distances from the SDSS-IV eBOSS DR14 quasar survey at $z_{\text{eff}} = \{0.98, 1.23, 1.52, 1.94\}$ [218] have been included. Also, the consensus BAO measurements for the Hubble parameter and comoving angular diameter distances from the SDSS-III BOSS DR12 at $z_{\text{eff}} = \{0.38, 0.51, 0.61\}$ [149] and the full covariance matrix associated with these two BAO datasets are taken into account. This extended dataset allows for a more comprehensive analysis, refining our cosmological constraints with the inclusion of measurements across a wider range of redshifts. By combining these new BAO data points, we enhance the precision of the constraints derived in section 3.4.

The corresponding combination of parameter, utilizing the reported BAO results given by [219],

$$\mathcal{G}(z_i) = \left(\frac{D_V(z_i)}{r_s(z_d)} \right) \left(\frac{r_s(z_d)}{D_V(z_i)} \right) D_H(z_i) \left(\frac{r_{s,\text{fid}}(z_d)}{r_s(z_d)} D_M(z_i) \right) \left(\frac{r_s(z_d)}{r_{s,\text{fid}}(z_d)} H(z_i) \right) \left(\frac{r_{s,\text{fid}}(z_d)}{r_s(z_d)} D_A(z_i) \right) ,$$

where, the angular diameter distance is $D_A(z) = (1+z)^{-2} D_L(z)$, the volume-average distance is $D_V(z) = \left[(1+z)^2 D_A(z)^2 \frac{cz}{H(z)} \right]^{1/3}$, the comoving angular diameter distance is given by $D_M(z) = (1+z) D_A(z)$, the Hubble distance is $D_H(z) = \frac{c}{H(z)}$ and the comoving sound horizon at the end of the baryon drag epoch at redshift $z_d \approx 1059.94$ [40] is calculated as,

$$r_s(z) = \int_z^\infty \frac{c_s(\tilde{z})}{H(\tilde{z})} dz = \frac{1}{\sqrt{3}} \int_0^{1/(1+z)} \frac{da}{a^2 H(a) \sqrt{1 + [3\Omega_{b,0}/(4\Omega_{\gamma,0})]a}} ,$$

where, we use the values $T_0 = 2.7255 \text{ K}$ [220], $\Omega_{b,0} = 0.02242$ [40] and a fiducial value of $r_{s,\text{fid}}(z_d) = 147.78 \text{ Mpc}$.

The chi-square for the BAO data (χ^2_{BAO}) is determined by,

$$\chi^2_{\text{BAO}}(\Theta) = \Delta G(z_i, \Theta)^T C_{\text{BAO}}^{-1} \Delta G(z_i, \Theta) , \quad (4.10)$$

where C_{BAO} is the covariance matrix of all the considered BAO observations and $\Delta G(z_i, \Theta) = G(z_i, \Theta) - G_{\text{obs}}(z_i)$.

These observational datasets offer essential constraints on the proposed Hubble function, providing valuable insights into their viability. In the next section, we will investigate the impact of

these datasets on free parameter of the Hubble function and analyzing how these constrained free parameter of the Hubble parameter affect the $f(Q)$ models and refines the cosmological understanding.

4.4 Impact on $f(Q)$ models

By considering the first Friedman equation (1.65), we can reconstruct the $f(Q)$ function. Based on Q , the derivatives of the non-metricity tensor can be expressed as derivatives of the Hubble parameter with respect to redshift. One can find

$$f_Q = \frac{f'(z)}{12H(z)H'(z)} ,$$

where the prime denote derivative with respect to z . Now, the Eq. (1.65) can be re-written as,

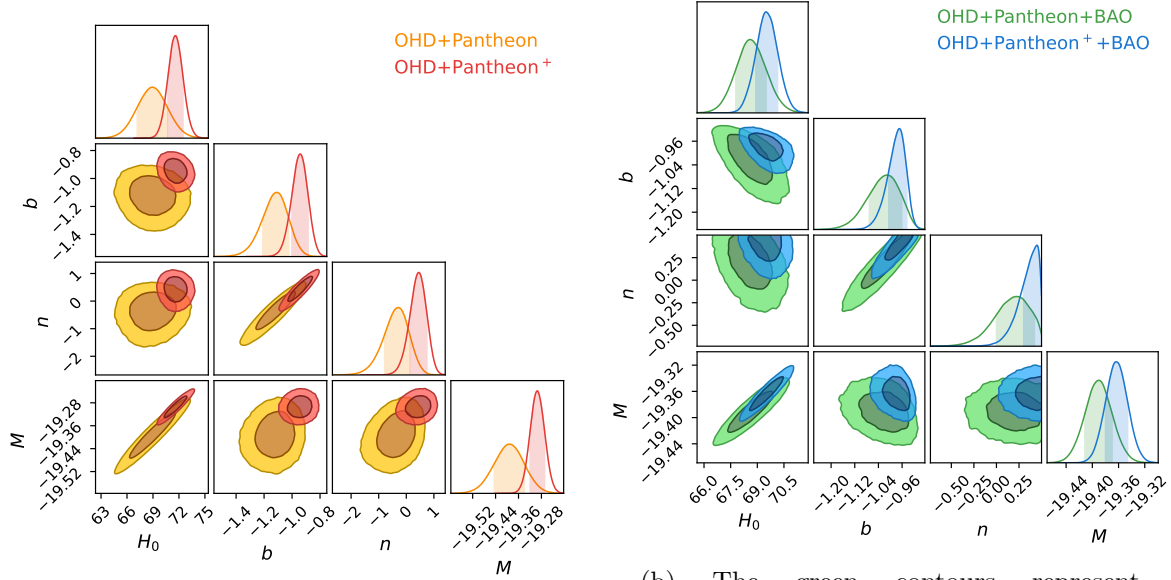
$$\frac{H'(z)}{H(z)} f'(z) - f(z) = 6H_0^2 \Omega_{m0} (1+z)^3 . \quad (4.11)$$

Based on Eq. (4.8) - (4.9) for both models and the results in Table 4.1 - 4.2 for each model, we can solve Eq. (4.11) numerically. To establish a boundary condition, we define the effective gravitational constant in $f(Q)$ gravity as $G_{eff} \equiv \frac{G}{f_Q}$ [221]. A natural requirement is that G_{eff} coincident with Newton's constant at the present epoch, which implies that $f_Q = 1$ when $z = 0$. Incorporating this condition into Eq. (1.65) yields the following initial condition $f_0 = 6H_0^2 (2 - \Omega_{m0})$ [186].

4.4.1 Power-law function

The constraints on the free parameters for the power-law model has been displayed in Fig. 4.1. The figure 4.1a shows the posteriors as well as the confidence areas for various combination of OHD and SNe Ia datasets. It is clear from a deeper look at the posteriors that the parameters from the dataset combinations containing Pantheon⁺ show tighter constraints, with the H_0 parameter demonstrating substantially improved precision. However, the contour plots for the OHD+Pantheon and OHD+Pantheon⁺ dataset display a degeneracy between the H_0 , b and n . Notably, the OHD+Pantheon⁺ dataset combination exhibits a degeneracy between H_0 and the Ω_{m0} parameter.

In Fig. 4.1b the contour plots for the combination of OHD, SNe Ia and BAO datasets are displayed. In the analysis of the OHD+Pantheon+BAO dataset combination, we observe that the constraints on the H_0 , b and n parameters are more precise compared to those derived from the OHD+Pantheon dataset alone. The addition of BAO data helps break the degeneracy between these parameters, resulting in more robust constraints and tighter bounds on the Ω_{m0} parameter. Also, the OHD+Pantheon⁺+BAO combination yields even more precise constraints, with excellent precision on H_0 while significantly minimizing the degeneracy between H_0 , b



(a) The yellow contours represent dataset combinations that include OHD+Pantheon, while the red contours show combinations that include the OHD+Pantheon⁺ datasets.

(b) The green contours represent dataset combinations that include OHD+Pantheon+BAO, while the blue contours show combinations that include the OHD+Pantheon^{++BAO} datasets.

FIGURE 4.1: Confidence contours and posteriors for the parameters H_0 , b and n of the power-law function.

and n . As a result, the uncertainty associated with Ω_{m_0} is significantly reduced, making this combination the most precise across all parameters in the power-law model.

Dataset	H_0	b	n	Ω_{m_0}	M
OHD + Pantheon	$68.90^{+1.80}_{-1.70}$	$-1.108^{+0.085}_{-0.101}$	$-0.28^{+0.41}_{-0.50}$	$0.324^{+0.036}_{-0.037}$	$-19.391^{+0.051}_{-0.053}$
OHD + Pantheon ⁺	$71.62^{+0.84}_{-0.89}$	$-0.941^{+0.055}_{-0.060}$	$0.46^{+0.29}_{-0.31}$	$0.26^{+0.05}_{-0.04}$	-19.294 ± 0.025
OHD + Pantheon+BAO	$68.59^{+0.90}_{-0.80}$	$-1.012^{+0.051}_{-0.059}$	$0.22^{+0.20}_{-0.22}$	$0.28^{+0.02}_{-0.03}$	-19.391 ± 0.021
OHD + Pantheon ^{++BAO}	$69.47^{+0.67}_{-0.55}$	$-0.969^{+0.025}_{-0.036}$	$0.46^{+0.04}_{-0.16}$	$0.25^{+0.02}_{-0.01}$	-19.365 ± 0.020

TABLE 4.1: Constrained values of free parameters based on the different combinations of OHD, SNe Ia and BAO datasets for the power-law function.

Table 4.1 displays the precise values for the cosmological and model parameters for power-law model, including the nuisance parameter M . For dataset combinations that contain Pantheon⁺, we found that the H_0 values are comparatively greater than the corresponding H_0 values that contain Pantheon data. According to the SH0ES team, $H_0 = 73.30 \pm 1.04 \text{ km s}^{-1} \text{Mpc}^{-1}$ [138] and $H_0 = 73.24 \pm 1.74 \text{ km s}^{-1} \text{Mpc}^{-1}$ [164], which is in accordance with the high value of H_0 . The OHD+Pantheon⁺ yielded the highest values of H_0 as, $H_0 = 71.62^{+0.84}_{-0.89} \text{ km s}^{-1} \text{Mpc}^{-1}$. The Ω_{m_0} parameter interestingly reaches a minimal value in this scenario, suggesting that the majority of the energy of the Universe appears as an effective dark energy, consistent with the high value of H_0 . For the dataset OHD + Pantheon + BAO and OHD + Pantheon^{++BAO}, the

constrained value of H_0 are marginally lower than those derived from the OHD + Pantheon and OHD + Pantheon⁺ combination. Specifically, the OHD + Pantheon + BAO dataset yields $H_0 = 68.59_{-0.80}^{+0.90} \text{ km s}^{-1} \text{ Mpc}^{-1}$, whereas the OHD + Pantheon⁺ + BAO configuration leads to $H_0 = 69.47_{-0.55}^{+0.67} \text{ km s}^{-1} \text{ Mpc}^{-1}$. Although these values are still in the high range compared to the CMB, which is approximately $67.4 \pm 0.5 \text{ km s}^{-1} \text{ Mpc}^{-1}$ based on Planck data [40], the inclusion of the BAO data imposes tighter constraints on the cosmological parameters, resulting in a slight reduction in the H_0 estimates. Additionally, the Ω_{m_0} parameter, while still on the lower end in both scenarios, shows a modest increase compared to the Pantheon⁺ analysis. This indicates that dark energy continues to be the dominant component of the Universe, while the inclusion of BAO data suggests a somewhat enhanced matter density contribution.

Using the Eq. (4.8) we can find

$$\frac{1}{H(z)} \frac{d}{dz} [H(z)] = \frac{3(1+z)^3(2b-n+3) - 2bn(1+z)^n}{2(2b(1+z)^n + (1+z)^3(-2b+n-3))}. \quad (4.12)$$

We determine $z(Q)$ by using Eq. (4.8) to invert $Q = 6H^2$. The function $f(Q)$ is obtained by re-inserting $z(Q)$ into $f(z)$. Therefore, we find that the numerical solution is suitable for the function as,

$$f(Q) = Q + \alpha Q e^{\beta \frac{Q}{Q_0}}, \quad (4.13)$$

for the set of constant coefficients $(\alpha, \beta) = (2.460, 0.191)$. We display our results in Fig. 4.2.

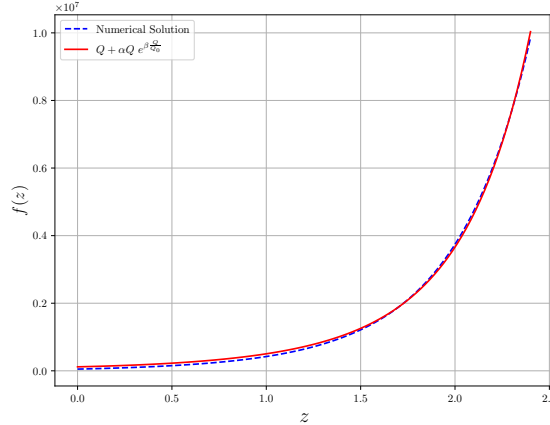


FIGURE 4.2: Reconstruction of $f(Q)$ model for power-law function. The best analytical matching (solid red) to the numerical solution (dashed blue).

We note that the test function given in Eq. (4.13) recovers pure GR for $\alpha = 0$ and $\beta = 0$. This reconstructed model has GR as a particular limit, it has the same number of free parameters as Λ CDM, but in a cosmological context it creates a scenario that does not have Λ CDM as a limit [88].

4.4.2 Logarithmic function

Here, we have analyzed the observational constraints for logarithmic model given in Eq. (4.9). The confidence levels and the posterior of the constrained parameters are shown in Fig. 4.3. The red contours show the combinations that consist of the OHD+Pantheon⁺ samples, while the orange contours show the dataset combinations that include the OHD+Pantheon sample [Fig. 4.3a]. The precise numerical values of the parameters, including the nuisance parameter M , shown in Fig. 4.3 are presented in Table 4.2. These results indicate that the estimated H_0 values are comparable to those found in the power-law model. However, the inferred values of the matter density parameter Ω_{m_0} are somewhat lower than those of the power-law model since the logarithmic model is especially made to forecast an accelerating Universe at the late-time regime. In this case, the data constraints support a lower matter density to be consistent with the observed acceleration, while the model parameters allow for a more flexible description of the Universe.

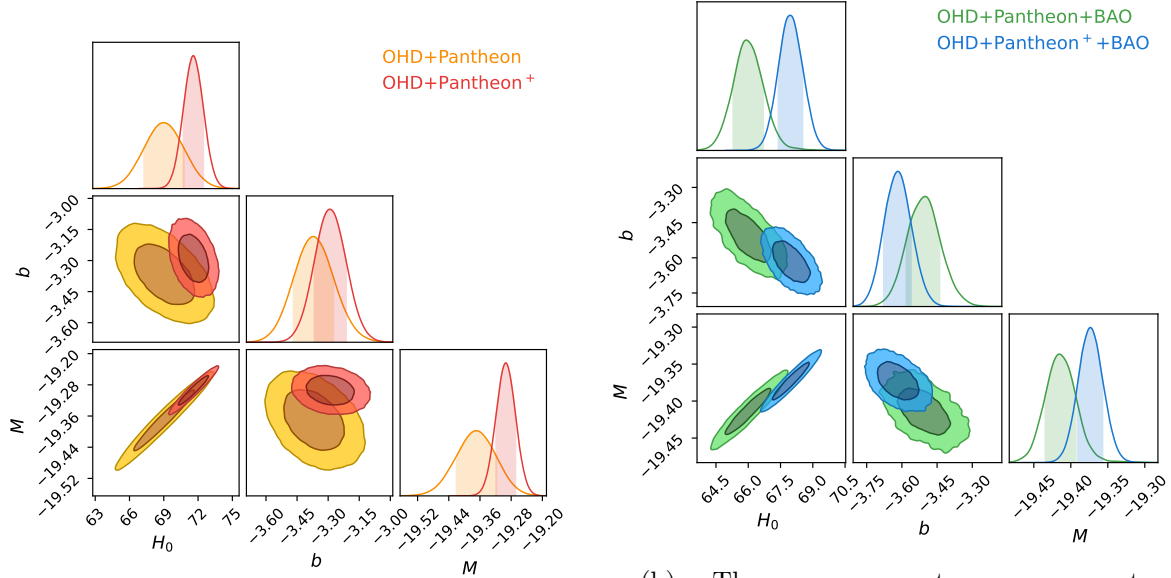
Figure 4.3b displays the contour plots for the OHD+Pantheon and OHD+Pantheon⁺ datasets, with the addition of BAO data. The inclusion of BAO data into the OHD+Pantheon and OHD+Pantheon⁺ datasets offers additional constraints on the model parameters, resulting in minor adjustments to the estimated values. Specifically, for both dataset scenarios, the incorporation of BAO leads to a reduction in the estimated Hubble constant H_0 , compared to analyses that exclude BAO. While the matter density parameter Ω_{m_0} remains nearly unchanged, but the BAO data helps refine the constraints on the other parameters, including the nuisance parameter. Overall, incorporating the BAO data enhances the precision of parameter estimates, thereby improving the capacity of the model to describe the late-time dynamics of the Universe. The BAO data incorporation yields the lowest value of Ω_{m_0} as $\Omega_{m_0} = 0.24$.

Dataset	H_0	b	Ω_{m_0}	M
OHD + Pantheon	$69.00^{+1.80}_{-1.70}$	$-3.372^{+0.098}_{-0.095}$	0.25 ± 0.02	$-19.367^{+0.049}_{-0.053}$
OHD + Pantheon ⁺	$71.57^{+0.90}_{-0.85}$	$-3.293^{+0.080}_{-0.073}$	0.27 ± 0.02	-19.294 ± 0.025
OHD + Pantheon+BAO	$65.88^{+0.82}_{-0.58}$	$-3.500^{+0.061}_{-0.081}$	$0.24^{+0.01}_{-0.02}$	-19.416 ± 0.020
OHD + Pantheon ⁺ +BAO	$67.98^{+0.55}_{-0.58}$	$-3.617^{+0.056}_{-0.060}$	$0.23^{+0.02}_{-0.02}$	-19.374 ± 0.017

TABLE 4.2: Constrained values of free parameters based on the different combinations of OHD, SNe Ia and BAO datasets for the logarithmic function.

We have reconstructed the $f(Q)$ for logarithmic function in a similar manner as power-law function. Subsequently, we obtain the most suitable $f(Q)$ function as,

$$f(Q) = \alpha_1 Q + \alpha_2 Q^2 + \alpha_3 Q^3 + \alpha_4 \log\left(\frac{Q}{Q_0}\right), \quad (4.14)$$



(a) The yellow contours represent dataset combinations that include OHD+Pantheon, while the red contours show combinations that include the OHD+Pantheon⁺ datasets.

(b) The green contours represent dataset combinations that include OHD+Pantheon+BAO, while the blue contours show combinations that include the OHD+Pantheon⁺+BAO datasets.

FIGURE 4.3: Confidence contours and posteriors for the parameters H_0 and b of the logarithmic function.

with the values of coefficients, $(\alpha_1, \alpha_2, \alpha_3, \alpha_4) = (1.196, -2.22 \times 10^{-5}, 2.03 \times 10^{-10}, 1.24 \times 10^5)$. The results are shown in Fig. 4.4. We note that the test function [Eq. (4.14)] returns to GR when $(\alpha_1, \alpha_2, \alpha_3, \alpha_4) = (1, 0, 0, 0)$. The Eq. (4.14) is presented as a novel approach

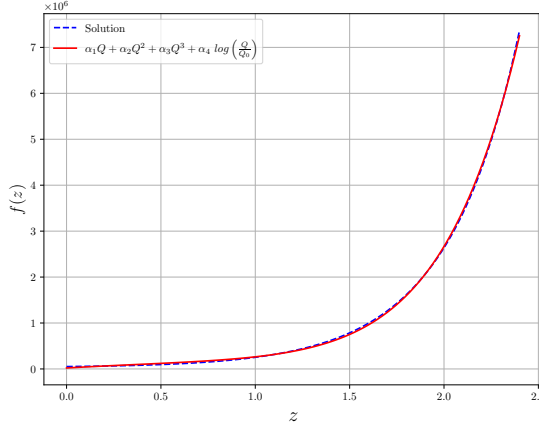


FIGURE 4.4: Reconstruction of $f(Q)$ model for logarithmic function. The best analytical match (solid red) to the numerical solution (dashed blue).

for describing cosmic evolution, particularly focusing on avoiding early-time instabilities and phantom behaviors. In this model, the effective EoS parameter remains strictly non-phantom. As shown in [222], it can be combined with an exponential and cross the phantom divide. Notably, this model passes the Big Bang Nucleosynthesis constraints trivially, meaning it does not interfere

with the delicate balance required for early Universe nucleosynthesis, making it a stable and potentially viable model for both early and late Universe dynamics [172].

The logarithmic model, offering a more flexible description of late-time acceleration and a lower matter density, serves as an alternative to the power-law function. In the next section, we will conduct a detailed comparison of both models, evaluating their cosmological implications and how well they fit the available observational data.

4.4.3 Model comparison

We assess the performance of each model and dataset by calculating its minimal χ^2_{\min} values, which are derived from the maximum likelihood L_{\max} since $\chi^2_{\min} = -2 \ln L_{\max}$. Additionally, we use the Akaike Information Criteria (AIC), a measure of the goodness of fit and the complexity of the model based on the number of parameters n , to compare these models with the typical Λ CDM. The AIC is defined as [223],

$$\text{AIC} = \chi^2_{\min} + 2n. \quad (4.15)$$

When the AIC value is lower, the model fits the data more effectively while taking its complexity into account. Models with more parameters are penalized by the AIC, even if they improve the fit. This means that, provided the difference is significant, a model with a lower AIC is preferable to one with a higher value. As well as the AIC, we examine the Bayesian Information Criterion (BIC), which places a greater emphasis on model complexity than the AIC and is defined as [224],

$$\text{BIC} = \chi^2_{\min} + n \ln m, \quad (4.16)$$

where m is the sample size of the observational data combination.

We determine the differences in AIC and BIC relative to the Λ CDM model as a reference, in order to assess the performance of different models with different dataset combinations. $\Delta\text{AIC} = \Delta\chi^2_{\min} + 2\Delta n$ and $\Delta\text{BIC} = \Delta\chi^2_{\min} + \Delta n \ln m$, respectively represent the differences between AIC and BIC. Better performance is suggested by smaller ΔAIC and ΔBIC values, which show that the model utilizing the chosen dataset is more comparable to the Λ CDM model. The values for several statistical measures, including χ^2_{\min} , AIC, ΔAIC , BIC and ΔBIC , are presented in Table 4.3 - 4.4 for both models that incorporate various combinations of OHD, SNe Ia and BAO data.

Model	OHD + Pantheon					OHD+ Pantheon ⁺				
	χ^2_{\min}	AIC	ΔAIC	BIC	ΔBIC	χ^2_{\min}	AIC	ΔAIC	BIC	ΔBIC
ΛCDM	1041.16	1047.16	0	1050.63	0	1539.22	1545.22	0	1548.93	0
Model I	1040.76	1048.76	1.60	1052.90	2.27	1552.82	1560.82	15.60	1565.78	16.85
Model II	1043.90	1049.90	2.74	1053.00	2.37	1552.82	1558.82	13.60	1562.53	13.60

TABLE 4.3: The comparison of the models with the ΛCDM model for OHD+Pantheon and OHD+Pantheon⁺ datasets.

Model	OHD + Pantheon + BAO					OHD+ Pantheon ⁺ + BAO				
	χ^2_{\min}	AIC	ΔAIC	BIC	ΔBIC	χ^2_{\min}	AIC	ΔAIC	BIC	ΔBIC
ΛCDM	1046.40	1052.40	0	1056.13	0	1576.10	1582.10	0	1585.83	0
Model I	1045.26	1053.26	0.86	1057.42	1.29	1568.90	1576.90	-5.2	1581.03	-5.8
Model II	1063.31	1069.31	16.91	1073.03	16.90	1596.82	1602.82	20.72	1606.53	20.70

TABLE 4.4: The comparison of the models with the ΛCDM model for OHD+Pantheon+BAO and OHD+Pantheon⁺+BAO datasets.

Several studies have explored the reconstruction of the $f(Q)$ model. For instance, the numerical approximation of the $f(Q)$ model to a polynomial form using the luminosity distance and Páde approximation was conducted by [186]. Additionally, [225] examined various modified gravity models for reconstructing the $f(Q)$ function. In contrast, our approach utilizes a parametrized deceleration parameter for reconstructing the $f(Q)$ models, resulting in exponential and logarithmic approximations. Notably, the exponential model has been rigorously tested against observational data in [88], while the logarithmic model has been studied in the context of Big Bang Nucleosynthesis in [172].

4.5 Conclusion

In this chapter, we studied the impact of the deceleration parameter on the modified $f(Q)$ gravity models. An important step in cosmological analysis is reconstructing a parametric form for $q(z)$. To validate the parametrization and ensure its predictive capability across all redshift ranges, it is essential to approach the process with careful consideration of both observational constraints and theoretical frameworks. Consequently, robust investigations of the dynamics of the Universe are enabled and modified gravity theories can be explored. A new parametrization for the deceleration parameter has been presented in this chapter, providing a more flexible way of studying the dynamics of the Universe. As a result of the utilization of observational datasets

including OHD, SNe Ia and BAO, cosmological parameters were constrained and the proposed models were validated. With the use of Bayesian statistical inference techniques and MCMC methods, we were able to accurately analyze the data and draw meaningful conclusions from the analysis. Based on these fitting results, we analyze the kinematic behavior of the Universe. Our results demonstrate that the parameters of our models match the observational data well.

The model I, which follows a power-law formulation, demonstrates compatibility with the latest high values of H_0 , aligning with recent observational values and indicating a dark energy-dominated Universe. Moreover the reconstructed $f(Q)$ model has GR as a particular limit, it has the same number of free parameters as Λ CDM, but in a cosmological context it creates a scenario that does not have Λ CDM as a limit. Whereas, the model II, featuring a logarithmic term, aligns with a slightly reduced matter density and accurately models the accelerated expansion. The reconstructed $f(Q)$ function for model II is presented as a novel approach for describing cosmic evolution, particularly focusing on avoiding early-time instabilities and phantom behaviors. In this model, the effective equation of state parameter remains strictly non-phantom. Also, this model passes the Big Bang Nucleosynthesis constraints trivially, meaning it does not interfere with the delicate balance required for early Universe nucleosynthesis, making it a stable and potentially viable model for both early and late Universe dynamics. Finally the comparative analysis against Λ CDM using AIC and BIC metrics shows that these models provide competitive fits, with Model II offering a slight edge in simplicity. Thus, the reconstructed $f(Q)$ functions from deceleration parameter in the $f(Q)$ gravity presents a robust framework for addressing dark energy and cosmic acceleration.

Chapter 5

Stable $f(Q)$ gravity model through trivial and non-trivial connection

* The work, in this chapter, is covered by the following publications:

S. A. Narawade, Santosh V Lohakare and B. Mishra, “Stable $f(Q)$ gravity model through non-trivial connection”, *Annals Phys.* **474** (2025) 169913.

S. A. Narawade, S. H. Shekh, B. Mishra, Wompherdeiki Khyllep and Jibitesh Dutta, “Modelling the Accelerating Universe with $f(Q)$ Gravity: Observational Consistency”, *Eur. Phys. J. C*, **84**, 773 (2024).

5.1 Introduction

In symmetric teleparallel gravity, the choice of connection is crucial as it determines the nonmetricity scalar Q , this impacts the equations of motion and influences the cosmological dynamics. Various connections provide unique insights into the relationship between geometry and cosmic evolution. For example, Connection I corresponds to coincident gauge choices, ensures a more straightforward dynamic formulation. In contrast, Connection II and Connection III introduce more complex dynamical characteristics, allowing for a deeper investigation into cosmological phenomena. Recently, there has been considerable attention on $f(Q)$ gravity and its cosmological implications in several important studies, see [86–89, 110, 111, 226–231]. It is worth noting that all of these studies were conducted with coincident gauges and line elements in Cartesian coordinates. Due to this specific choice, the covariant derivative is reduced to a partial derivative, which simplifies the calculations. On the other hand, the pressure and energy equations are identical to the $f(T)$ theory. In cosmological context, whether in flat [232–234] or curved [235–238] Universe, the $f(Q)$ theory, which does not rely on coincident gauges, is garnering significant interest.

In the previous chapter, we analyzed the reconstruction of the gravity model $f(Q)$ with the help of the deceleration parameter within the framework of coincident gauge. Now, in this chapter, we explores the reconstruction of the $f(Q)$ gravity model using NEC within the framework of non-trivial connection. A covariant $f(Q)$ gravity within Connection-III [103] and FLRW metric is utilized to reconstruct the $f(Q)$ model. The dynamic behavior of two models, particularly model within coincident gauge and the reconstructed model are thoroughly studied using the Hubble parameter and various observational datasets for the comparative analysis. Also the energy conditions are analyzed, because of the fundamental causal structure of space-time, the gravitation attraction can be characterized by the energy conditions. Moreover, these boundary conditions play a significant role in shaping the cosmic evolution of the Universe. Furthermore, the stability of the model is achieved through the scalar perturbation. To explore the potential impact of nonmetricity on the evolution of the Universe, we constructed an $f(Q)$ model that incorporates nontrivial connections. By comparing this model to the Λ CDM paradigm, the goal is to assess the role of nonmetricity in cosmic dynamics. The structure of the chapter is as follows: In section 5.2, we applying specific conditions along with connection-III, we reconstruct the $f(Q)$ model. The section 5.3 discusses the Hubble parameter, along with the observational datasets and the results for parameter constrains. The dynamical behaviour of the two models, particularly model within coincident gauge and model reconstructed through non-coincident gauge are studied for the comparative analysis in section 5.4 and also the stability of the model reconstructed through non-coincident gauge has been studied using scalar perturbation. We conclude with a general discussion of our results in section 5.5.

5.2 Reconstruction of the $f(Q)$ model

The Connection I corresponds to coincident gauge choices, it simplifies the dynamical formulation. While Connection II and Connection III share a similar structure, the function γ which acts as an additional degree of freedom, behaves differently in each case [239]. The $\frac{1}{a^2}$ factor in Connection III plays a crucial role by suppressing the contributions of γ and $\dot{\gamma}$ at late times, ensuring a smoother cosmological evolution and reducing the risk of sudden singularities compared to Connection II. This scaling enables a clear distinction between early and late-time dynamics, making the model more stable and better aligned with observational data. Thus we will focus on model within coincident gauge and Connection III in this chapter. By employing $\gamma = \gamma_1 a^2(t)$ [232], where γ_1 is arbitrary constant. We derive $Q = -6H^2 + 9\gamma_1 H$, which leads to $\dot{Q} = -12H\dot{H} + 9\gamma_1 \dot{H}$. Consequently, Eqs. (1.76) and (1.77) are transformed as,

$$\rho = \frac{f}{2} + 3H^2 f_Q - \frac{1}{2} Q f_Q - \frac{3\gamma_1}{2} \dot{Q} f_{QQ}, \quad (5.1)$$

$$p = -\frac{f}{2} - 3H^2 f_Q + \frac{1}{2} Q f_Q - 2\dot{H} f_Q + \frac{(\gamma_1 - 4H)}{2} \dot{Q} f_{QQ}. \quad (5.2)$$

$$(5.3)$$

From Eqs. (5.1) and (5.2), we derive the expression

$$\rho + p = \left(-\gamma_1 \dot{Q} f_{QQ} - 2\dot{H} f_Q - 2H\dot{Q} f_{QQ} \right). \quad (5.4)$$

By applying the chain rule to f_Q and considering the condition $p + \rho \rightarrow 0$, we obtain

$$\begin{aligned} -\frac{d}{dt}(\gamma_1 f_Q) &= \frac{d}{dt}(2H f_Q), \\ \frac{df}{dH} &= \frac{C(4H - 3\gamma_1)}{2H + \gamma_1}. \end{aligned}$$

Upon integrating both sides, we find

$$f(H) = 4H - 5\gamma_1 \ln(2H + \gamma_1).$$

By applying these results up to the 4th order and substituting the value of Q , we can reconstruct $f(Q)$ as,

$$f(Q) = \alpha_1 + \alpha_2 Q + \alpha_3 Q^2 + (\beta_1 + \beta_2 Q) \sqrt{81\gamma_1^2 - 24Q}. \quad (5.5)$$

The reconstruction of the $f(Q)$ model provides a theoretical framework to explore the underlying dynamics of the Universe. In the following section, we will analyze observational data to estimate the free parameters of the Hubble parameter.

5.3 Data analysis and parameter estimation

In this section, we analyze the behavior of the $f(Q)$ model by utilizing the functional form of the Hubble parameter given by $H(z)^2 = H_0^2 \left[A(1+z)^B + \sqrt{A^2(1+z)^{2B} + C} \right]$ [240]. We will conduct MCMC analysis using the *emcee* package described in section 3.3.3, to constrain the free parameters H_0 , A , B and C based on observational datasets. Our analysis will use Hubble data, Pantheon⁺ data and BAO data as the baseline discussed in the section 3.3 and 4.3.

The free parameters H_0 , A , B and C are constrained using the OHD, Pantheon⁺ and OHD + Pantheon⁺ + BAO datasets [Fig. 5.1] and are given in Table 5.1.

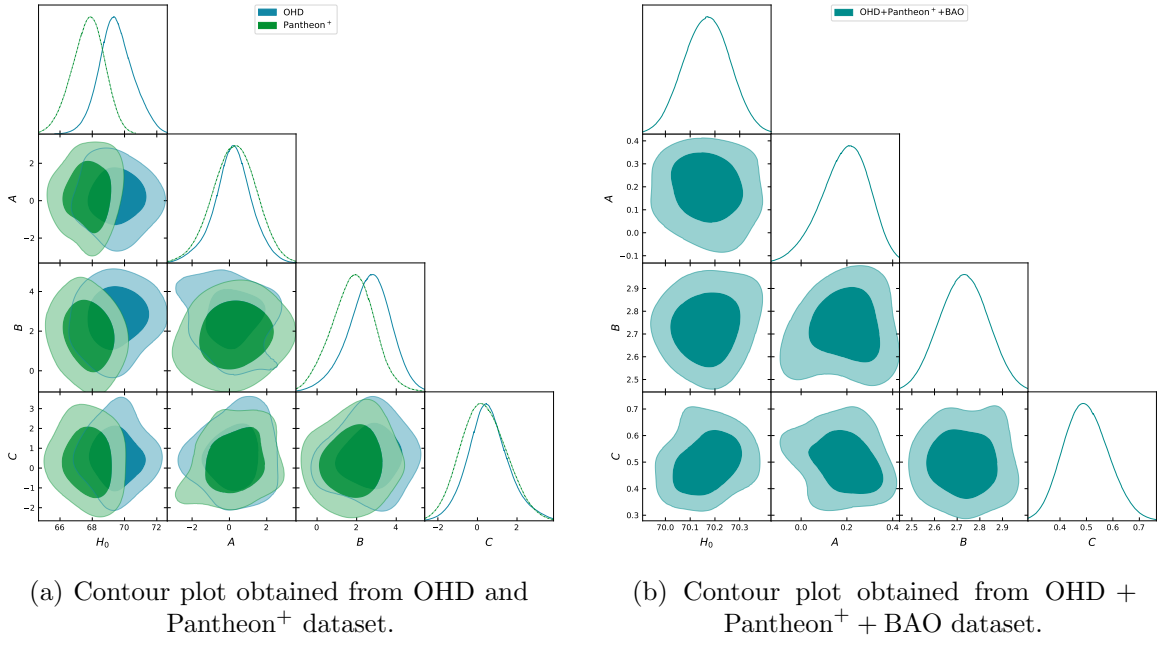


FIGURE 5.1: MCMC contour plot obtained from the observational datasets for 1σ and 2σ confidence interval.

Dataset	H_0	A	B	C
OHD	69.49 ± 1.10	0.19 ± 0.99	$2.66_{-0.97}^{+1.10}$	$0.55_{-1.10}^{+0.95}$
Pantheon ⁺	$69.5_{-1.80}^{+2.10}$	$0.20_{-2.20}^{+2.00}$	2.70 ± 2.10	$0.5_{-2.10}^{+2.20}$
OHD + Pantheon ⁺ + BAO	$70.16_{-0.90}^{+1.00}$	$0.19_{-0.13}^{+0.15}$	2.73 ± 0.10	$0.49_{-1.00}^{+0.08}$

TABLE 5.1: Best-fit values of parameter space using OHD, Pantheon⁺ and OHD + Pantheon⁺ + BAO dataset.

The estimated value of the Hubble constant H_0 from our analysis, using the OHD, Pantheon⁺ and the combined OHD+Pantheon⁺+BAO datasets are respectively 69.49 km/s/Mpc, 69.50 km/s/Mpc and 70.16 km/s/Mpc, are consistent with current local measurements, with a value around

70.4 ± 1.4 km/s/Mpc [192]. This result is in mild tension with the value inferred from the CMB, which is approximately 67.4 km/s/Mpc based on Planck data [40]. The slight variations observed in our estimates reflect the impact of different datasets and highlight the ongoing challenges in resolving the Hubble tension, a key issue in modern cosmology.

In this section, we have reconstructed the cosmological model within the $f(Q)$ gravity framework and constrained the free parameters for Hubble parameter using MCMC analysis using different observational datasets. These constrained parameters and the $H(z)$ will be utilized in the next section to study the dynamical aspects of this reconstructed model by analyzing the time evolution of energy density and the equation of state, along with testing stability under perturbations. This analysis is essential for understanding the physical validity and long-term behavior of the model, ensuring that the reconstructed model align with observational data and remain stable over cosmic evolution.

5.4 Comparative analysis

In this section, we will analyze the dynamic behaviour of two different cosmological models utilizing the constrained free parameters for $H(z)$ from the various observational datasets. The equation for \dot{H} is provided in the context of redshift z as,

$$\dot{H} = -\frac{1}{2}ABH_0^2(1+z)^B \left(1 + \frac{A(1+z)^B}{\sqrt{A^2(1+z)^{2B} + C}} \right). \quad (5.6)$$

5.4.1 Model within coincident gauge

To study the background evolution of the dynamical parameter, we consider a well-motivated form $f(Q)$ given by [106],

$$f(Q) = \frac{\alpha Q}{Q_0} + \frac{\beta Q_0}{Q}, \quad (5.7)$$

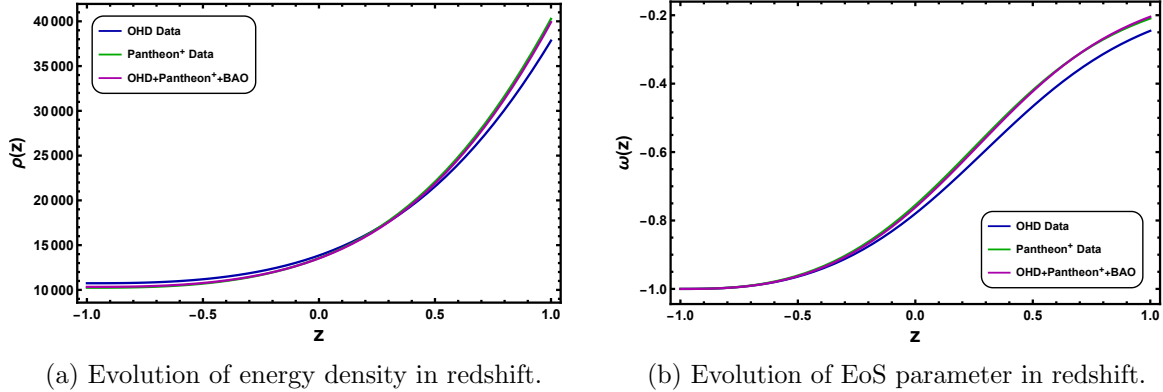
where $Q_0 = 6H_0^2$ (H_0 is present Hubble value). This form is useful in describing the late time acceleration without invoking the DE component [227]. Using the Hubble parameter and Eq. (5.7), Eqs. (1.65) - (1.66) can be written as,

$$\rho = H(z)^2 \left(3 - \frac{\alpha}{2H_0^2} \right) + \frac{3\beta H_0^2}{2H(z)^2} + (1+z)^3(\Omega_m + \Omega_r z + \Omega_r), \quad (5.8)$$

$$p = \frac{\alpha (3H(z)^6 + 2H(z)^4 H_z) + H_0^2 (-9\beta H(z)^2 H_0^2 + 6\beta H_0^2 H_z - 18H(z)^6 + 2H(z)^4 (\Omega_r(1+z)^4 - 6H_z))}{6H(z)^4 H_0^2}. \quad (5.9)$$

From Fig. 5.2, we can observe that the effect of the radiation term ρ_r reflects here and also the energy density decreases from early times to late times but does not vanish. The total EoS parameter yields present values of $\omega_0 \simeq -0.78$, $\omega_0 \simeq -0.77$ and $\omega_0 \simeq -0.76$ for

the constrained free parameters from the OHD dataset, Pantheon⁺ dataset and the combined OHD+Pantheon⁺+BAO dataset, respectively [Fig. 5.2b]. The energy density and EoS parameter are solely dependent on the values of the model coefficients, which govern the evolutionary behavior of the parameters. This model shows the quintessence behavior at present time [241].

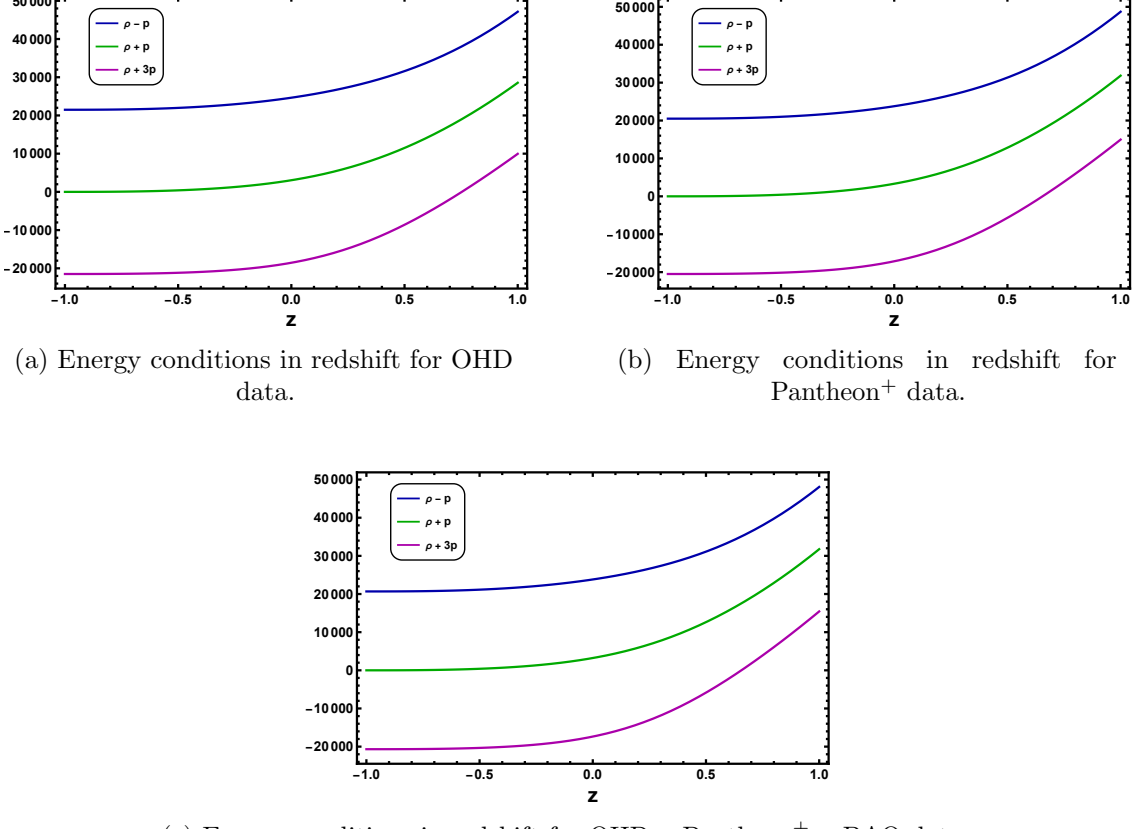


(a) Evolution of energy density in redshift.

(b) Evolution of EoS parameter in redshift.

FIGURE 5.2: The behavior of the dynamical parameters for model within coincident gauge.

In the study of cosmological models within modified gravity theories, examining energy conditions are crucial. Specifically, in the context of covariant $f(Q)$ gravity, we investigate the behavior of various energy conditions. The energy density must remain positive throughout cosmic evolution



(a) Energy conditions in redshift for OHD data.

(b) Energy conditions in redshift for Pantheon⁺ data.(c) Energy conditions in redshift for OHD + Pantheon⁺ + BAO data.

FIGURE 5.3: The behavior of energy conditions for the model within coincident gauge.

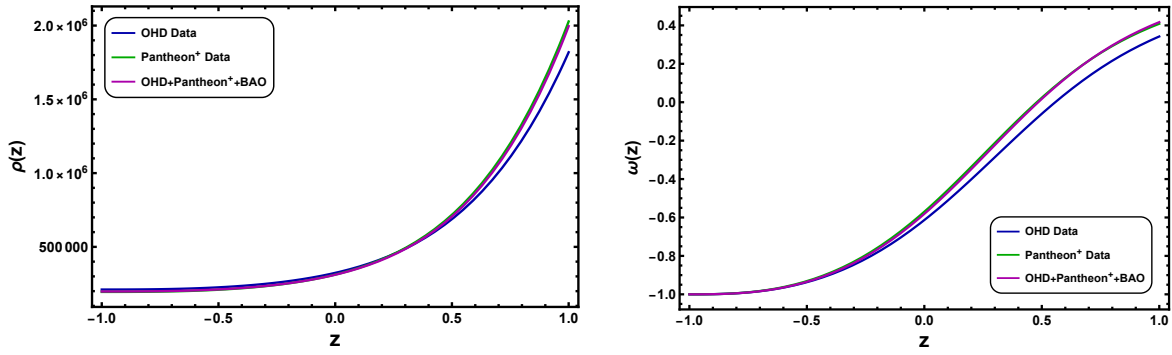
and these energy conditions essentially serve as boundary conditions. The violation of the SEC due to DE suggests that these boundary conditions may not hold physical relevance. However, because of the fundamental causal structure of space-time, the gravitation attraction can be characterized by the energy conditions [242]. Moreover, these boundary conditions play a significant role in shaping the cosmic evolution of the Universe [30].

The evolutionary behaviour of the energy conditions is depicted in Fig. 5.3, for the constrained values of the free parameters obtained from the OHD [Fig. 5.3a], Pantheon⁺ [Fig. 5.3b] and OHD + Pantheon⁺ + BAO [Fig. 5.3c] datasets. We observed that during the early epoch, the NEC decreases and remains positive throughout but vanishes at the late epoch. The DEC remains positive throughout and does not violate. While the SEC does not violate at early times, it does violate at late times. These observations highlight the dynamic nature of the energy conditions across different cosmological epochs. The parameter scheme for the plots is $Q_0 = 69$, $\alpha = -0.0287$ and $\beta = 0.345$.

5.4.2 Model reconstructed through non-coincident gauge

Here, we will analyze the dynamical behavior of the Universe for reconstructed model. Using the Eqs. (5.1), (5.2), (5.5) and Hubble parameter one can obtain the expressions for the variables ρ and p , which are derived from a field equations. These equations incorporate various parameters such as α_1 , α_2 , α_3 , β_1 , β_2 and γ_1 along with dynamical quantities like the Hubble parameter H and its derivative with respect to time t (i.e. \dot{H}).

$$\begin{aligned} \rho = & \frac{-\sqrt{3}}{2(27\gamma_1^2 - 8Q)^{3/2}} \left(648\beta_1\gamma_1^2H^2 - 729\beta_1\gamma_1^4 - 4374\beta_2\gamma_1^4H^2 - 192\beta_1H^2Q + 3240\beta_2\gamma_1^2H^2Q + 32\beta_2Q^3 \right. \\ & + 576\beta_1H\dot{H} - 576\beta_2H^2Q^2 + 7776\beta_2\gamma_1^2H\dot{H} - 1728\beta_2H\dot{H}Q - 32\beta_1Q^2 - 108\beta_2\gamma_1^2Q^2 - 432\beta_1\dot{H} \\ & + 1296\beta_2\dot{H}Q - 5832\beta_2\gamma_1^2\dot{H} + 324\beta_1\gamma_1^2Q \Big) - \frac{1}{2(27\gamma_1^2 - 8Q)} \left(96\alpha_3H^2Q^2 + 48\alpha_2H^2Q - 162\alpha_2\gamma_1^2H^2 \right. \\ & + 576\alpha_3H\dot{H}Q - 324\alpha_3\gamma_1^2H^2Q - 8\alpha_3Q^3 + 27\alpha_3\gamma_1^2Q^2 - 1944\alpha_3\gamma_1^2H\dot{H} + 8\alpha_1Q - 432\alpha_3\dot{H}Q - 27\alpha_1\gamma_1^2 \\ & \left. + 1458\alpha_3\gamma_1^2\dot{H} \right), \\ p = & 48\alpha_3H^2\dot{H} - 3\alpha_2H^2 - 6\alpha_3H^2Q - 48\alpha_3H\dot{H} - 2\alpha_2\dot{H} + 9\alpha_3\dot{H} - 4\alpha_3\dot{H}Q - \frac{1}{2}(\beta_1 + \beta_2Q)\sqrt{81\gamma_1 - 24Q} \\ & + \frac{\alpha_3Q^2}{2} - \frac{\alpha_1}{2} + \frac{\sqrt{3}}{(27\gamma_1^2 - 8Q)^{3/2}} \left(384\beta_1H\dot{H} - 384\beta_1H^2\dot{H} + 1152\beta_2H^2\dot{H}Q - 72\beta_1\dot{H} + 216\beta_2\dot{H}Q \right. \\ & + 5184\beta_2\gamma_1^2H\dot{H} - 5184\beta_2\gamma_1^2H^2\dot{H} - 1152\beta_2H\dot{H}Q - 972\beta_2\gamma_1^2\dot{H} \Big) + \frac{1}{\sqrt{9\gamma_1^2 - \frac{8Q}{3}}} \left(12\beta_1H^2 + 36\beta_2H^2Q \right. \\ & \left. + 8\beta_1\dot{H} - 81\beta_2\gamma_1^2H^2 - 54\beta_2\gamma_1^2\dot{H} + 24\beta_2\dot{H}Q - 6\beta_2Q^2 - 2\beta_1Q + \frac{27\beta_2\gamma_1^2Q}{2} \right). \end{aligned}$$



(a) Evolution of energy density in redshift. (b) Evolution of EoS parameter in redshift.

FIGURE 5.4: The behavior of the dynamical parameters for the model reconstructed through non-coincident gauge.

Fig. 5.4a shows that while the energy density decreases over time, it never completely vanishes. The current values of the EoS parameter are $\omega_0 \simeq -0.63$, $\omega_0 \simeq -0.59$ and $\omega_0 \simeq -0.60$ for the constrained free parameters from the OHD dataset, Pantheon⁺ dataset and the combined OHD + Pantheon⁺ + BAO dataset, respectively from Fig. 5.4b. The energy density and EoS parameters are determined by the coefficients of the model, which influence their evolution. This model exhibits quintessence behavior at present. As illustrated in Fig. 5.5, across all datasets,

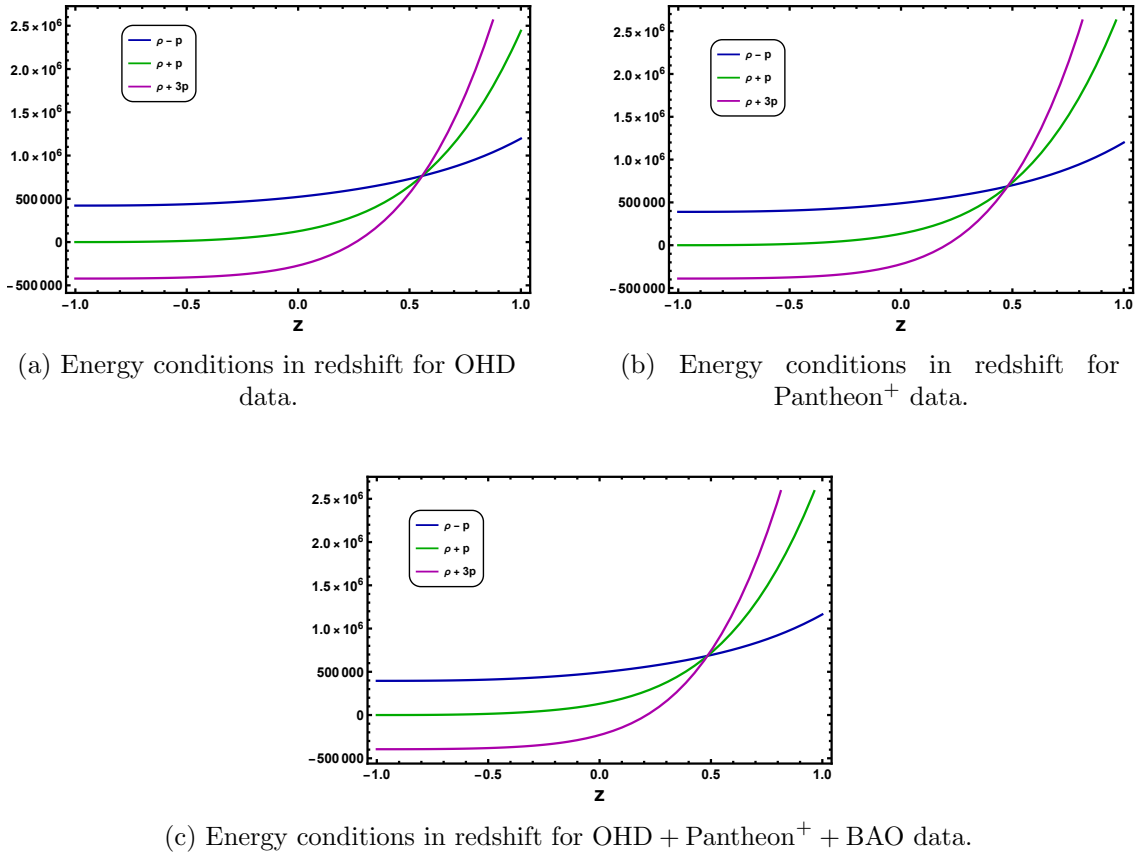


FIGURE 5.5: The behavior of energy conditions for the model reconstructed through non-coincident gauge.

the NEC decreases from early to late time, remains positive throughout, but approaches zero in late-time. In contrast, the DEC remains positive at all times without any violation. The SEC is satisfied in the early Universe but is violated in the late epoch. The parameter scheme for the plots is $\alpha_1 = 1.20$, $\alpha_2 = 0.50$, $\alpha_3 = -0.0001$, $\beta_1 = 0.90$ and $\beta_2 = 0.01$.

The dynamical behaviour and energy conditions are presented in the previous section offer valuable insights into the evolution of the models. To further understand the stability of the reconstructed model, we now turn to the analysis of scalar perturbations, which will provide a deeper understanding of the stability of the model.

5.4.3 Analyzing stability with scalar perturbation

Our focus in this section will be on perturbations of homogeneous and isotropic FLRW metrics and their evolution, which ultimately determines whether cosmological solutions are stable in $f(Q)$ gravity. In order to study perturbations near the solutions $H(t)$ and $\rho(t)$, let us consider small deviations from the Hubble parameter and the evolution of the energy density defined as [243, 244],

$$H(t) \rightarrow H(t)(1 + \delta), \quad \rho \rightarrow \rho(1 + \delta_m), \quad (5.10)$$

where δ and δ_m represent the isotropic deviation of the Hubble parameter and the matter over density, respectively. In this case, $H(t)$ and $\rho(t)$ represent zero order quantities [in some references, these are sometimes designated as $H_0(t)$ and $\rho_0(t)$, but this notation is avoided here in order to distinguish from quantities evaluated at present], which satisfy Eqs. (5.1), (5.2) and continuity equation provided in (1.23). The perturbation of the function f and its derivatives are

$$\delta f = f_Q \delta Q, \quad \delta f_Q = f_{QQ} \delta Q, \quad \delta f_{QQ} = f_{QQQ} \delta Q.$$

where δx represents the first-order perturbation of the variable x . Here $\delta Q = (-12H^2 + 9H)\delta$. In this way, the perturbed equations of Eq. (5.1) and continuity equation become,

$$c_1 \dot{\delta} + c_0 \delta = \rho \delta_m, \quad (5.11)$$

$$\dot{\delta_m} + 3H(1 + \omega)\delta = 0. \quad (5.12)$$

where

$$c_0 = 6f_Q H^2 - 72f_{QQ} H^4 + 108f_{QQ} H^3 - \frac{81f_{QQ} H^2}{2} + 36f_{QQ} H \dot{H} - \frac{27f_{QQ} \dot{H}}{2} - \frac{243}{2} f_{QQQ} H \dot{H} - 216f_{QQQ} H^3 \dot{H} + 324f_{QQQ} H^2 \dot{H},$$

$$c_1 = 18f_{QQ} H^2 - \frac{27f_{QQ} H}{2}.$$

By solving Eqs. (5.11) and (5.12), one can determine the stability of a particular FLRW cosmological solution in the context of $f(Q)$ gravity with connection-III. Since Eq. (5.11) has a linear character, the solution for $\delta(t)$ can generally be split into two branches: the first one

corresponds to the solution of the homogeneous equation in (5.11), which reflects perturbations induced by a particular gravitational Lagrangian. The second branch would correspond to the particular solution of that equation, which is merely affected by the growth of matter perturbations δ_m . Considering the Eqs. (5.5), (5.11), (5.12) and the Hubble parameter, one can find the perturbation equations for the reconstructed model. The analysis of cosmological

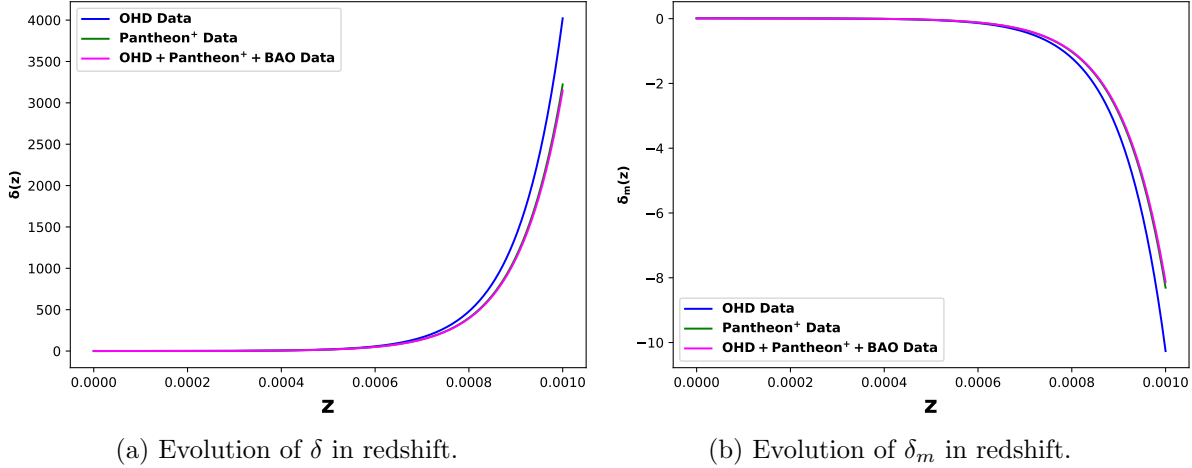


FIGURE 5.6: Evolution of δ and δ_m versus redshift. Herein, we set the initial conditions $\delta(0) = 0.1$ and $\delta_m(0) = 0.01$.

perturbations δ and δ_m as illustrated in Fig. 5.6 provides valuable insights into the behavior of these perturbations across different redshifts. Perturbation δ is compared against three datasets: OHD dataset, Pantheon⁺ dataset and the combined OHD + Pantheon⁺ + BAO dataset. Similarly, perturbation δ_m is evaluated using the same datasets. Both perturbations exhibit small variations, demonstrating consistency across different observational constraints. Importantly, it can be seen that δ and δ_m converge to zero at the late epoch in the redshift, which confirms the stability of the model with respect to the Hubble parameter. This convergence highlights the robustness of the model in describing the expansion of the Universe over time.

5.5 Conclusion

In this chapter, we applied the cosmological reconstruction method within the framework of $f(Q)$ gravity, using a non-trivial connection specifically, connection III. This introduces a non-metricity scalar that involves the Hubble parameter and an additional function. This unique formulation distinguishes the non-coincident gauge model, leading to novel cosmological dynamics and potential challenges related to stability. Through a comprehensive analysis utilizing the Hubble parameter $H(z)$ and various observational datasets, our models successfully capture the expansion history of the Universe. When comparing the two models, we found that both exhibit a decreasing energy density over time that does not vanish, but with different behaviors for the EoS parameter. The model within the coincident gauge results in an EoS parameter near

$\omega_0 \sim -0.78$ at the present time, indicating a more consistent dynamical evolution. On the other hand, the non-coincident gauge model shows a slightly higher EoS parameter ($\omega_0 \sim -0.63$) and a more significant violation of the SEC at late time.

Both models exhibit quintessence like behavior, but the non-coincident gauge model deviates more substantially from standard cosmology in the late Universe. This dual behavior highlights the flexibility of $f(Q)$ gravity in addressing the cosmological constant problem. Our detailed evaluation of the energy conditions for both models revealed that the NEC and the DEC are consistently satisfied, ensuring their physical plausibility. While the SEC is satisfied at early times, it is violated at later times, aligning with the observed accelerated expansion of the Universe.

Furthermore, a stability analysis through scalar perturbations confirmed the robustness of the non-coincident gauge model, indicating that it is free from instabilities. These results position $f(Q)$ gravity as a compelling alternative to the Λ CDM model, providing a comprehensive explanation for the accelerating expansion of the Universe and offering new insights into fundamental cosmological issues. This work makes a significant contribution to our understanding of cosmological dynamics within modified gravity theories and sets the stage for future research into the implications of $f(Q)$ gravity in modern cosmology.

Chapter 6

Concluding Remarks and Future perspectives

This thesis delves into the cosmological implications of various $f(Q)$ gravity models, providing valuable insights into the accelerated expansion of the Universe and the role of DE. Through in-depth analyses and comparisons with observational data, we demonstrate that these models present viable alternatives to the standard Λ CDM model.

Chapter 2 introduced a two $f(Q)$ gravity models, focusing on the log-square-root model and exponential model. The hybrid scale factor has been incorporated to analyze the evolutionary behavior of the models. The log-square-root model shows the quintessence behavior at present time and behaves like the Λ CDM at late times whereas exponential model shows the phantom behavior and the present value of the DE EoS parameter obtained to be $\omega_{DE} = -0.82$ and $\omega_{DE} = -1.01$ respectively. The dynamical system analysis has been performed for both the cosmological models obtained with the form of $f(Q)$ and the time varying deceleration parameter in the second phase. For both the models, the critical point $(0, 0, 1)$ and $(0, 0, 0)$ are unstable. Whereas, the curve $(x, 1 - x, 0)$ has all eigenvalues for Jacobian matrix are negative real part and zero gives the stable node behavior. The behavior of the critical points are validated in the 2-D and 3-D phase portraits. Moreover, the evolutionary behavior for both the models shows the present value of density parameters as, $\Omega_{DE} \approx 0.7$ and $\Omega_m \approx 0.3$. Both the models shows early radiation era and late time DE era, transition through matter dominated era. The total EoS parameter obtained from hybrid scale factor and the total EoS parameter from the evolution plot shows same behavior of Universe for both the models.

In Chapter 3, by considering higher power of non-metricity in the expression for $f(Q)$ and performing some algebraic manipulations, we explicitly derived the expression for the Hubble function in terms of the redshift. Then, we constrained the model parameters and the EoS parameter using Bayesian statistical analysis with MCMC techniques, along with observational data from Hubble measurements and extended Pantheon+SH0ES dataset. The error bar plots reveal that both the curve for our models and the Λ CDM model pass through the range obtained

from these datasets. Furthermore, the constrained parameters were validated using the BAO dataset and constraints on the geometrical parameters were derived to investigate the accelerating behavior of the Universe. This analysis shows that the cosmological model transitions from a deceleration to an acceleration phase. We derived a deceleration parameter $q_0 \approx -0.61$ for the transiting Universe at the present epoch. The EoS parameter was found to be -1.16 ± 0.17 and -1.15 ± 0.17 respectively from the Hubble dataset and Pantheon+SH0ES dataset respectively, indicating the phantom behavior of the model. Utilizing the constrained value of the Hubble parameter, we have calculated the age of the Universe and the $Om(z)$ diagnostic analysis has been performed, which provides a null test to the Λ CDM model. If the model deviates from the Λ CDM model, there may be interactions between DE and DM components. Our results suggest that the behavior of the $Om(z)$ parameter may favor a phantom phase.

Chapter 4 delve into the cosmological reconstruction in $f(Q)$ gravity with trivial connection. We have developed some novel form of deceleration parameter and studied its impact on the $f(Q)$ gravity in the context of accelerating Universe. The parametrization must to be carefully done, taking into account both theoretical and observational constraints, in order to ensure that it is reliable and predictive over all redshift ranges. The parametrized deceleration parameter presented in the paper offers a flexible framework for analyzing the dynamics of the Universe, enabling the exploration of various cosmological models and their implications. We constrained the cosmological parameters and validated the models utilizing the observational datasets such as OHD, SNe Ia and BAO. Bayesian statistical inference techniques and MCMC methods were employed for the analysis. Our results demonstrate that the parameters of our models match the observational data well. The power-law function, demonstrates compatibility with the latest high values of H_0 , aligning with recent observational values and indicating a DE-dominated Universe. Moreover the reconstructed $f(Q)$ model has GR as a particular limit, it has the same number of free parameters as Λ CDM, but in a cosmological context it creates a scenario that does not have Λ CDM as a limit. Whereas, the logarithmic function, aligns with a slightly reduced matter density and accurately models the accelerated expansion. The reconstructed $f(Q)$ model for logarithmic function is presented as a novel approach for describing cosmic evolution, particularly focusing on avoiding early-time instabilities and phantom behaviors. In this model, the effective EoS parameter remains strictly non-phantom. Also, this model passes the Big Bang Nucleosynthesis constraints trivially, meaning it does not interfere with the delicate balance required for early Universe Nucleosynthesis, making it a stable and potentially viable model for both early and late Universe dynamics. Finally the comparative analysis against Λ CDM using AIC and BIC metrics shows that these models provide competitive fits, with model II offering a slight edge in simplicity.

In Chapter 5, we presented a detailed implementation of the cosmological reconstruction method in $f(Q)$ gravity, utilizing non-trivial connections, specifically connection III within a symmetric teleparallel background. Through this approach, we derived an intriguing cosmological model, which is a noteworthy step in categorizing the association of cosmological models in modified gravity. Our model has been meticulously analyzed using the Hubble parameter $H(z)$ and various observational datasets, providing a robust representation of the expansion history of

the Universe. Then the dynamical behaviour of the model within the coincident gauge, along with the reconstructed model has been studied. Both the models exhibits quintessence behavior at the current epoch, characterized by a dynamic DE component that evolves over time. This behavior transitions smoothly to the Λ CDM model at late time, which is consistent with the observed accelerated expansion of the Universe. The dual behavior of the reconstructed model underscores the versatility and potential of $f(Q)$ gravity in addressing the cosmological constant problem. We have also thoroughly evaluated the energy conditions for both the models. The NEC remains positive throughout the cosmic evolution, indicating that the energy density is non-negative and the speed of sound is real. The DEC is consistently satisfied, ensuring that the energy density exceeds the pressure and the energy propagation remains within causal bounds. The SEC, which is satisfied in the early Universe, is violated in the late epoch. This violation is consistent with the observed accelerated expansion and suggests a deviation from standard matter-dominated model. The stability analysis for the reconstructed model through scalar perturbations has confirmed the robustness of the model.

In summary, this thesis has demonstrated that the models, based on the $f(Q)$ gravity, provide promising alternatives to the Λ CDM model. The research explored various forms of $f(Q)$ gravity, including models based on the log-square-root, exponential and higher powers of non-metricity, offering robust frameworks for understanding the accelerated expansion of the Universe. These models have shown strong agreement with current cosmological observations, including OHD, SNe Ia and BAO. Additionally, the thesis presented novel cosmological models reconstructed within the $f(Q)$ gravity framework, utilizing trivial connections and non-trivial connections. These reconstructed models offer an effective description of cosmic evolution, ensuring compatibility with both early and late Universe dynamics, while also providing a viable alternative to the Λ CDM model. The reconstructed models further demonstrated smooth transitions from deceleration to acceleration and matched observational data well. The findings also highlighted the versatility of $f(Q)$ gravity, with models exhibiting both quintessence and phantom behavior as well as smooth transitions between deceleration and acceleration phases of the Universe. Furthermore, the stability analysis and energy condition evaluations confirmed the physical viability of the models, with particular attention given to their ability to describe the nature of DE and the evolution of the Universe. The comparison with the Λ CDM model further supports the competitive and viable nature of $f(Q)$ gravity models in explaining the accelerating expansion of the Universe and the nature of DE.

In the future, the $f(Q)$ gravity models can be extended to explore their effects in strong gravitational regimes, particularly on the propagation of gravitational waves. This would provide a valuable platform for investigating how these models influence the propagation of gravitational waves, particularly in extreme cosmic environments such as black holes, neutron stars and the early Universe. Analyzing the full CMB, Large Scale Structure spectra, DESI data, weak lensing data and other relevant datasets can offer valuable insights into our findings. Such analyses are essential for assessing whether these models provide a better fit compared to the standard Λ CDM model or not. Further extending these models to higher-dimensional spacetime or including extra fields may provide new insights into cosmic inflation and DM interactions.

References

- [1] J. Moffat, “Modified gravity (MOG), cosmology and black holes,” *J. Cosmol. Astropart. Phys.* **2021** (2021) 017.
- [2] S. Vilhena, S. Duarte, M. Dutra and P. Pompeia, “Neutron stars in modified teleparallel gravity,” *J. Cosmol. Astropart. Phys.* **2023** (2023) 044.
- [3] A. Einstein, “Cosmological Considerations in the General Theory of Relativity,” *Ber. Kgl. Preuss. Akad. Wiss. Berlin* (1917) 142.
- [4] A. Friedman, “Über die Krümmung des Raumes,” *Zeitschrift für Physik* **10** (1922) 377.
- [5] E. Hubble, “A relation between distance and radial velocity among extra-galactic nebulae,” *Proc. N. A. S.* **15** (1929) 168.
- [6] E. Hubble and M.L. Humason, “The Velocity-Distance Relation among Extra-Galactic Nebulae ,” *Astron. J.* **74** (1931) 43.
- [7] A. Friedman, “Über die Möglichkeit einer Welt mit konstanter negativer Krümmung des Raumes,” *Zeitschrift für Physik* **21** (1924) 326.
- [8] G. Lemaître, “Republication of: A homogeneous universe of constant mass and increasing radius accounting for the radial velocity of extra-galactic nebulae,” *Annales Soc. Sci. Brux. Ser. I Sci. Math. Astron. Phys.* **49** (1927) 1635.
- [9] H.P. Robertson, “Kinematics and World-Structure,” *Astrophys. J.* **82** (1935) 284.
- [10] A.G. Walker, “On Milne’s Theory of World-Structure,” *Proc. London Math. Soc.* **42** (1937) 90.
- [11] J. Yadav, S. Bharadwaj, B. Pandey and T.R. Seshadri, “Testing homogeneity on large scales in the Sloan Digital Sky Survey Data Release One,” *Mon. Not. Roy. Astron. Soc.* **364** (2005) 601.
- [12] R.G. Clowes, K.A. Harris, S. Raghunathan, L.E. Campusano et al., “A structure in the early Universe at $z \sim 1.3$ that exceeds the homogeneity scale of the R-W concordance cosmology,” *Mon. Not. Roy. Astron. Soc.* **429** (2013) 2910.
- [13] W. Hu and S. Dodelson, “Cosmic microwave background anisotropies,” *Annu. Rev. Astron. Astrophys.* **40** (2002) 171.

- [14] A.A. Starobinsky, “Spectrum of relict gravitational radiation and the early state of the universe,” *JETP Lett.* **30** (1979) 682.
- [15] A. A. Starobinsky, “Dynamics of phase transition in the new inflationary universe scenario and generation of perturbations,” *Phys. Lett. B* **117** (1982) 175.
- [16] A.H. Guth, “Inflationary universe: A possible solution to the horizon and flatness problems,” *Phys. Rev. D* **23** (1981) 347.
- [17] A. Linde, “A new inflationary universe scenario: A possible solution of the horizon, flatness, homogeneity, isotropy and primordial monopole problems,” *Phys. Lett. B* **108** (1982) 389.
- [18] V.M. Slipher, “Nebulae,” *Proc. American Philosophical Soc.* **56** (1917) 403.
- [19] A.G. Riess, A.V. Filippenko, P. Challis, A. Clocchiatti et al., “Observational Evidence from Supernovae for an Accelerating Universe and a Cosmological Constant,” *Astron. J.* **116** (1998) 1009.
- [20] B.P. Schmidt, N.B. Suntzeff, M.M. Phillips, R.A. Schommer et al., “The High-Z Supernova Search: Measuring Cosmic Deceleration and Global Curvature of the Universe Using Type Ia Supernovae*,” *Astrophys. J.* **507** (1998) 46.
- [21] A.G. Riess, R.P. Kirshner, B.P. Schmidt, S. Jha et al., “BVRI Light Curves for 22 Type Ia Supernovae,” *Astron. J.* **117** (1999) 707.
- [22] S. Perlmutter, G. Aldering, G. Goldhaber, R.A. Knop et al., “Measurements of Ω and Λ from 42 High-Redshift Supernovae,” *Astron. J.* **517** (1999) 565.
- [23] P.A.R. Ade, N. Aghanim, M. Arnaud, M. Ashdown et al., “Planck 2015 results - XIII. Cosmological parameters,” *Astron. Astrophys.* **594** (2016) A13.
- [24] S. Weinberg, *Gravitation and Cosmology*, Springer Cham (1972).
- [25] A.K. Raychaudhuri, *Theoretical Cosmology*, Oxford University Press (1979).
- [26] T. Padmanabhan, *Theoretical Astrophysics, Vol III: Galaxies and Cosmology*, Cambridge University Press (2000).
- [27] J. Rich, *Fundamentals of Cosmology*, Springer (2009).
- [28] A.R. Liddle, *An Introduction to Modern Cosmology*, John Wiley & Sons (2015).
- [29] B. Ryden, *Introduction to cosmology*, Cambridge University Press (2017).
- [30] S.M. Carroll, M. Hoffman and M. Trodden, “Can the dark energy equation-of-state parameter w be less than -1 ?” *Phys. Rev. D* **68** (2003) 023509.
- [31] R. Penrose, “Gravitational Collapse and Space-Time Singularities,” *Phys. Rev. Lett.* **14** (1965) 57.

- [32] S.W. Hawking, “The occurrence of singularities in cosmology,” *Proc. R. Soc. A* **294** (1966) 571.
- [33] J. Ehlers, “A. K. Raychaudhuri and his equations,” *Int. J. Mod. Phys. D* **15** (2006) 1573.
- [34] S. Nojiri and S.D. Odintsov, “Introduction to modified gravity and gravitational alternative for dark energy,” *Int. J. Geom. Meth. Mod. Phys.* **4** (2007) 115.
- [35] G.F.R.E. S. W. Hawking, *The Large Scale Structure of Space-Time*, Cambridge University Press (1973).
- [36] E.-A. Kontou and K. Sanders, “Energy conditions in general relativity and quantum field theory,” *Classical and Quantum Gravity* **37** (2020) 193001.
- [37] S. Capozziello, F.S. Lobo and J.P. Mimoso, “Energy conditions in modified gravity,” *Phys. Lett. B* **730** (2014) 280.
- [38] U. Alam, V. Sahni, T. Deep Saini and A.A. Starobinsky, “Exploring the expanding Universe and dark energy using the statefinder diagnostic,” *Mon. Not. Roy. Astron. Soc.* **344** (2003) 1057.
- [39] V. Sahni, T.D. Saini, A.A. Starobinsky and U. Alam, “Statefinder—A new geometrical diagnostic of dark energy,” *J. Exp. Theo. Phys. Lett.* **77** (2003) 201.
- [40] N. Aghanim, Y. Akrami, M. Ashdown, J. Aumont et al., “Planck 2018 results - VI. Cosmological parameters,” *Astron. Astrophys.* **641** (2020) A6.
- [41] A. Joyce, B. Jain, J. Khoury and M. Trodden, “Beyond the cosmological standard model,” *Physics Reports* **568** (2015) 1.
- [42] S. Tsujikawa, “Introductory review of cosmic inflation,” [arXiv:hep-ph/0304257](https://arxiv.org/abs/hep-ph/0304257).
- [43] H.E.S. Velten, R.F. vom Marttens and W. Zimdahl, “Aspects of the cosmological “coincidence problem”,” *Eur. Phys. J. C* **74** (2014) 3160.
- [44] D. Astesiano and M.L. Ruggiero, “Galactic dark matter effects from purely geometrical aspects of general relativity,” *Phys. Rev. D* **106** (2022) 044061.
- [45] T. Katsuragawa and S. Matsuzaki, “Dark matter in modified gravity?,” *Phys. Rev. D* **95** (2017) 044040.
- [46] R. Zaregonbadi, M. Farhoudi and N. Riazi, “Dark matter from $f(R, T)$ gravity,” *Phys. Rev. D* **94** (2016) 084052.
- [47] E. Di Valentino, L.A. Anchordoqui, O. Akarsu, Y. Ali-Haimoud et al., “Snowmass2021 - Letter of interest cosmology intertwined II: The hubble constant tension,” *Astropart. Phys.* **131** (2021) 102605.
- [48] E. Di Valentino, L.A. Anchordoqui, O. Akarsu, Y. Ali-Haimoud et al., “Cosmology intertwined III: f σ 8 and S8,” *Astropar. Phys.* **131** (2021) 102604.

- [49] D. Benisty, “Quantifying the S_8 tension with the Redshift Space Distortion data set,” *Phys. of the Dark Universe* **31** (2021) 100766.
- [50] S. Joudaki, A. Mead, C. Blake, A. Choi et al., “KiDS-450: testing extensions to the standard cosmological model,” *Mon. Not. Roy. Astron. Soc.* **471** (2017) 1259.
- [51] E.V. Linder, “Exploring the Expansion History of the Universe,” *Phys. Rev. Lett.* **90** (2003) 091301.
- [52] H.K. Jassal, J.S. Bagla and T. Padmanabhan, “Understanding the origin of CMB constraints on dark energy,” *Mon. Not. Roy. Astron. Soc.* **405** (2010) 2639.
- [53] E. Barboza and J. Alcaniz, “A parametric model for dark energy,” *Phys. Lett. B* **666** (2008) 415.
- [54] C. Wetterich, “Phenomenological parameterization of quintessence,” *Phys. Lett. B* **594** (2004) 17.
- [55] G. Gupta, R. Rangarajan and A.A. Sen, “Thawing quintessence from the inflationary epoch to today,” *Phys. Rev. D* **92** (2015) 123003.
- [56] T. Chiba, A. De Felice and S. Tsujikawa, “Observational constraints on quintessence: Thawing, tracker, and scaling models,” *Phys. Rev. D* **87** (2013) 083505.
- [57] N. Roy and N. Banerjee, “Quintessence scalar field: A dynamical systems study,” *Eur. Phys. J. Plus* **129** (2014) 162.
- [58] G. Pantazis, S. Nesseris and L. Perivolaropoulos, “Comparison of thawing and freezing dark energy parametrizations,” *Phys. Rev. D* **93** (2016) 103503.
- [59] R. Caldwell, “A phantom menace? Cosmological consequences of a dark energy component with super-negative equation of state,” *Phys. Lett. B* **545** (2002) 23.
- [60] Y.-F. Cai and J. Wang, “Dark energy model with spinor matter and its quintom scenario,” *Classical and Quantum Gravity* **25** (2008) 165014.
- [61] B. Feng, X. Wang and X. Zhang, “Dark energy constraints from the cosmic age and supernova,” *Phys. Lett. B* **607** (2005) 35.
- [62] C. Armendáriz-Picón, T. Damour and V. Mukhanov, “k-Inflation,” *Phys. Lett. B* **458** (1999) 209.
- [63] C. Armendariz-Picon, V. Mukhanov and P.J. Steinhardt, “Essentials of k-essence,” *Phys. Rev. D* **63** (2001) 103510.
- [64] T. Chiba, T. Okabe and M. Yamaguchi, “Kinetically driven quintessence,” *Phys. Rev. D* **62** (2000) 023511.
- [65] S. Tsujikawa, *Lectures on Cosmology: Modified Gravity Models of Dark Energy*, Springer (2010).

- [66] Timothy Clifton and Pedro G. Ferreira and Antonio Padilla and Constantinos Skordis, “Modified gravity and cosmology,” *Phys. Rep.* **513** (2012) 1.
- [67] S.M. Carroll, A. De Felice, V. Duvvuri, D.A. Easson et al., “Cosmology of generalized modified gravity models,” *Phys. Rev. D* **71** (2005) 063513.
- [68] S. Nojiri and S.D. Odintsov, “Newton law corrections and instabilities in $f(R)$ gravity with the effective cosmological constant epoch,” *Phys. Lett. B* **652** (2007) 343.
- [69] H. Motohashi and A.A. Starobinsky, “Constant-roll inflation in scalar-tensor gravity,” *J. Cosmol. Astropart. Phys.* **2019** (2019) 025.
- [70] G.J. Olmo, D. Rubiera-Garcia and A. Wojnar, “Minimum main sequence mass in quadratic Palatini $f(\mathcal{R})$ gravity,” *Phys. Rev. D* **100** (2019) 044020.
- [71] S.D. Odintsov and V.K. Oikonomou, “ $f(R)$ gravity inflation with string-corrected axion dark matter,” *Phys. Rev. D* **99** (2019) 064049.
- [72] S.D. Odintsov and V.K. Oikonomou, “Geometric inflation and dark energy with axion $F(R)$ gravity,” *Phys. Rev. D* **101** (2020) 044009.
- [73] V.K. Oikonomou, “Unifying inflation with early and late dark energy epochs in axion $F(R)$ gravity,” *Phys. Rev. D* **103** (2021) 044036.
- [74] R.H. Sanders, “A Stratified Framework for Scalar-Tensor Theories of Modified Dynamics,” *Astrophys. J.* **480** (1997) 492.
- [75] S. Das and N. Banerjee, “Brans-Dicke scalar field as a chameleon,” *Phys. Rev. D* **78** (2008) 043512.
- [76] A. Riazuelo and J.-P. Uzan, “Cosmological observations in scalar-tensor quintessence,” *Phys. Rev. D* **66** (2002) 023525.
- [77] B. Boisseau, G. Esposito-Farèse, D. Polarski and A.A. Starobinsky, “Reconstruction of a Scalar-Tensor Theory of Gravity in an Accelerating Universe,” *Phys. Rev. Lett.* **85** (2000) 2236.
- [78] M. Crisostomi and K. Koyama, “Self-accelerating universe in scalar-tensor theories after GW170817,” *Phys. Rev. D* **97** (2018) 084004.
- [79] E. Elizalde, S. Nojiri and S.D. Odintsov, “Late-time cosmology in a (phantom) scalar-tensor theory: Dark energy and the cosmic speed-up,” *Phys. Rev. D* **70** (2004) 043539.
- [80] S. Capozziello, O. Luongo and E.N. Saridakis, “Transition redshift in $f(T)$ cosmology and observational constraints,” *Phys. Rev. D* **91** (2015) 124037.
- [81] Y.-F. Cai, S. Capozziello, M. De Laurentis and E.N. Saridakis, “ $f(T)$ teleparallel gravity and cosmology,” *Rept. Prog. Phys.* **79** (2016) 106901.

- [82] R.C. Nunes, “Structure formation in $f(T)$ gravity and a solution for H_0 tension,” *J. Cosmol. Astropart. Phys.* **2018** (2018) 052.
- [83] F.K. Anagnostopoulos, S. Basilakos and E.N. Saridakis, “Bayesian analysis of $f(T)$ gravity using $f\sigma_8$ data,” *Phys. Rev. D* **100** (2019) 083517.
- [84] S. Bahamonde, J.L. Said and M. Zubair, “Solar system tests in modified teleparallel gravity,” *J. Cosmol. Astropart. Phys.* **2020** (2020) 024.
- [85] J.B. Jiménez, L. Heisenberg and T. Koivisto, “Coincident general relativity,” *Phys. Rev. D* **98** (2018) 044048.
- [86] R. Lazkoz, F.S.N. Lobo, M. Ortiz-Baños and V. Salzano, “Observational constraints of $f(Q)$ gravity,” *Phys. Rev. D* **100** (2019) 104027.
- [87] B.J. Barros, T. Barreiro, T. Koivisto and N.J. Nunes, “Testing $F(Q)$ gravity with redshift space distortions,” *Phys. of the Dark Universe* **30** (2020) 100616.
- [88] F.K. Anagnostopoulos, S. Basilakos and E.N. Saridakis, “First evidence that non-metricity $f(Q)$ gravity could challenge Λ CDM,” *Phys. Lett. B* **822** (2021) 136634.
- [89] N. Frusciante, “Signatures of $f(Q)$ gravity in cosmology,” *Phys. Rev. D* **103** (2021) 044021.
- [90] K. Hu, T. Katsuragawa and T. Qiu, “ADM formulation and Hamiltonian analysis of $f(Q)$ gravity,” *Phys. Rev. D* **106** (2022) 044025.
- [91] T. Harko, F.S.N. Lobo, S. Nojiri and S.D. Odintsov, “ $f(R, T)$ gravity,” *Phys. Rev. D* **84** (2011) 024020.
- [92] R. Myrzakulov, “FRW cosmology in $F(R, T)$ gravity,” *Eur. Phys. J. C* **72** (2012) 2203.
- [93] T. Harko and F.S.N. Lobo, “ $f(R, L_m)$ gravity,” *Eur. Phys. J. C* **70** (2010) 373.
- [94] Y. Xu, G. Li, T. Harko and S.-D. Liang, “ $f(Q, T)$ gravity,” *Eur. Phys. J. C* **79** (2019) 708.
- [95] Y. Xu, S. Shahidi and S.-D. Liang, “Weyl type $f(Q, T)$ gravity, and its cosmological implications,” *Eur. Phys. J. C* **80** (2020) 449.
- [96] F.W. Hehl, J. McCrea, E.W. Mielke and Y. Ne’eman, “Metric-affine gauge theory of gravity: field equations, Noether identities, world spinors, and breaking of dilation invariance,” *Phys. Rep.* **258** (1995) 1.
- [97] T. Ortín, *Gravity and Strings*, Cambridge University Press (2004).
- [98] J.B. Jiménez, L. Heisenberg and T.S. Koivisto, “Teleparallel Palatini theories,” *J. Cosmol. Astropart. Phys.* **2018** (2018) 039.
- [99] L. Järv, M. Rünklä, M. Saal and O. Vilson, “Nonmetricity formulation of general relativity and its scalar-tensor extension,” *Phys. Rev. D* **97** (2018) 124025.

- [100] A. Einstein, “The Field Equations of Gravitation,” *Sitzungsber. Preuss. Akad. Wiss. Berlin (Math. Phys.)* **1915** (1915) 844.
- [101] L. Heisenberg, “Review on $f(\mathbb{Q})$ gravity,” *Phys. Rep.* **1066** (2024) 1.
- [102] J.M. Nester and H.-J. Yo, “Symmetric teleparallel general relativity,” *Chin. J. Phys.* **37** (1999) 113 [[arXiv:gr-qc/9809049](https://arxiv.org/abs/gr-qc/9809049)].
- [103] D. Zhao, “Covariant formulation of $f(Q)$ theory,” *Eur. Phys. J. C* **82** (2022) 303.
- [104] A. Golovnev, T. Koivisto and M. Sandstad, “On the covariance of teleparallel gravity theories,” *Classical and Quantum Gravity* **34** (2017) 145013.
- [105] G.W. Gibbons and S.W. Hawking, “Action integrals and partition functions in quantum gravity,” *Phys. Rev. D* **15** (1977) 2752.
- [106] T. Harko, T.S. Koivisto, F.S.N. Lobo, G.J. Olmo et al., “Coupling matter in modified Q gravity,” *Phys. Rev. D* **98** (2018) 084043.
- [107] M. Hohmann, C. Pfeifer, U. Ualikhanova and J.L. Said, “Propagation of gravitational waves in symmetric teleparallel gravity theories,” *Phys. Rev. D* **99** (2019) 024009.
- [108] I. Soudi, G. Farrugia, J.L. Said, V. Gakis et al., “Polarization of gravitational waves in symmetric teleparallel theories of gravity and their modifications,” *Phys. Rev. D* **100** (2019) 044008.
- [109] F. Bajardi, D. Vernieri and S. Capozziello, “Bouncing cosmology in $f(Q)$ symmetric teleparallel gravity,” *Eur. Phys. J. Plus* **135** (2020) 912.
- [110] R.-H. Lin and X.-H. Zhai, “Spherically symmetric configuration in $f(Q)$ gravity,” *Phys. Rev. D* **103** (2021) 124001.
- [111] W. Khyllep, A. Paliathanasis and J. Dutta, “Cosmological solutions and growth index of matter perturbations in $f(Q)$ gravity,” *Phys. Rev. D* **103** (2021) 103521.
- [112] N. Dimakis, M. Roumeliotis, A. Paliathanasis, P.S. Apostolopoulos et al., “Self-similar cosmological solutions in symmetric teleparallel theory: Friedmann-Lemaître-Robertson-Walker spacetimes,” *Phys. Rev. D* **106** (2022) 123516.
- [113] D. Foreman-Mackey, D.W. Hogg, D. Lang and J. Goodman, “emcee: The mcmc hammer,” *PASP* **125** (2013) 306.
- [114] A. Lewis, “GetDist: a Python package for analysing Monte Carlo samples,” [arXiv:1910.13970](https://arxiv.org/abs/1910.13970) (2019) [[1910.13970](https://arxiv.org/abs/1910.13970)].
- [115] H. Yu, B. Ratra and F.-Y. Wang, “Hubble Parameter and Baryon Acoustic Oscillation Measurement Constraints on the Hubble Constant, the Deviation from the spatially Flat Λ CDM Model, the Deceleration-Acceleration Transition Redshift, and Spatial Curvature,” *Astrophys. J.* **856** (2018) 3.

- [116] M. Moresco, A. Cimatti, R. Jimenez, L. Pozzetti et al., “Improved constraints on the expansion rate of the Universe up to $z \sim 1.1$ from the spectroscopic evolution of cosmic chronometers,” *J. Cosmol. Astropart. Phys.* **2012** (2012) 006.
- [117] M. Moresco, L. Pozzetti, A. Cimatti, R. Jimenez et al., “A 6% measurement of the Hubble parameter at $z \sim 0.45$: direct evidence of the epoch of cosmic re-acceleration,” *J. Cosmol. Astropart. Phys.* **2016** (2016) 014.
- [118] G. Bruzual and S. Charlot, “Stellar population synthesis at the resolution of 2003,” *Mon. Not. Roy. Astron. Soc.* **344** (2003) 1000.
- [119] Z. Cong, Z. Han, Y. Shuo, L. Siqi et al., “Four new observational $H(z)$ data from luminous red galaxies in the Sloan Digital Sky Survey data release seven,” *Res. Astron. Astrophys.* **14** (2014) 1221.
- [120] C. Maraston and G. Strömbäck, “Stellar population models at high spectral resolution: High-resolution stellar population models,” *Mon. Not. Roy. Astron. Soc.* **418** (2011) 2785.
- [121] M. Moresco, “Raising the bar: new constraints on the Hubble parameter with cosmic chronometers at $z \sim 2$,” *Mon. Not. Roy. Astron. Soc. Lett.* **450** (2015) L16.
- [122] D. Stern, R. Jimenez, L. Verde, M. Kamionkowski et al., “Cosmic chronometers: constraining the equation of state of dark energy. I: $H(z)$ measurements,” *J. Cosmol. Astropart. Phys.* **2010** (2010) 008.
- [123] G. Sharov and V. Vasiliev, “How predictions of cosmological models depend on Hubble parameter data sets,” *Math. Modell. Geomet.* **6** (2018) 1.
- [124] M. Moresco, L. Amati, L. Amendola, S. Birrer et al., “Unveiling the Universe with emerging cosmological probes,” *Living Rev. Relativ.* **25** (2022) 6.
- [125] J.A. Holtzman, J. Marriner, R. Kessler, M. Sako et al., “The Sloan Digital Sky Survey-II: Photometry and Supernova Ia Light Curves from the 2005 Data,” *Astron. J.* **136** (2008) 2306.
- [126] R. Kessler, A.C. Becker, D. Cinabro, J. Vanderplas et al., “First-year Sloan Digital Sky Survey-II Supernova Results: Hubble Diagram and Cosmological Parameters,” *Astrophys. J. Lett. Supp. Ser.* **185** (2009) 32.
- [127] J. Leaman, W. Li, R. Chornock and A.V. Filippenko, “Nearby supernova rates from the Lick Observatory Supernova Search – I. The methods and data base,” *Mon. Not. Roy. Astron. Soc.* **412** (2011) 1419.
- [128] W. Li, J. Leaman, R. Chornock, A.V. Filippenko et al., “Nearby supernova rates from the Lick Observatory Supernova Search – II. The observed luminosity functions and fractions of supernovae in a complete sample,” *Mon. Not. Roy. Astron. Soc.* **412** (2011) 1441.

[129] Y. Copin, C. Buton, E. Gangler, G. Smadja et al., *The Nearby Supernova Factory: toward a high-precision spectro – photometry*, SF2A Conference (2007).

[130] R.A. Scalzo, G. Aldering, P. Antilogus, C. Aragon et al., “Nearby supernova factory observations of sn 2007if: first total mass measurement of a super-chandrasekhar-mass progenitor,” *Astrophys. J.* **713** (2010) 1073.

[131] P. Astier, J. Guy, N. Regnault, R. Pain et al., “The Supernova Legacy Survey: measurement of Ω_M , Ω_Λ and w from the first year data set,” *Astron. Astrophys.* **447** (2006) 31.

[132] S. Baumont, C. Balland, P. Astier, J. Guy et al., “Photometry assisted spectral extraction (phase) and identification of snls supernovae*,” *Astron. Astrophys.* **491** (2008) 567.

[133] A.G. Riess, L.-G. Strolger, J. Tonry, S. Casertano et al., “Type Ia Supernova Discoveries at $z > 1$ from the Hubble Space Telescope: Evidence for Past Deceleration and Constraints on Dark Energy Evolution*,” *Astrophys. J.* **607** (2004) 665.

[134] A.G. Riess, L.-G. Strolger, S. Casertano, H.C. Ferguson et al., “New Hubble Space Telescope Discoveries of Type Ia Supernovae at $z \geq 1$: Narrowing Constraints on the Early Behavior of Dark Energy*,” *Astrophys. J.* **659** (2007) 98.

[135] M. Visser, “Jerk, snap and the cosmological equation of state,” *Classical Quantum Gravity* **21** (2004) 2603.

[136] D. Scolnic, D. Brout, A. Carr, A.G. Riess et al., “The Pantheon+ Analysis: The Full Data Set and Light-curve Release,” *Astrophys. J.* **938** (2022) 113.

[137] D. Brout, D. Scolnic, B. Popovic, A.G. Riess et al., “The Pantheon+ Analysis: Cosmological Constraints,” *Astrophys. J.* **938** (2022) 110.

[138] A.G. Riess, W. Yuan, L.M. Macri, D. Scolnic et al., “A Comprehensive Measurement of the Local Value of the Hubble Constant with $1 \text{ km s}^{-1} \text{ Mpc}^{-1}$ Uncertainty from the Hubble Space Telescope and the SH0ES Team,” *Astrophys. J. Lett.* **934** (2022) L7.

[139] P.J.E. Peebles and J.T. Yu, “Primeval Adiabatic Perturbation in an Expanding Universe,” *Astrophys. J.* **162** (1970) 815.

[140] P.J.E. Peebles and B. Ratra, “The Cosmological Constant and Dark Energy,” *Rev. Mod. Phys.* **75** (2003) 559.

[141] U. Alam, V. Sahni and A.A. Starobinsky, “The case for dynamical dark energy revisited,” *J. Cosmol. Astropart. Phys.* **2004** (2004) 008.

[142] J. Jönsson, A. Goobar, R. Amanullah and L. Bergström, “No evidence for dark energy metamorphosis?,” *J. Cosmol. Astropart. Phys.* **2004** (2004) 007.

[143] M. Colless, B.A. Peterson, C. Jackson and J.A.P. others, “The 2dF Galaxy Redshift Survey: Final Data Release,” *arXiv:astro-ph/0306581* (2003) [[astro-ph/0306581](https://arxiv.org/abs/astro-ph/0306581)].

[144] D.G. York, J. Adelman, J. John E. Anderson, S.F. Anderson et al., “The Sloan Digital Sky Survey: Technical Summary,” *Astron. J.* **120** (2000) 1579.

[145] M. Tegmark, D.J. Eisenstein, M.A. Strauss, D.H. Weinberg et al., “Cosmological constraints from the sdss luminous red galaxies,” *Phys. Rev. D* **74** (2006) 123507.

[146] A.G. Adame, J. Aguilar, S. Ahlen, S. Alam et al., “DESI 2024 VI: Cosmological Constraints from the Measurements of Baryon Acoustic Oscillations,” *arXiv:2404.03002 [astro-ph.CO]* (2024) .

[147] D.N. Spergel, L. Verde, H.V. Peiris, E. Komatsu et al., “First-Year Wilkinson Microwave Anisotropy Probe (WMAP)* Observations: Determination of Cosmological Parameters,” *Astrophys. J. Suppl. Ser.* **148** (2003) 175.

[148] G. Hinshaw, D. Larson, E. Komatsu, D.N. Spergel et al., “Nine-Year Wilkinson Microwave Anisotropy Probe (WMAP) Observations: Cosmological Parameter Results,” *Astrophys. J. Suppl. Ser.* **208** (2013) 19.

[149] S. Alam, M. Ata, S. Bailey, F. Beutler et al., “The clustering of galaxies in the completed SDSS-III Baryon Oscillation Spectroscopic Survey: cosmological analysis of the DR12 galaxy sample,” *Mon. Not. Roy. Astron. Soc.* **470** (2017) 2617.

[150] S.H. Strogatz, *Nonlinear Dynamics and Chaos With Applications to Physics, Biology, Chemistry, and Engineering*, Cambridge, MA : Westview Press (2000).

[151] S. Wiggins, *Introduction to applied nonlinear dynamical systems and chaos* (Vol. 2), Springer Science & Business Media (2003).

[152] P. Glendinning, *Stability, instability and chaos: an introduction to the theory of nonlinear differential equations*, Cambridge University Press (1994).

[153] K. Koyama, “Cosmological tests of modified gravity,” *Rep. Prog. Phys.* **79** (2016) 046902.

[154] A.K. Sharma and M.M. Verma, “Effect of the Modified Gravity on the Large-scale Structure Formation,” *Astrophys. J.* **934** (2022) 13.

[155] W. Khyllep, J. Dutta, E.N. Saridakis and K. Yesmakhanova, “Cosmology in $f(Q)$ gravity: A unified dynamical systems analysis of the background and perturbations,” *Phys. Rev. D* **107** (2023) 044022.

[156] A. Bonanno and S. Carloni, “Dynamical system analysis of cosmologies with running cosmological constant from quantum Einstein gravity,” *New J. Phys.* **14** (2012) 025008.

[157] A.S. Agrawal, S. Chakraborty, B. Mishra, J. Dutta et al., “Global phase space analysis for a class of single scalar field bouncing solutions in general relativity,” *Eur. Phys. J. C* **84** (2024) 56.

[158] L.K. Duchaniya, S.A. Kadam, J.L. Said and B. Mishra, “Dynamical systems analysis in $f(T, \phi)$ gravity,” *Eur. Phys. J. C* **83** (2023) 27.

- [159] A. Samaddar and S.S. Singh, “Qualitative stability analysis of cosmological parameters in $f(T, B)$ gravity,” *Eur. Phys. J. C* **83** (2023) 283.
- [160] L. Duchaniya, S.V. Lohakare and B. Mishra, “Cosmological models in $f(T, \mathcal{T})$ gravity and the dynamical system analysis,” *Phys. Dark Universe* **43** (2024) 101402.
- [161] L. Pati, S.A. Narawade, S.K. Tripathy and B. Mishra, “Evolutionary behaviour of cosmological parameters with dynamical system analysis in $f(Q, T)$ gravity,” *Eur. Phys. J. C* **83** (2023) 445.
- [162] L. Atayde and N. Frusciante, “Can $f(Q)$ gravity challenge Λ CDM?,” *Phys. Rev. D* **104** (2021) 064052.
- [163] E. Di Valentino, A. Melchiorri and J. Silk, “Reconciling Planck with the local value of H_0 in extended parameter space,” *Phys. Lett. B* **761** (2016) 242.
- [164] S. Vagnozzi, “New physics in light of the H_0 tension: An alternative view,” *Phys. Rev. D* **102** (2020) 023518.
- [165] R. Amanullah, C. Lidman, D. Rubin, G. Aldering et al., “Spectra and Hubble Space Telescope Light Curves of Six Type Ia Supernovae at $0.511 < z < 1.12$ and the Union2 Compilation,” *Astron. J.* **716** (2010) 712.
- [166] N. Aghanim, Y. Akrami, F. Arroja, M. Ashdown et al., “Planck 2018 results - I. Overview and the cosmological legacy of Planck,” *Astron. Astrophys.* **641** (2020) A1.
- [167] E. Di Valentino, A. Mukherjee and A.A. Sen, “Dark Energy with Phantom Crossing and the H_0 Tension,” *Entropy* **23** (2021) 404.
- [168] B. Mishra and S.K. Tripathy, “Anisotropic dark energy model with a hybrid scale factor,” *Mod. Phys. Lett. A* **30** (2015) 1550175.
- [169] B. Mishra, S.K. Tripathy and S. Tarai, “Cosmological models with a hybrid scale factor in an extended gravity theory,” *Mod. Phys. Lett. A* **33** (2018) 1850052.
- [170] B. Mishra, P.P. Ray and R. Myrzakulov, “Bulk viscous embedded hybrid dark energy models,” *Eur. Phys. J. C* **79** (2019) 34.
- [171] S.K. Tripathy, B. Mishra, M. Khlopov and S. Ray, “Cosmological models with a hybrid scale factor,” *Int. J. Mod. Phys. D* **30** (2021) 2140005.
- [172] F.K. Anagnostopoulos, V. Gakis, E.N. Saridakis and S. Basilakos, “New models and big bang nucleosynthesis constraints in $f(Q)$ gravity,” *Eur. Phys. J. C* **83** (2023) 58.
- [173] K. Hotokezaka, E. Nakar, O. Gottlieb, S. Nissanke et al., “A Hubble constant measurement from superluminal motion of the jet in GW170817,” *Nat. Astron.* **3** (2019) 940.

- [174] R.H. Abraham and C.D. Shaw, *Dynamics: The Geometry Of Behavior*, Santa Cruz, Calif. Aerial Press (1992).
- [175] A. Katok and B. Hasselblatt, *Introduction to the Modern Theory of Dynamical Systems*, Cambridge University Press (1995).
- [176] S. Bahamonde, C.G. Böhmer, S. Carloni, E.J. Copeland et al., “Dynamical systems applied to cosmology: Dark energy and modified gravity,” *Phys. Rep.* **775** (2018) 1.
- [177] R. D’Agostino and O. Luongo, “Growth of matter perturbations in nonminimal teleparallel dark energy,” *Phys. Rev. D* **98** (2018) 124013.
- [178] B. Aulbach, *Continuous and Discrete Dynamics near Manifolds of Equilibria*, Springer Berlin, Heidelberg (1984).
- [179] A.A. Coley, “Dynamical Systems in Cosmology,” [arXiv:gr-qc/9910074](https://arxiv.org/abs/gr-qc/9910074).
- [180] M. Seikel, S. Yahya, R. Maartens and C. Clarkson, “Using $H(z)$ data as a probe of the concordance model,” *Phys. Rev. D* **86** (2012) 083001.
- [181] Juan Magaña and Víctor H. Cárdenas and Verónica Motta, “Cosmic slowing down of acceleration for several dark energy parametrizations,” *J. Cosmol. Astropart. Phys.* **2014** (2014) 017.
- [182] H. Wei and S.N. Zhang, “Interacting energy components and observational $H(z)$ data,” *Phys. Lett. B* **654** (2007) 139.
- [183] O. Farooq, F.R. Madiyar, S. Crandall and B. Ratra, “Hubble Parameter Measurement Constraints on the Redshift of the Deceleration-Acceleration Transition, Dynamical Dark Energy, and Space Curvature,” *Astrophys. J.* **835** (2017) 26.
- [184] A. Mukherjee and N. Banerjee, “Parametric reconstruction of the cosmological jerk from diverse observational data sets,” *Phys. Rev. D* **93** (2016) 043002.
- [185] G.K. Goswami, A.K. Yadav, B. Mishra and S.K. Tripathy, “Modeling of Accelerating Universe with Bulk Viscous Fluid in Bianchi V Space-Time,” *Fortschritte der Phys.* **69** (2021) 2100007.
- [186] S. Capozziello and R. D’Agostino, “Model-independent reconstruction of $f(Q)$ non-metric gravity,” *Phys. Lett. B* **832** (2022) 137229.
- [187] S. Capozziello and M. Shokri, “Slow-roll inflation in $f(Q)$ non-metric gravity,” *Phys. of the Dark Universe* **37** (2022) 101113.
- [188] A. Hernández-Almada and M. A. García-Aspeitia and J. Magaña and V. Motta, “Stability analysis and constraints on interacting viscous cosmology,” *Phys. Rev. D* **101** (2020) 063516.

[189] J. Román-Garza, T. Verdugo, J. Magaña and V. Motta, “Constraints on barotropic dark energy models by a new phenomenological $q(z)$ parameterization,” *Eur. Phys. J. C* **79** (2019) 890.

[190] O. Akarsu, J.D. Barrow, C.V.R. Board, N.M. Uzun et al., “Screening Λ in a new modified gravity model,” *Eur. Phys. J. C* **79** (2019) 846.

[191] P. Lemos, E. Lee, G. Efstathiou and S. Gratton, “Model independent $H(z)$ reconstruction using the cosmic inverse distance ladder,” *Mon. Not. Roy. Astron. Soc.* **483** (2018) 4803.

[192] N. Jarosik, C.L. Bennett, J. Dunkley, B. Gold et al., “Seven-Year Wilkinson Microwave Anisotropy Probe (WMAP*) Observations: Sky Maps, Systematic Errors, and Basic Results,” *Astrophys. J. Supp. Ser.* **192** (2011) 14.

[193] E. Komatsu, J. Dunkley, M.R. Nolta, C.L. Bennett et al., “Five-Year Wilkinson Microwave Anisotropy Probe* Observations: Cosmological Interpretation,” *Astrophys. J. Supp. Ser.* **180** (2009) 330.

[194] Y. Wang and P. Mukherjee, “Observational constraints on dark energy and cosmic curvature,” *Phys. Rev. D* **76** (2007) 103533.

[195] E.L. Wright, “Constraints on Dark Energy from Supernovae, Gamma-Ray Bursts, Acoustic Oscillations, Nucleosynthesis, Large-Scale Structure, and the Hubble Constant,” *Astrophys. J.* **664** (2007) 633.

[196] C.L. Bennett, D. Larson, J.L. Weiland, N. Jarosik et al., “Nine-Year Wilkinson Microwave Anisotropy Probe (WMAP) Observations: Final Maps and Results,” *Astrophys. J. Supp. Ser.* **208** (2013) 20.

[197] W.J. Percival, B.A. Reid, D.J. Eisenstein, N.A. Bahcall et al., “Baryon acoustic oscillations in the Sloan Digital Sky Survey Data Release 7 galaxy sample,” *Mon. Not. Roy. Astron. Soc.* **401** (2010) 2148.

[198] C. Blake, E.A. Kazin, F. Beutler, T.M. Davis et al., “The WiggleZ Dark Energy Survey: mapping the distance–redshift relation with baryon acoustic oscillations,” *Mon. Not. Roy. Astron. Soc.* **418** (2011) 1707.

[199] F. Beutler, C. Blake, M. Colless, D.H. Jones et al., “The 6dF Galaxy Survey: baryon acoustic oscillations and the local Hubble constant,” *Mon. Not. Roy. Astron. Soc.* **416** (2011) 3017.

[200] R. Gostri, M.V. dos Santos, I. Waga, R. Reis et al., “From cosmic deceleration to acceleration: new constraints from SN Ia and BAO/CMB,” *J. Cosmol. Astropart. Phys.* **2012** (2012) 027.

[201] C. Gruber and O. Luongo, “Cosmographic analysis of the equation of state of the universe through Padé approximations,” *Phys. Rev. D* **89** (2014) 103506.

- [202] Y. Yang and Y. Gong, “The evidence of cosmic acceleration and observational constraints,” *J. Cosmol. Astropart. Phys.* **2020** (2020) 059.
- [203] V. Sahni, A. Shafieloo and A.A. Starobinsky, “Two new diagnostics of dark energy,” *Phys. Rev. D* **78** (2008) 103502.
- [204] X. Ding, M. Biesiada, S. Cao, Z. Li et al., “Is there Evidence for Dark Energy Evolution?,” *Astrophys. J. Lett.* **803** (2015) L22.
- [205] X. Zheng, X. Ding, M. Biesiada, S. Cao et al., “What are the $Om h^2(z_1, z_2)$ and $Om(z_1, z_2)$ Diagnostics Telling us in Light of $H(z)$ Data,” *Astrophys. J.* **825** (2016) 17.
- [206] J.-Z. Qi, S. Cao, M. Biesiada, T.-P. Xu et al., “What do parameterized $Om(z)$ diagnostics tell us in light of recent observations?,” *Res. Astron. Astrophys.* **18** (2018) 066.
- [207] S. Vagnozzi, F. Pacucci and A. Loeb, “Implications for the Hubble tension from the ages of the oldest astrophysical objects,” *J. High Energy Astrophys.* **36** (2022) 27.
- [208] N. Roy, S. Goswami and S. Das, “Quintessence or phantom: Study of scalar field dark energy models through a general parametrization of the Hubble parameter,” *Phys. of the Dark Universe* **36** (2022) 101037.
- [209] S. Capozziello, R. D’Agostino and O. Luongo, “Thermodynamic parametrization of dark energy,” *Phys. of the Dark Universe* **36** (2022) 101045.
- [210] A.A. Mamon and S. Das, “A parametric reconstruction of the deceleration parameter,” *Eur. Phys. J. C* **77** (2017) 495.
- [211] Z.-X. Zhai, M.-J. Zhang, Z.-S. Zhang, X.-M. Liu et al., “Reconstruction and constraining of the jerk parameter from OHD and SNe Ia observations,” *Phys. Lett. B* **727** (2013) 8.
- [212] A. Mukherjee, “Acceleration of the universe: a reconstruction of the effective equation of state,” *Mon. Not. Roy. Astron. Soc.* **460** (2016) 273.
- [213] S. Carneiro, M.A. Dantas, C. Pigozzo and J.S. Alcaniz, “Observational constraints on late-time $\Lambda(t)$ cosmology,” *Phys. Rev. D* **77** (2008) 083504.
- [214] R.-G. Cai and A. Wang, “Cosmology with interaction between phantom dark energy and dark matter and the coincidence problem,” *J. Cosmol. Astropart. Phys.* **2005** (2005) 002.
- [215] D.M. Scolnic, D.O. Jones, A. Rest, Y.C. Pan et al., “The Complete Light-curve Sample of Spectroscopically Confirmed SNe Ia from Pan-STARRS1 and Cosmological Constraints from the Combined Pantheon Sample,” *Astrophys. J.* **859** (2018) 101.
- [216] H. du Mas des Bourboux, J.-M. Le Goff, M. Blomqvist, N.G. Busca et al., “Baryon acoustic oscillations from the complete SDSS-III Ly α -quasar cross-correlation function at $z = 2.4$,” *Astron. Astrophys.* **608** (2017) A130.

[217] A.J. Ross, L. Samushia, C. Howlett, W.J. Percival et al., “The clustering of the SDSS DR7 main Galaxy sample- I. A 4 per cent distance measure at $z = 0.15$,” *Mon. Not. R. Astron. Soc.* **449** (2015) 835.

[218] G.-B. Zhao, Y. Wang, S. Saito, H. Gil-Marín et al., “The clustering of the SDSS-IV extended Baryon Oscillation Spectroscopic Survey DR14 quasar sample: a tomographic measurement of cosmic structure growth and expansion rate based on optimal redshift weights,” *Mon. Not. R. Astron. Soc.* **482** (2018) 3497.

[219] R. Briffa, C. Escamilla-Rivera, J.L. Said and J. Mifsud, “Constraints on $f(T)$ cosmology with Pantheon+,” *Mon. Not. R. Astron. Soc.* **522** (2023) 6024.

[220] D.J. Fixsen, “The temperature of the cosmic microwavw background,” *Astrophys. J.* **707** (2009) 916.

[221] E.N. Saridakis, R. Lazkoz, V. Salzano, P.V. Moniz et al., *Modified Gravity and Cosmology*, Springer Cham (2021).

[222] K. Bamba, C.-Q. Geng, C.-C. Lee and L.-W. Luo, “Equation of state for dark energy in $f(T)$ gravity,” *J. Cosmol. Astropart. Phys.* **2011** (2011) 021.

[223] H. Akaike, “A new look at the statistical model identification,” *IEEE Transactions on Automatic Control* **19** (1974) 716.

[224] G. Schwarz, “Estimating the Dimension of a Model,” *The Annals of Statistics* **6** (1978) 461.

[225] A.K. Singha, A. Sardar and U. Debnath, “ $f(Q)$ Reconstruction: In the light of various modified gravity models,” *Phys. of the Dark Universe* **41** (2023) 101240.

[226] J. Lu, X. Zhao and G. Chee, “Cosmology in symmetric teleparallel gravity and its dynamical system,” *Eur. Phys. J. C* **79** (2019) 530.

[227] J.B. Jiménez, L. Heisenberg, T. Koivisto and S. Pekar, “Cosmology in $f(Q)$ geometry,” *Phys. Rev. D* **101** (2020) 103507.

[228] F. D’Ambrosio, S.D.B. Fell, L. Heisenberg and S. Kuhn, “Black holes in $f(Q)$ gravity,” *Phys. Rev. D* **105** (2022) 024042.

[229] S. Capozziello, V. De Falco and C. Ferrara, “Comparing equivalent gravities: common features and differences,” *Eur. Phys. J. C* **82** (2022) 865.

[230] S. Capozziello, V.D. Falco and C. Ferrara, “The role of the boundary term in $f(Q, B)$ symmetric teleparallel gravity,” *Eur. Phys. J. C* **83** (2023) 915.

[231] E. Jensko, “Spatial curvature in coincident gauge $f(Q)$ cosmology,” *arXiv: 2407.17568* (2024) .

[232] G. Subramaniam, A. De, T.-H. Loo and Y.K. Goh, “How different connections in flat FLRW geometry impact energy conditions in $f(Q)$ theory?,” *Fortschritte der Phys.* **71** (2023) 2300038.

[233] H. Shabani, A. De and T.-H. Loo, “Phase-space analysis of a novel cosmological model in $f(Q)$ theory,” *Eur. Phys. J. C* **83** (2023) 535.

[234] A. Paliathanasis, “Dynamical analysis of $f(Q)$ -cosmology,” *Phys. Dark Universe* **41** (2023) 101255.

[235] N. Dimakis, A. Paliathanasis, M. Roumeliotis and T. Christodoulakis, “FLRW solutions in $f(Q)$ theory: The effect of using different connections,” *Phys. Rev. D* **106** (2022) 043509.

[236] L. Heisenberg, M. Hohmann and S. Kuhn, “Homogeneous and isotropic cosmology in general teleparallel gravity,” *Eur. Phys. J. C* **83** (2023) 315.

[237] H. Shabani, A. De, T.-H. Loo and E.N. Saridakis, “Cosmology of $f(Q)$ gravity in non-flat Universe,” *Eur. Phys. J. C* **84** (2024) 285.

[238] G. Subramaniam, A. De, T.-H. Loo and Y.K. Goh, “Energy condition bounds on $f(Q)$ model parameters in a curved FLRW Universe,” *Phys. Dark Universe* **41** (2023) 101243.

[239] M.-J. Guzmán, L. Järv and L. Pati, “Exploring the stability of $f(Q)$ cosmology near general relativity limit with different connections,” *Phys. Rev. D* **110** (2024) 124013.

[240] V. Sahni and Y. Shtanov, “Braneworld models of dark energy,” *J. Cosmol. Astropart. Phys.* **2003** (2003) 014.

[241] M. Koussour, N. Myrzakulov, S.H. Shekh and M. Bennai, “Quintessence Universe and cosmic acceleration in $f(Q, T)$ gravity,” *Int. J. Mod. Phys. D* **31** (2022) 2250115.

[242] S. Capozziello, R. D’Agostino and O. Luongo, “Extended gravity cosmography,” *Int. J. Mod. Phys. D* **28** (2019) 1930016.

[243] A. de la Cruz-Dombriz and D. Sáez-Gómez, “On the stability of the cosmological solutions in $f(R, G)$ gravity,” *Classical Quantum Gravity* **29** (2012) 245014.

[244] G. Farrugia and J.L. Said, “Stability of the flat FLRW metric in $f(T)$ gravity,” *Phys. Rev. D* **94** (2016) 124054.

[245] J. Simon, L. Verde and R. Jimenez, “Constraints on the redshift dependence of the dark energy potential,” *Phys. Rev. D* **71** (2005) 123001.

[246] N. Borghi, M. Moresco and A. Cimatti, “Toward a Better Understanding of Cosmic Chronometers: A New Measurement of $H(z)$ at $z \sim 0.7$,” *Astrophys. J. Lett.* **928** (2022) L4.

[247] A.L. Ratsimbazafy, S.I. Loubser, S.M. Crawford, C.M. Cress et al., “Age-dating luminous red galaxies observed with the Southern African Large Telescope,” *Mon. Not. Roy. Astron. Soc.* **467** (2017) 3239.

[248] M. Ganeshalingam, W. Li, A.V. Filippenko, C. Anderson et al., “Results of the Lick Observatory Supernova Search Follow-up Photometry Program: BVRI Light Curves of 165 Type Ia Supernovae,” *Astrophys. J.* **190** (2010) 418.

[249] B.E. Stahl, W. Zheng, T. de Jaeger, A.V. Filippenko et al., “Lick Observatory Supernova Search follow-up program: photometry data release of 93 Type Ia supernovae,” *Mon. Not. Roy. Astron. Soc.* **490** (2019) 3882.

[250] P.J. Brown, A.A. Breeveld, S. Holland, P. Kuin et al., “SOUSA: the Swift Optical/Ultraviolet Supernova Archive,” *Astrophys. Space Sci.* **354** (2014) 89.

[251] K. Krisciunas, C. Contreras, C.R. Burns, M.M. Phillips et al., “The Carnegie Supernova Project. I. Third Photometry Data Release of Low-redshift Type Ia Supernovae and Other White Dwarf Explosions,” *Astron. J.* **154** (2017) 211.

[252] S. Jha, R.P. Kirshner, P. Challis, P.M. Garnavich et al., “UBVRI Light Curves of 44 Type Ia Supernovae,” *Astron. J.* **131** (2006) 527.

[253] M. Hicken, P. Challis, S. Jha, R.P. Kirshner et al., “CfA3: 185 Type Ia Supernova Light Curves from the CfA,” *Astrophys. J.* **700** (2009) 331.

[254] M. Hicken, P. Challis, R.P. Kirshner, A. Rest et al., “CfA4: Light Curves for 94 Type Ia Supernovae,” *Astrophys. J.* **200** (2012) 12.

[255] S. Jha, A.G. Riess and R.P. Kirshner, “Improved Distances to Type Ia Supernovae with Multicolor Light-Curve Shapes: MLCS2k2,” *Astrophys. J.* **659** (2007) 122.

[256] P.A. Milne, P.J. Brown, P.W.A. Roming, S.T. Holland et al., “Near-ultraviolet Properties of a Large Sample of Type Ia Supernovae as Observed with the Swift UVOT,” *Astrophys. J.* **721** (2010) 1627.

[257] D.Y. Tsvetkov and L. Elenin, “SN 2008fv: the Third Type Ia Supernova in NGC 3147,” *Peremennye Zvezdy* **30** (2010) 2.

[258] T. Zhang, X. Wang, W. Li, A.V. Filippenko et al., “Optical Observations of the Rapidly Expanding Type Ia Supernova 2007gi,” *Pub. Astron. Soc. Pacific* **122** (2010) 1.

[259] C. Contreras, M. Hamuy, M.M. Phillips, G. Folatelli et al., “The Carnegie Supernova Project: First Photometry Data Release of Low-Redshift Type Ia Supernovae,” *Astron. J.* **139** (2010) 519.

[260] K. Krisciunas, N.B. Suntzeff, J. Espinoza, D. Gonzalez et al., “Optical and Infrared Photometry of SN 2005df*,” *Research Notes of the AAS* **1** (2017) 36.

[261] M.D. Stritzinger, M.M. Phillips, L.N. Boldt, C. Burns et al., “The Carnegie Supernova Project: Second Photometry Data Release of Low-redshift Type Ia Supernovae,” *Astron. J.* **142** (2011) 156.

[262] J. Wee, N. Chakraborty, J. Wang and B.E. Penprase, “Optical and Infrared Photometry of the nearby SN 2017cbv,” *Astrophys. J.* **863** (2018) 90.

[263] M. Kawabata, K. Maeda, M. Yamanaka, T. Nakaoka et al., “SN 2019ein: New Insights into the Similarities and Diversity among High-velocity Type Ia Supernovae,” *Astrophys. J.* **893** (2020) 143.

[264] P. Chen, S. Dong, C.S. Kochanek, K.Z. Stanek et al., “The First Data Release of CNIA0.02—A Complete Nearby (Redshift ≤ 0.02) Sample of Type Ia Supernova Light Curves*,” *Astrophys. J. Supp. Ser.* **259** (2022) 53.

[265] R.J. Foley, D. Scolnic, A. Rest, S.W. Jha et al., “The Foundation Supernova Survey: motivation, design, implementation, and first data release,” *Mon. Not. Roy. Astron. Soc.* **475** (2018) 193.

[266] M. Sako, B. Bassett, A.C. Becker, P.J. Brown et al., “The Data Release of the Sloan Digital Sky Survey-II Supernova Survey,” *Pub. Astron. Soc. Pacific* **130** (2018) 064002.

[267] M. Betoule, R. Kessler, J. Guy, J. Mosher et al., “Improved cosmological constraints from a joint analysis of the SDSS-II and SNLS supernova samples,” *Astron. Astrophys.* **568** (2014) A22.

[268] M. Smith, C.B. D’Andrea, M. Sullivan, A. Möller et al., “First Cosmology Results using Supernovae Ia from the Dark Energy Survey: Survey Overview, Performance, and Supernova Spectroscopy,” *Astron. J.* **160** (2020) 267.

[269] R.L. Gilliland, P.E. Nugent and M.M. Phillips, “High-Redshift Supernovae in the Hubble Deep Field*,” *Astrophys. J.* **521** (1999) 30.

[270] A.G. Riess, P.E. Nugent, R.L. Gilliland, B.P. Schmidt et al., “The Farthest Known Supernova: Support for an Accelerating Universe and a Glimpse of the Epoch of Deceleration*,” *Astrophys. J.* **560** (2001) 49.

[271] N. Suzuki, D. Rubin, C. Lidman, G. Aldering et al., “The Hubble Space Telescope Cluster Supernova Survey. V. Improving the Dark-energy Constraints above $z > 1$ and Building an Early-type-hosted Supernova Sample,” *Astrophys. J.* **746** (2012) 85.

[272] A.G. Riess, S.A. Rodney, D.M. Scolnic, D.L. Shafer et al., “Type Ia Supernova Distances at Redshift > 1.5 from the Hubble Space Telescope Multi-cycle Treasury Programs: The Early Expansion Rate,” *Astrophys. J.* **853** (2018) 126.

Appendices

Cosmological datasets

A) Hubble data with 32 data points :

z -value	$H(z)$	σ_H	Ref.	z -value	$H(z)$	σ_H	Ref.
0.07	69.0	19.6	[119]	0.4783	80.9	9.0	[117]
0.09	69.0	12.0	[245]	0.48	97	62	[122]
0.12	68.6	26.2	[119]	0.593	104	13	[116]
0.17	83	8	[245]	0.68	92	8	[116]
0.179	75.0	4.0	[116]	0.75	98.8	33.6	[246]
0.199	75.0	5.0	[116]	0.781	105	12	[116]
0.200	72.9	29.6	[119]	0.875	125	17	[116]
0.27	77	14	[245]	0.88	90	40	[122]
0.28	88.8	36.6	[119]	0.9	117	23	[245]
0.352	83	14	[116]	1.037	154	20	[116]
0.38	83.0	13.5	[117]	1.3	168	17	[245]
0.4	95	17	[245]	1.363	160	33.6	[121]
0.4004	77	10.2	[117]	1.43	177	18	[245]
0.425	87.1	11.2	[117]	1.53	140	14	[245]
0.445	92.8	12.9	[117]	1.75	202	40	[245]
0.47	89	49.6	[247]	1.965	186.5	50.4	[121]

TABLE 6.1: $H(z)$ measurements expressed in $[\text{km s}^{-1} \text{ Mpc}^{-1}]$ units, were obtained using the CC technique, along with the associated errors.

B) Pantheon⁺ data with 1701 samples :

Source	$N_{\text{SN}} / N_{\text{Tot}}$	z range	Ref.
LOSS1	105/165	0.0020 – 0.0948	[248]
LOSS2	48/78	0.0008 – 0.082	[249]
SOUSA	57/121	0.0008 – 0.0616	[250]
CSP	89/134	0.0038 – 0.0836	[251]
CfA1	13/22	0.0031 – 0.123	[21]
CfA2	24/44	0.0067 – 0.0542	[252]
CfA3S + CfA3K	92/185	0.0032 – 0.084	[253]
CfA4	50/94	0.0067 – 0.0745	[254]
LOWZ	46/95	0.0014 – 0.123	[255–263]
CNIa0.02	15/17	0.0041 – 0.0303	[264]
Foundation	179/242	0.0045 – 0.1106	[265]
SDSS	321/499	0.0130 – 0.5540	[266]
PS1MD	269/370	0.0252 – 0.670	[215]
SNLS	160/239	0.1245 – 1.06	[267]
DES	203/251	0.0176 – 0.850	[137, 268]
HDFN	0/1	1.755	[269, 270]
SCP	6/8	1.014 – 1.415	[271]
CANDELS + CLASH	8/13	1.03 – 2.26	[272]
GOODS + PANS	16/29	0.460 – 1.390	[133, 134]

TABLE 6.2: The Pantheon⁺ compilation includes various samples, detailing the number of SNe Ia utilized in the cosmological sample (N_{SN}) versus the total count from the complete dataset (N_{Tot}) along with the specifics on the redshift range covered.

C) BAO measurement samples :

z_{BAO}	$\frac{r_s(z_d)}{D_V(z_{BAO})}$	$\frac{d_A(z_*)}{D_V(z_{BAO})}$	$\frac{d_A(z_*)}{D_V(z_{BAO})} \cdot \frac{r_s(z_d)}{r_s(z_*)}$	Ref.
0.106	0.336 ± 0.015	30.95 ± 1.46	32.35 ± 1.45	[199]
0.200	0.1905 ± 0.0061	17.55 ± 0.60	18.34 ± 0.59	[197]
0.350	0.1097 ± 0.0036	10.11 ± 0.37	10.56 ± 0.35	[197]
0.440	0.0916 ± 0.0071	8.44 ± 0.67	8.82 ± 0.68	[198]
0.600	0.0726 ± 0.0034	6.69 ± 0.33	6.99 ± 0.33	[198]
0.730	0.0592 ± 0.0032	5.45 ± 0.31	5.70 ± 0.31	[198]

TABLE 6.3: The most recent BAO distance dataset includes measurements at six different redshifts.

List of Publications and Presentations

Thesis Publications

1. **S. A. Narawade**, Shashank P. Singh and B. Mishra, “Accelerating cosmological models in $f(Q)$ gravity and the phase space analysis”, *Phys. of the Dark Universe* **42** (2023) 101282.
2. **S. A. Narawade** and B. Mishra, “Phantom cosmological model with observational constraints in $f(Q)$ gravity”, *Ann. der Phys.* **535** (2023) 2200626.
3. **S. A. Narawade** and B. Mishra, “Insights into $f(Q)$ gravity: modeling through deceleration parameter”, *J. High Energy Astrop.* **45** (2025) 409.
4. **S. A. Narawade**, Santosh V Lohakare and B. Mishra, “Stable $f(Q)$ gravity model through non-trivial connection”, *Annals Phys.* **474** (2025) 169913.
5. **S. A. Narawade**, S. H. Shekh, B. Mishra, Wompherdeiki Khyllep and Jibitesh Dutta, “Modelling the Accelerating Universe with $f(Q)$ Gravity: Observational Consistency”, *Eur. Phys. J. C* **84** (2024) 773.

Other Publications

1. **S. A. Narawade**, Laxmipriya Pati, B. Mishra and S. K. Tripathy, “Dynamical system analysis for accelerating models in non-metricity $f(Q)$ gravity”, *Phys. of the Dark Universe* **36** (2022) 101020.
2. **S. A. Narawade**, M. Koussour and B. Mishra, “Constrained $f(Q, T)$ gravity accelerating cosmological model and its dynamical system analysis”, *Nuc. Phys. B* **992** (2023) 116233.
3. **S. A. Narawade**, M. Koussour and B. Mishra, “Observational Constraints on Hybrid Scale Factor in $f(Q, T)$ Gravity with Anisotropic Space-Time”, *Ann. der Phys.* **535** (2023) 2300161.

4. **S. A. Narawade**, S. K. Tripathy, Raghunath Patra and B. Mishra, “Baryon asymmetry constraints on Extended Symmetric Teleparallel Gravity”, *Gravitation and Cosmology* **30** (2024) 135.
5. Laxmipriya Pati, **S. A. Narawade**, S. K. Tripathy and B. Mishra, “Evolutionary behaviour of cosmological parameters with dynamical system analysis in $f(Q, T)$ gravity”, *Eur. Phys. J. C* **83** (2023) 445.
6. Rahul Bhagat, **S. A. Narawade** and B. Mishra, “Weyl type $f(Q, T)$ gravity observational constrained cosmological model”, *Phys. of the Dark Universe* **41** (2023) 101250.
7. Rahul Bhagat, **S. A. Narawade**, B. Mishra and S. K. Tripathy, “Constrained cosmological model in $f(Q, T)$ gravity with non-linear non-metricity”, *Phys. of the Dark Universe* **42** (2023) 101358.
8. Muhammad Azzam Alwan, Tomohiro Inagaki, B. Mishra and **S. A. Narawade**, “Neutron Star in Covariant $f(Q)$ gravity”, *J. Cosmol. Astrophys.* **2024** (2024) 011.
9. Y. Kalpana Devi, **S. A. Narawade** and B. Mishra, “Constraining Parameters for the Accelerating Universe in $f(R, \mathcal{L}_m)$ Gravity”, *Phys. of the Dark Universe* **46** (2024) 101640.
10. Muhammad Azzam Alwan, Tomohiro Inagaki, **S. A. Narawade** and B. Mishra, “Exploring the universal $\bar{\mathcal{I}} - \mathcal{C}$ relations for relativistic stars in $f(Q)$ gravity”, *arXiv:2501.11296*.

Conferences and Presentations

1. Participated in the 27th International Conference of International Academy of Physical Sciences on Advances in Relativity and Cosmology (PARC-2021) organized by BITS Pilani, Hyderabad Campus, India (October 26 – 28, 2021).
2. Presented a paper entitled “*Phantom cosmological model with observational constraints in $f(Q)$ gravity*” in the *Physical Interpretations of Relativity Theory (PIRT-2023)* organized by Bauman Moscow State Technical University, Moscow, Russia (July 3 - 6, 2023).
3. Presented a paper entitled “*Accelerating cosmological models in $f(Q)$ gravity and the phase space analysis*” in the *The Indian Mathematical Society (IMS-2023)* organized by BITS-Pilani, Hyderabad Campus, India (December 23 - 25, 2023).
4. Presented a paper entitled “*Stable $f(Q)$ gravity model through non-trivial connection*” in *II International Scientific Conference Space. Time. Civilization. (STC – 2024)* organized by BITS Pilani, Hyderabad Campus, India (November 02 – 07, 2024).

Workshop/ International visit (In person)

1. Participated in the workshop on *General Relativity and Cosmology (GRC - 2022)* organized by GLA University, Mathura. (November 24 - 26, 2022).
2. Participated in the *Teacher's Enrichment Workshop* organized by BITS-Pilani Hyderabad Campus (January 09 - 14, 2023).
3. A research visit as a Special Research Student under the BITS-HU joint supervision program to the *Hirosima University* at Hiroshima, Japan (04 January – 29 February, 2024).

Biography

Brief Biography of the Candidate :

Mr. Shubham Atmaram Narawade completed his M.Sc. from National Institute of Technology, Manipur, Manipur, in 2019. He achieved the 31st rank in the joint CSIR-UGC NET all-India exams in June 2019. He also secured 581st all-India rank in the GATE exam in 2019. He published several research papers in reputed national and international journals. He has presented research papers at several national and international conferences. He visited Hiroshima University, Japan as a Special Research Student under BITS-HU joint supervision program during the period January 04, 2024 to February 29, 2024.

Brief Biography of the Supervisor :

Prof. Bivudutta Mishra received his Ph.D. degree from Sambalpur University, Odisha, India, in 2003. His main research areas are Geometrically Modified Theories of Gravity, Theoretical Aspects of Dark Energy and Wormhole Geometry. He has published over 170 research papers in national and international journals, presented papers at conferences in India and abroad, supervised six Ph.D. students and is currently guiding six more. He has also organized academic and scientific events in the department. He has become a member of the scientific advisory committee of national and international academic events. He has successfully completed multiple sponsored projects funded by Government Funding agencies and is at present working on three projects funded by CSIR, SERB-DST (MATRICS) and SERB-DST (CRG-ANRF). He is also an awardee of DAAD-RISE, 2019, 2022. He has also reviewed several research papers in highly reputed journals, is a Ph.D. examiner and is a BoS member of several universities. He has been invited by many foreign universities to share his research in scientific events, some of which are Canada, Germany, the Republic of China, Russia, Australia, Switzerland, Japan, the UK, Poland, etc. As an academic administrator, he was Head of the Department of Mathematics from September 2012 to October 2016 and was Associate Dean of International Programmes and Collaborations from August 2018 to September 2024. He is also a visiting professor at Bauman Moscow State Technical University, Moscow, a visiting associate at Inter-University Centre for Astronomy and Astrophysics, Pune, a Fellow of the Royal Astronomical Society, UK and a Fellow of the Institute of Mathematics and Applications, UK. Foreign member of the Russian Gravitational Society, Moscow. He has been listed among the top 2% of scientists according to the Stanford University author database of standardized citation indicators.